PASSIVE THERMAL MANAGEMENT OF NON-ROAD MOBILE MACHINE BATTERIES

Lappeenranta-Lahti University of Technology LUT

Master's thesis

Master's programme in Electric Transportation Systems

2025

Shruthi Meda

Examiners: Professor Pertti Kauranen

Professor Arunachala Mada Kannan

ABSTRACT

Lappeenranta-Lahti University of Technology LUT

LUT School of Energy Systems

Electrical Engineering

Shruthi Meda

Passive thermal management of non-road mobile machine batteries

Master's thesis

2025

103 pages, 45 figures, 15 tables and 03 appendices

Examiners: Professor Pertti Kauranen and Professor Arunachala Mada Kannan

Keywords: NRMM, PCM, NRTC, BTMS, Temperature, Li-ion Battery, Heat generation

This thesis investigates phase-change-material-based passive thermal management for lithium-ion battery modules in non-road mobile machines. Two 2S2P modules of 14 Ah prismatic cells were assembled: a reference module without PCM and an otherwise identical module with a paraffin-based PCM layer between the cells. After initial capacity, OCV and impedance characterisation, both modules were cycled at 1C and 1.5C using a constant-current / constant-voltage protocol, and the PCM module was additionally tested under a non-road transient cycle (NRTC) combining 2C discharge with 1.5C recharge.

At 1C, the modules showed similar thermal behaviour, with peak temperatures around 33-34 °C and small temperature gradients, indicating limited benefit from PCM at moderate C-rates. At 1.5C, the non-PCM module reached about 37 °C with sensor-to-sensor differences near 5 °C, while the PCM module stayed below roughly 35 °C with gradients of about 3 °C. During 20 NRTC cycles, the PCM module maintained peak temperatures below approximately 34 °C and middle–edge differences of 3-4 °C without temperature accumulation.

Overall, the results show that PCM-based passive thermal management effectively suppresses hot spots and reduces temperature non-uniformity under high-rate and transient operation, while offering little advantage at lower C-rates. Future work should extend NRTC cycling to both PCM and non-PCM modules over longer periods to link the observed thermal improvements to degradation behaviour and lifetime.

ACKNOWLEDGEMENTS

Firstly, I would like to thank my Professors Pertti Kauranen and Arunachala Mada Kannan for giving me this opportunity of pursuing my master's thesis under their expert supervision. Special thanks to Professor Pertti Kauranen for his valuable feedback and advice. His immense support and guidance helped me to carry out this research work smoothly. I also acknowledge Flexible Clean Propulsion Technologies (Flex-CPT) for financially supporting this thesis under the Energy Storage Professorship at LUT University.

My special thanks also go to Vesa Ruuskanen, Matti Piispanen, Henri Löyttynen and Helen Sun for their time and assistance in the laboratory.

I am also thankful to my colleagues in the research group at the LUT School of Energy Systems for their support during my turn as a Junior Research Assistant while pursuing this thesis.

I am grateful for my husband, Sateesh Yeddu, and my daughter, Viyanshi Yeddu, as well as my entire family, for their support and encouragement throughout my master's studies and thesis work. My daughter is a true blessing, showing remarkable strength and patience in my absence, which has continually motivated me to pursue my studies

This thesis would not have been possible without the support of all these wonderful individuals.

SYMBOLS AND ABBREVIATIONS

Roman characters

A	area	m^2
a	proportionality factor	
c	specific heat capacity	$Jkg^{-1} K^{-1}$
C	battery capacity	Ah
e	specific energy	$Wh.kg^{-1}$
	energy density	$Wh. l^{-1}$
f	flat-to-flat length	m
I	current	A
m	mass of the battery	kg
n	number of batteries	
N	number of electrons	
P	power	W
Q	heat	J
R	resistance	Ω
s	side length	m
t	time	s
T	temperature	ºC
U	voltage	V
v	speed	rpm
V	volume	m^3
ΔH	latent heat of fusion	Jkg^{-1}
ΔS	change in entropy	$J.mol^{-1}.K^{-1}$

η	efficiency	
ρ	liquid density	kgm^{-3}
τ	torque	Nm
x	ratio of average to maximum power	

Constants

F	faraday constant	96,484.5 C/mol
π	pi	3.14

Subscripts

bat	battery
eng	engine
hex	hexagonal
i	irreversible
int	internal
j	ohmic
lat	latent
max	maximum
norm	normalised
p	polarization
r	reversible
s	side reaction
sens	sensible
t	total

Abbreviations

ACIR	Alternating Current Internal Resistance
AFIR	Alternate Fuels Infrastructure Regulation
AGV	Automated Guided Vehicles
BTMS	Battery Thermal Management Systems
CC	Constant-Current
CV	Constant-Voltage
DCIR	Direct Current Internal Resistance
DOD	Depth of Discharge
GEIS	Galvanostatic Electrochemical Impedance Spectroscopy
GHG	Greenhouse Gas
HFR	High-frequency Resistance
HP	Heat Pipe
HVAC	Heating, Ventilation and Air Conditioning
IOT	Internet of Things
ITMS	Integrated Thermal Management Systems
LFP	Lithium Iron Phosphate
LGV	Laser Guided Vehicles
LHD	Load Haul Dumps
LIB	Lithium-ion Battery
LTO	Lithium-Titanate Oxide
NMC	Nickel Manganese Cobalt
NRMM	Non-Road Mobile Machines
NRTC	Non-Road Transient Cycle

OCV	Open Circuit Voltage
PCM	Phase Change Materials
RTG	Rubber Tired Gantry
SEI	Solid Electrolyte Interphase
SOC	State of Charge

Table of contents

Appendices

Appendix 1. Datasheet of the LIB from Phylion

Appendix 2. Datasheet of the Rubitherm RT35

Appendix 3. Calculations of thermal sizing

Figures

Tables

1 Introduction

The Electrification of Non-Road mobile machines (NRMMs), such as excavators and loaders, is required to reduce emissions and increase energy efficiency, and comply in developing environmental regulations. However, operating under high cyclic loads and extreme environmental conditions brings new challenges related to battery safety, reliability, and cycle life. In this respect, effective thermal management plays an important role to operate the cells within their optimal temperature range. Yet, traditional active cooling technologies will require additional energy by means of either fans, pumps, or compressors and may introduce complexity in system integration. For heavy-duty equipment that is used periodically, passive thermal management solutions become more advantageous since they can provide effective temperature control without any additional power consumption or complicated system integrations. Therefore, this thesis drives focused exploration of passive technologies as one pathway towards safe, high-performance, and long-lifetime battery systems in electrified NRMM applications.

The focus of the thesis is on using Phase change materials (PCM) for passive thermal management of Li-ion prismatic cell modules in non-road mobile machines. The problem addressed is that during dynamic load cycles, such as the ones simulated by the Non-Road Transient Cycle (NRTC) test, battery temperatures need to remain within safe operating limits without active cooling. Two identical modules, one equipped with PCM and the other without, are experimentally compared for their thermal performance with the objective of assessing the effectiveness of the PCM in reducing temperature rise and/or improving thermal uniformity. This work is limited to laboratory-scale experimental analysis of NRTC based load conditions. The results are evaluated in terms of how effectively PCM regulates battery temperature, and its heat dissipation performance during NRTC operation. It further discusses on the battery degradation over a defined number of NRTC cycles.

The structure of this thesis consists of a review of non-road mobile machines (section 2.1), the types and thermal behaviour of batteries (section 2.2, 2.3 and 2.4), thermal management methods (section 2.5) focusing on cooling with PCMs (section 2.5.3 and 2.5.4), experimental setup (section 3), results (section 4) and discussions (section 5), and conclusions (section 6) with future recommendations form the structure of this thesis.

2 Literature review

Literature review discusses non-road mobile machines and their operating conditions, various battery technologies involved in and their thermal behaviour. It also explains the cooling strategies used in NRMM batteries along with PCM-based passive cooling methods.

2.1 Non-Road Mobile Machines (NRMMs)

Non-Road mobile machines (NRMM) are machines operating with or without wheels and might be those installed on the chassis of vehicles but are not designed for the transportation of passengers or goods along roads [Antila et al., 2025]. They range from small gardening vehicles to large agricultural tractors, trucks and big heavy-duty mining machinery [Lajunen et al., 2018]. They consume high amounts of energy because they are designed for intensive use and mostly operate off the road in harsh environments to execute certain tasks [Antila et al., 2025; Lajunen et al., 2018]. For this kind of operation, these machines may run for longer periods, often more than a normal eight-hour work shift [Lajunen et al., 2018]. In this section, we will discuss various types of NRMMs, their operating characteristics, energy demands, transient load profiles, which are critical for designing efficient battery thermal management systems (BTMS).

2.1.1 Types of NRMMs

Non-Road Mobile Machines (NRMMs) include a wide range of machines designed to perform specific operations in off-road environments [European commission, 2025]. They are classified as below in Table 1.

Table 1: Classification of NRMMs

S.No.	Type of NRMM	Examples
1	Agricultural and Forestry machines	Agricultural tractors, forest machines like harvesters, forwarders etc., manure spreaders, field choppers etc.
2	Construction machines	Bulldozers, excavators, land rollers, loaders, dumpers, mobile cranes, lifters, etc.
3	Gardening machines	Lawnmowers, Tillers etc.
4	Municipal machines	Street cleaning, snow removal machines etc.
5	Mining machines	Underground Load haul dumps (LHD), haul trucks, drilling rigs etc.
6	Material handling machines	Forklifts, mobile cranes, straddle carriers, Automated Guided Vehicles (AGV), Rubber Tired gantry (RTG) etc.

(a)

(b)

(c)

(d)

Figure 1: Some types of NRMMs (a) Model X Series Combines: John Deere (b) Model 973 Truck loaders: Caterpillar (c) GX Crew Electric Utility Vehicle: John Deere (d) TH550B Battery Electric Mining Truck: Sandvik

2.1.2 Operating conditions of NRMMs

The operating conditions for non-road mobile machines depends on their demanding and variable nature of work. They perform intensive tasks in environments ranging from construction sites to agricultural fields, ports, and mines, they have unique irregular loads, long duty cycles, and several harsh external factors strongly influencing machine performance [Antila et al., 2025]. Therefore, it is essential to understand operating characteristics of NRMMs, which will thus help in designing efficient and reliable powertrains and thermal managements systems for NRMMs [Lajunen et al., 2018; Antila et al., 2025].

Load profiles and duty cycles

The load profiles of NRMMs vary widely depending on machine type, operating environment, and the nature of the task performed [Antila et al., 2025]. NRMMs does not follow standardized or predictable driving cycles, hence its pattern of operation is dynamic and task dependent [Lajunen et al., 2018]. Operating cycles with intermittent periods of loading, include frequent transients in load and speed, which put high mechanical, electrical, and thermal stress on subsystems. Unlike on-road vehicles, typically driven under rather steady-state conditions, NRMMs face irregular dynamic load patterns that combine traction and work-cycle demands. The differences in operating modes reflect the diversity of process-specific energy requirements, sectoral applications, and seasonal use [Antila et al., 2025].

One of the distinctive features of operation regarding NRMMs is that transient load cycles are dominant, with both engine torque and speed varying rapidly under changing mechanical loads [Antila et al., 2025; Lajunen et al., 2018]. These transients have a significant influence on fuel consumption, energy efficiency, and thermal behaviour. It has been shown in various studies that during fast transient operations, the measured fuel consumption of diesel-powered NRMMs can be as high as twice that compared to equivalent steady-state conditions [Lindgren, 2005].

NRMMs face high and low load phases alternately depending on their function. While loading and excavation in construction and forestry are examples of rapid torque fluctuations with highly transient duty cycles, soil tillage in agriculture or road transport normally follows more steady engine operations [Lindgren, 2005].

Also, operational characteristics like long operational hours, frequent idling, and repetitive loading cycles contribute to the overall energy demand of these machines [Antila et al., 2025]. In more demanding industries like mining and harbour operations, their usage could extend up to almost continuous operation, reaching up to 24 hours per day, while, agricultural machinery operates seasonally, and thus annual operating hours are low [Lajunen et al., 2018, Antila et al., 2025].

Power and energy demands

The installed power of small loaders and utility vehicles normally starts at around 10kW, with the largest mining dumpers having installed power as high as 3MW [Lajunen et al., 2018]. The power range of NRMMs such as heavy industrial machines run typically between 50 and 500kW [Antila et al., 2025].

Power and energy needs of NRMMs strongly depend on machine size, application, and operational intensity. Machines designed for material handling, excavation, or mining need high peak power output and torque capability to manage heavy loads and sudden transients, while machines designed for agricultural or forestry applications are more often optimized for continuous mid-level power operation [Antila et al., 2025]. Energy demand also depends on auxiliary systems like hydraulic actuators, cooling systems, and on-board electronics, all of which use certain amount of power during operation [Lajunen et al., 2018]. Because NRMMs normally operate at very high-energy intensities, fuel or electrical energy consumption in standard duty cycles is high [Lindgren, 2005].

Environmental and mechanical conditions

Operating environments of NRMMs are usually severe, with continuous exposures to high mechanical load, dust, vibration, and wide ambient temperature variations. Many machines operate in confined or rugged terrains, restricting airflow and cooling, therefore creating thermal management challenges, especially when using electrified systems [Antila et al., 2025]. Long-term operation under those conditions increases risks of component wear and thermal stress and thus makes system robustness a crucial requirement during design [Lajunen et al., 2018].

Energy supply and infrastructure constraints

Historically, NRMM has primarily depended on ICEs, mainly diesel, which offer high power density, robustness, and ease of refuelling in a remote environment. Diesel and biodiesel fuels continue to dominate the energy mix in NRMMs, although this will rapidly change by the continuous tightening of emission regulations and by decarbonization goals through alternative energy carriers [Antila et al., 2025].

Recent electrification and hybridization improvements have shown that battery-electric, fuel-cell, and diesel-electric hybrid powertrains are suitable alternatives for a variety of NRMM applications. Electric powertrains provide many advantages in improving efficiency, reducing emissions and noise when compared to diesel driven systems [Antila et al., 2025]. For example, electric mining truck may contain 600kWh battery pack, which needs quick charging to increase the uptime, but it needs chargers capable of very high-power delivery up to 1MW which is one of the major infrastructure challenges for large-scale applications [NetZero-Events, n.d.]. It also includes lack of charging or refuelling networks, limited grid capacity, and operational downtime for refuelling especially in remote or off-grid sites [Antila et al., 2025].

The charging and refuelling needs of NRMMs should be combined with the next revision of Alternate Fuels Infrastructure Regulation (AFIR), because many worksites are dependent on mobile power units or hydrogen tank trucks rather than fixed grid connections [Transport & Environment, 2024].

Hydrogen and other renewable fuels, such as methanol and ammonia, are considered as efficient alternate energy sources for heavy-duty NRMMs. These fuels can produce electricity directly in the machine through fuel cells or hybrid energy systems, hence reduces the need of direct grid charging. But there are challenges related to hydrogen storage, refuelling infrastructure, and overall cost [Antila et al., 2025].

The choice between diesel, hybrid, and fully electric depends mainly on infrastructure options, machine size and duty cycle. While smaller and lighter NRMMs are increasingly moving towards battery-electric configurations, larger and continuously operated machines often find that their needs are better met by hybrid or fuel-cell-based systems in balancing range, energy density, and refuelling practically [Antila et al., 2025].

The changes in these energy systems mark a significant step towards the general electrification of non-road mobile machines, as industry approaches sustainability and digitalization, and is described in detail in the next section [Antila et al., 2025].

2.1.3 Electrification of NRMMs

The shift towards electrification is extending far beyond highways and streets, reaching non-road machines. In recent studies, it is identified that one of ways to attain sustainability and low emissions in industrial operations is through electrification of NRMMs [Antila et al., 2025]. These machines consume lots of fuel and produce high emissions and noise pollution when operated with diesel engines. Electric and hybrid powertrains provide a cleaner, quieter, and more efficient alternative that supports global decarbonisation and digitization pathways [Lajunen et al., 2018; Celltech, 2023].

Electrification and digitalization are processes that keep pace with each other, where the embedding of various digital technologies: the Internet of Things (IOT)-based monitoring of critical performance parameters and smart energy management, among others, further enhances operational efficiency, safety, and maintenance planning [Celltech, 2023]. The power demand is highly transient in NRMMs compared to the steady load profiles of on-road vehicles, this makes energy storage and powertrain systems more difficult to design [Lajunen et al., 2018].

The transition is further accelerated by regulatory measures being taken globally. For example, California requires that all new off-road vehicles be zero-emission by 2035, while Oslo aims for zero-emission construction sites by 2030 [Celltech, 2023]. Such policies reflect the growing commitment to reduce greenhouse gas (GHG) emissions. Now, the NRMM sector accounts for about 2% of the total GHG emissions in Europe [Antila et al., 2025].

The advantages of electrification include reduced emissions, improved energy efficiency through regenerative braking and optimised power management, and better performance with a host of factors like instant torque, precise speed control, and low maintenance requirements. Alongside this, robust battery systems are to be developed. Batteries should also be able to withstand harsh operating conditions, vibration, and continuous use without

compromising on the need for fast charging and reliability. At the same time, new European (EU) regulations are focusing on lower carbon footprint, and recycled material usage for batteries, which strengthens the focus on sustainable battery life cycle management [Celltech, 2023]. Some of the NRMMs that are already fully electrified are small tractors, forklifts, and loaders which have higher emission rates in warehouses and underground mines [Antila et al., 2025].

2.2 Batteries and their working principle

A battery is an electrochemical energy storage device that converts chemical energy into electrical energy through a process called as redox (reduction and oxidation), thereby providing power to various electrical devices ranging from small- scale smartphones, laptops to large-scale electric vehicles and grid storage. Group of cells connected either in series or parallel to achieve desired current voltage and current form a battery module and multiple battery module form the battery pack which is used to power any electronic drive systems [Kharabati et al., 2024]. There are many types of batteries i.e., Nickel -Cadmium, Nickel-Metal Hydride, lead-acid etc., among which lithium-ion batteries (LIBs) are highly significant because of their high energy and power density, long service life and eco-friendly, and thus, used in many consumer electronics and high-power applications like electric vehicles (EVs) and energy storage systems [Chen et al., 2019].

A lithium-ion cell consists of positive electrode (cathode), a negative electrode (anode), an electrolyte, a separator, current collectors, and an outer shell. The electrolyte is made up of lithium salts dissolved in organic solvents and other additives [Zhi et al., 2022]. It acts as channel for the transportation of lithium ions between the electrodes. A porous separator which allows the movement of lithium ions freely is placed in between the electrodes to avoid direct contact [Zhi et al., 2022; Boparai & Singh, 2020]. Current collectors are aluminum foil (cathode) and copper foil (anode) because of their excellent conductivity and stability [Zhi et al., 2022].

The cathode is any lithium compound usually like $LiCoO_2$, $LiMn_2O_4$, $LiFePO_4$, or multi element materials like Li [NiMnCo]O_2, whereas anode is mostly graphite due to its low cost, abundance and stable electrochemical properties [Zhi et al., 2022; Boparai & Singh, 2020]. Some of the technologies use Lithium-Titanate Oxide (LTO) as anode.

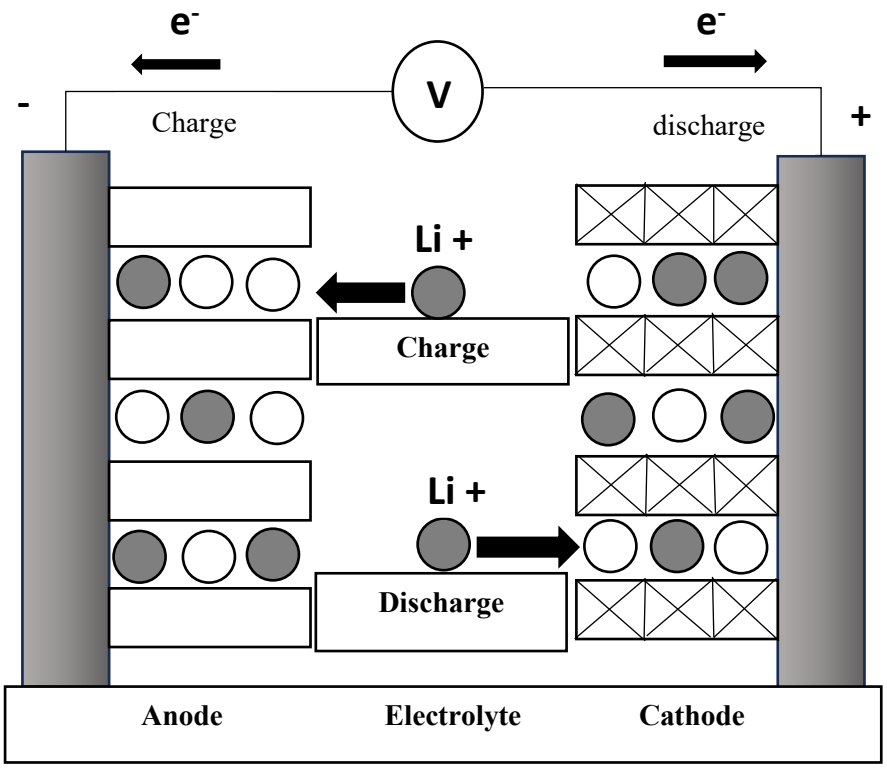

Figure 2: Schematic of Li ion battery, redrawn from [Boparai & Singh ,2020]

Fig 2 explains the working of LIBs. During charging, voltage is applied externally to the current collectors, which causes lithium atoms in the metal oxide structure of the cathode to release electrons and become lithium ions, Li^+ .These Li+ ions reach the anode by moving through the electrolyte, where, along with electrons arriving through the external circuit, they recombine and store in the graphite layers as neutral lithium atoms. The process is reversed during discharge. Lithium atoms in the anode are oxidized to form Li^+ ions and electrons [Kharabati et al., 2024]. The lithium ions move back to the cathode through electrolyte, whereas the electrons flow through the external circuit. This creates an electrical current that can be used to run the devices [Zhi et al., 2022; Kharabati et al., 2024]. The lithium ions combine again with electrons and are re-inserted into the metal oxide structure at the cathode, which completes electrochemical cycle [Kharabati et al., 2024]. In lithium-ion batteries, this is the major process for storing and releasing energy when lithium ions and electrons are transferred reversibly between the electrodes during charge and discharge cycles [Boparai et al., 2020; Kharabati et al., 2024].

2.2.1 Classification of batteries based on their geometry

Lithium-ion batteries are classified into three types based on their geometry, Cylindrical, Prismatic and Pouch cells as shown in Fig 3[Kharabati et al., 2024].

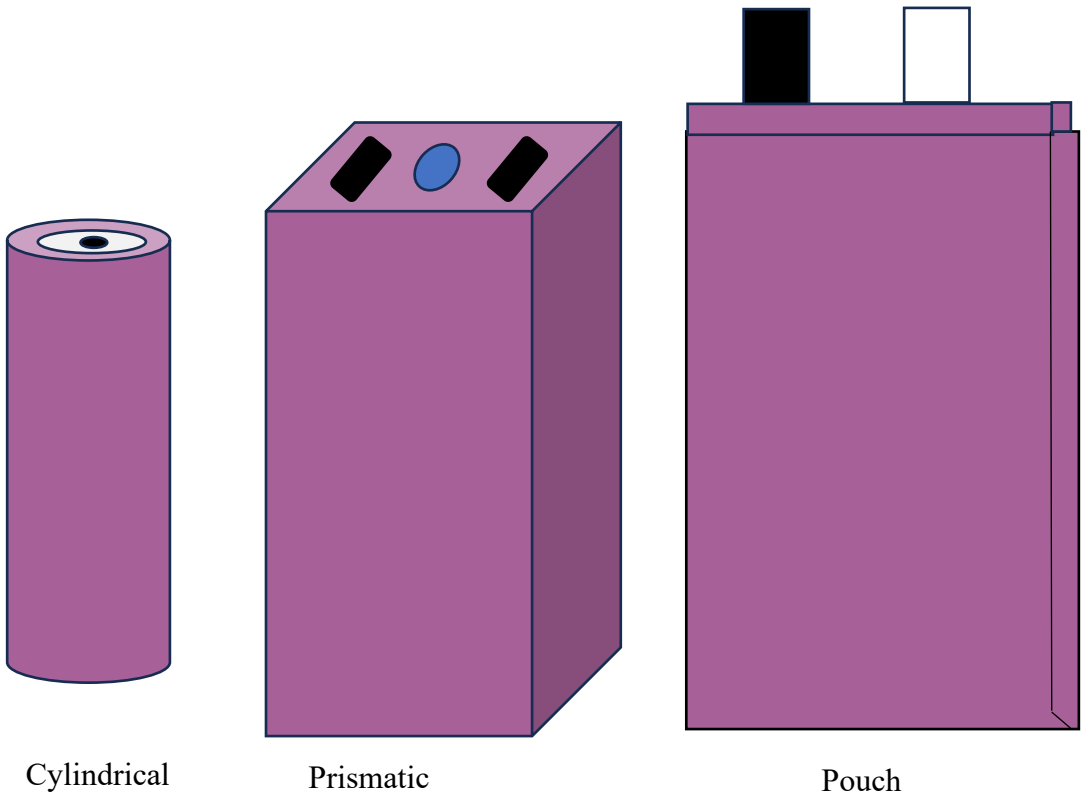

Figure 3: Classification of batteries based on their geometry, redrawn from [Kharabati et al., 2024]

Cylindrical cells can be easily produced with good consistency and lower production cost, but their capacity is limited, whereas prismatic cells provide required capacity, energy and power when connected in series or parallel with their flexible design and space utilization. Pouch cell uses aluminium or polymer laminate as its enclosure instead of metal case like in prismatic cells which reduces cost, weight and thickness but it faces issues like swelling which impacts its lifetime, safety and capacity [Kharabati et al., 2024].

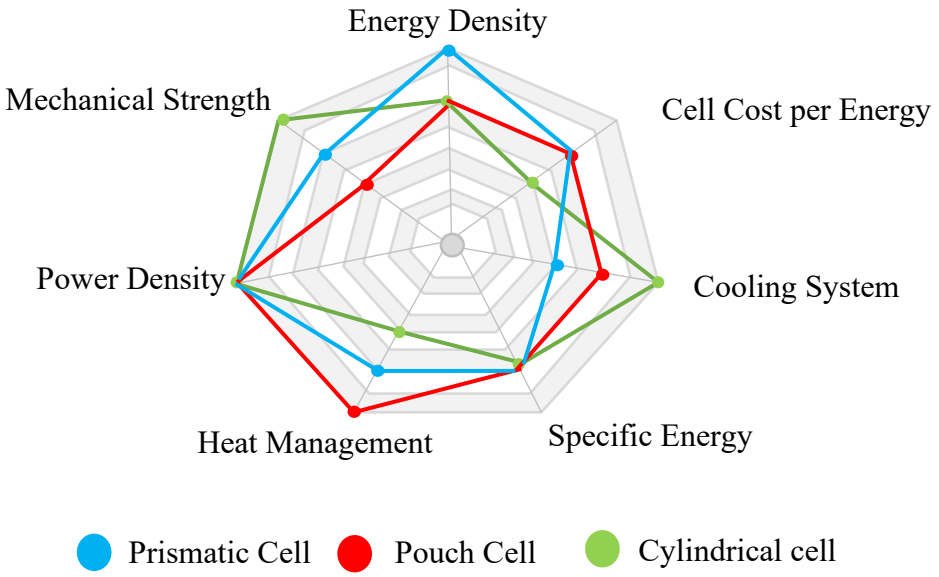

Figure 4: Characteristics of Prismatic, Pouch and Cylindrical cells, redrawn from [Kharabati et al., 2024]

Characteristics of these cells are compared in Fig 4, cylindrical cells provide good cost and structure flexibility but have lower capacity per unit, whereas prismatic cells provide high energy density [Kharabati et al., 2024].

2.3 Battery chemistries in NRMM

Most electrified NRMMs currently use lithium-ion batteries, where cathode is either Nickel Manganese Cobalt (NMC) or Lithium Iron Phosphate (LFP), and anode is graphite or Lithium Titanate Oxide (LTO) [Batteries Europe, 2022].

NMC and LFP have a good balance between energy, power, cost, safety, and lifetime, hence they are used in any kind of applications [Batteries Europe, 2022]. NMC Chemistries provide high energy density and are suitable for applications where space is constrained, while LFP provides superior safety, thermal stability, and longer life cycles, making it ideal for heavy-duty or large NRMMs [Flash battery, 2022; Jaswani, 2024].

Hence, NRMM electrification depends on the choice of battery chemistries that balance safety, cost, and lifecycle performance over high energy density, as many off-road machines have the physical capacity to accommodate larger, heavier battery packs [Jaswani, 2024].

2.3.1 Nickel Manganese Cobalt (NMC)

NMC cells are one of the most common lithium-ion chemistries used in both on-road and non-road vehicle applications. Cathode in NMC is LiNixMnyCozO2, and anode is graphite. There are various types of NMC chemistries (Flash battery, 2022):

a) NMC 111 - Nickel, Manganese and Cobalt are in equal proportions i.e. 33% each.

b) NMC 622 - Nickel accounts for 60%, whereas Manganese and Cobalt accounts for 20% each

c) NMC 811 - Percentage of Nickel is increased to 80%, whereas Manganese and Cobalt are reduced to 10% each)

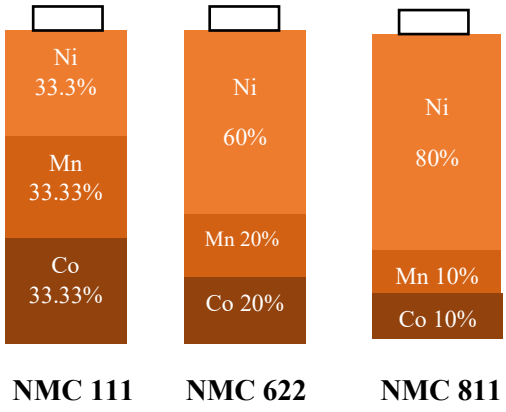

Figure 5: Types of NMC chemistries, redrawn from [Flash battery, 2022]

The three numbers followed by NMC indicates the percentage of materials used for the cathode [Flash battery, 2022]. NMC 811 is the latest technology with increase in Nickel content and lower traces of Manganese and Cobalt resulting in higher energy density at lower cost [Flash battery, 2022]. Typical characteristics of a NMC cell are shown in Table 2 and Fig 6.

NMC batteries can make smaller battery packs with their high energy densities and are suitable for compact machines like 2-tonne excavators [Jaswani, 2024]. However, NMC batteries are more expensive and have higher risk of thermal runaway compared to LFP, hence it is limited only to smaller NRMMs [Batteries Europe, 2022, Jaswani, 2024].

2.3.2 Lithium Iron Phosphate (LFP)

LFP batteries are one of the best suitable batteries for industrial sector, where high safety and long cycle life are important than high specific energy. Major applications of these batteries are NRMM's i.e. in automation, logistics, construction, agriculture etc [Flash battery, 2022]. LFP does not contain cobalt, which makes it safer option as cobalt is toxic to the environment [Batteries Europe, 2022]. Typical characteristics of a LFP cell are shown in Table 2 and Fig 6.

Even though LFP batteries are less dense and heavier in size, their long life, low price, performance maintenance at higher temperatures and greater resistance to thermal runaway makes them best suited to NRMMs [Donaldson, 2024; Jaswani, 2024].

2.3.3 Lithium Titanate Oxide (LTO)

The other cell chemistry commonly used in NRMMs is LTO, which is an alternative anode technology, replacing graphite but keeping either an NMC or LFP cathode [Jaswani, 2024]. LTO does not have high energy density unlike cells with graphite anode, but it is a very stable and robust chemistry [Jaswani, 2024]. It can provide very high cycle life and supports very quick charging as little as three minutes typically with C rates of 10 or higher [Donaldson, 2024; Jaswani, 2024]. Typical characteristics of a LTO cell are shown in Table 2 and Fig 6.

The specific energy of LTO cells is very low but their longevity is very high, lasting more than 20 years in some cases [Donaldson, 2025]. The lower levels of energy density, specific energy (Wh/kg) and voltage rating means that more cells are required in series to obtain the preferred battery voltage [Flash battery, 2022]. LTO technology is ideally used in heavy-duty applications such as AGVs due to their excellent long service life, wide temperature

range [typically -30 to +60 C] and high-power charging but are more expensive [Flash battery, 2022; Donaldson, 2024].

Table 2: Typical characteristics of NMC, LFP and LTO batteries [Flash battery, 2022]

S. No.	Characteristics	NMC	LFP	LTO
1	Voltage Rating, U (V)	3.6	3.2	2.4
2	Specific Energy, e (Wh/kg)	220	177	70
3	Energy Density (Wh/l)	500	384	177
4	Complete life cycles	2000	>4000	15000-20000
5	Discharge rate	2C/3C	1C/3C	4C/8C

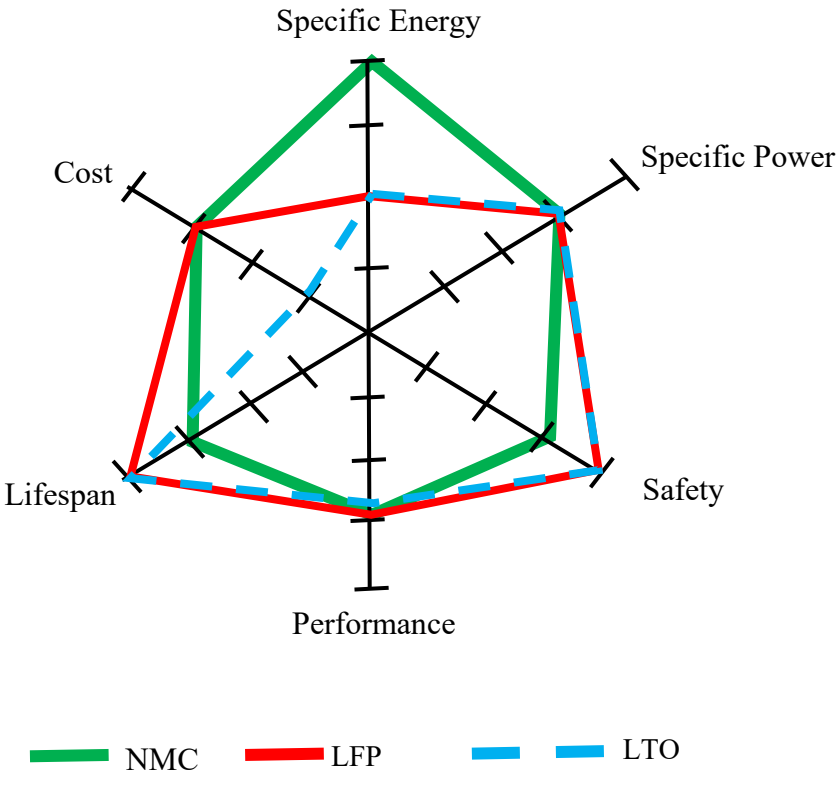

Figure 6: Characteristics of NMC, LFP & LTO batteries, redrawn from [BCG Research, n.d.]

2.3.4 Suitability for non-road machinery

In conclusion, in higher cyclic applications such as NRMMs that puts stress on the batteries, where space is less constraint and it is not mandatory to have high energy density, it is good to use battery types such as LFP and LTO, in which most important requirements are service life, reliability and safety[Flash battery, 2022], while, NMCs are suitable for smaller and compact machines such as excavators where higher energy density is required [Jaswani, 2024]. It is good to have a battery that is a bit larger in size but provides good safety and a significant longer service life. Batteries in vehicles such as Laser Guided Vehicles (LGV) and Automated Guided Vehicles (AGV) which are intensively used and are made to work continuously will have charging cycles for 3 - 4 times in a single day [Flash battery, 2022].

2.4 Battery thermal characteristics

In this section, we will discuss various effects of temperature on batteries, heat generation mechanisms and factors influencing heat in batteries.

2.4.1 Effects of temperature on batteries

Effects of temperature on batteries can be discussed in terms of high temperature, low temperature and the temperature differences as shown in Fig 7.

a) High temperature effects

The performance, safety, and life span of Li-ion batteries are mainly affected by high temperatures. When the battery is operated, internal heat is generated due to its electrochemical reactions, charge transfer, and ohmic losses leading to rise in temperature, and it is important to know about heat generation to minimize high-temperature effects [Ma et al., 2018]. Various heat generation mechanisms are discussed in section 2.4.2.

High temperatures accelerate the ageing of LIBs, reduces capacity and battery life [Ma et al., 2018, Cai et al., 2023]. Cycle aging and calendar aging of LIBs occur together, which affects cathodes, and electrolytes, and the entire battery [Ma et al., 2018, Cai et al., 2023]. $LiCoO_2$ and $LiMn_2O_4$ cathodes went through thermal aging at high temperature such as 75°C

that resulted in lithium intercalation into the cathode which was irreversible and caused severe capacity loss [Ma et al., 2018]. System-level studies also show that LIBs cycled at high temperatures, such as 85°C and 120 °C, suffer extremely high-capacity losses of 7.5% and 22%, respectively, demonstrating the strong dependence of battery performance on operating temperature [Cai et al., 2023].

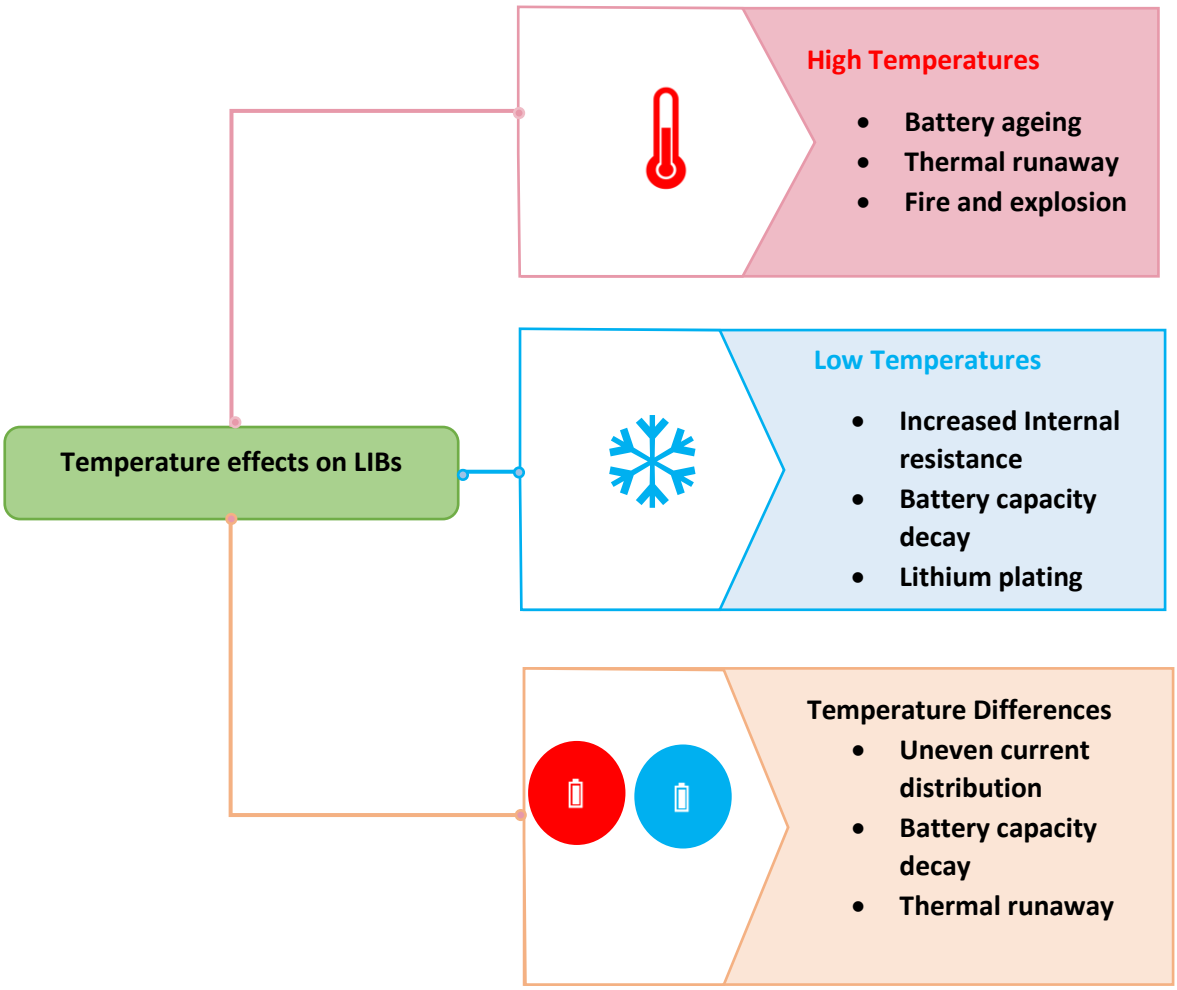

Figure 7: Effects of temperature on LIBs, redrawn from [Cai et al., 2023]

Degradation in Li-ion cells is rooted in the many physical and chemical mechanisms that take hold of the electrodes, electrolyte, separator, and current collectors. Such mechanisms are naturally strongly interacting and acting over a variety of different scales, so that comprehensive modelling is very difficult. Although most models concentrate on dominant processes such as Solid Electrolyte Interphase (SEI) growth or particle cracking, evidence shows that meso and macro-scale structural inhomogeneities in electrodes may generate non-uniform current distribution and lithiation, hence localized ageing that might not be directly

noticeable yet drives overall cell performance. These structural inhomogeneities become much more important under high-temperature conditions, with thermal stress accelerating ageing and enhancing these non-uniform effects [Birkl et al., 2017].

In addition to rapid aging, high temperatures increase the probability of thermal runaway, which is one of the most dangerous modes of failure of Li-ion batteries. Fig 8 explains various causes of thermal runaway. It occurs when the heat generated by a single failed cell is spread to nearest neighbouring cells leading to possible explosion because of the fire's chain-reaction. For example, internal short circuit in Li-ion 18650 cell slowly heat up its internal structure to ~130°C and melts the separator causing sudden energy release. This will rupture the cell, causing flaring and combustion, with temperatures higher than 500°C. Adjacent cells can also be heated up above critical temperatures, leading to further short circuit and transferring the failure. Hence, thermal runaway is noted as extremely high-temperature scenario which points out the importance of measuring and controlling battery temperature for safety reasons [Davis, 2018].

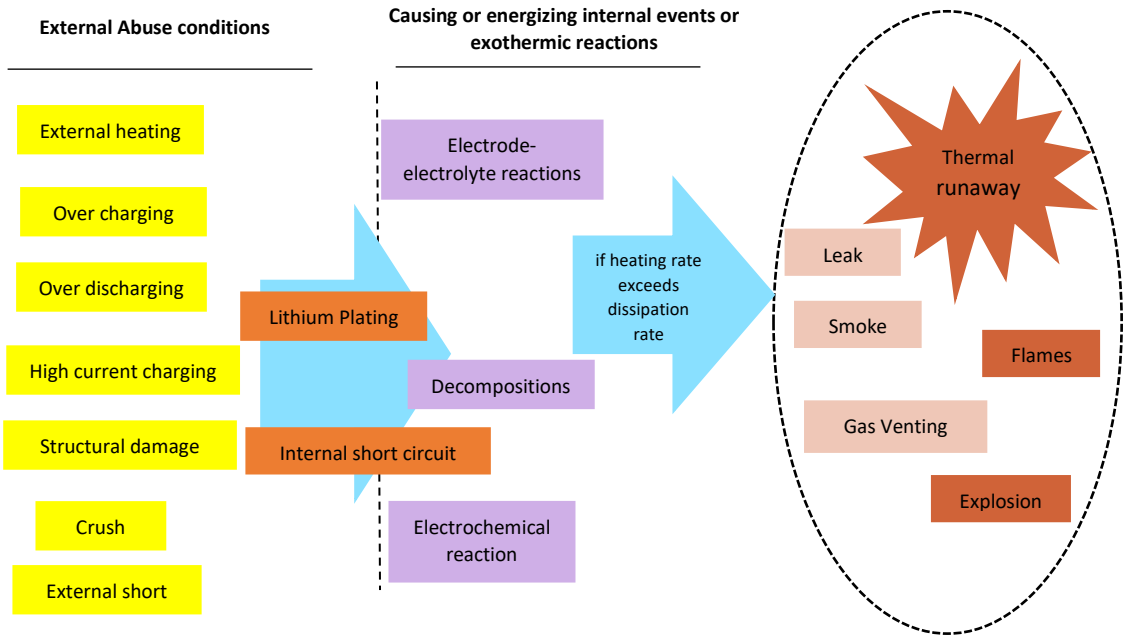

Figure 8: Causes of thermal runaway, redrawn from [Davis, 2018]

When internal temperatures exceed safe threshold limits, exothermic reactions occur in uncontrolled manner by generating gas, increasing internal pressure, and even leading to fire or explosion [Ma et al., 2018, Cai et al., 2023; Mesha 2025]. SEI layer decomposition,

separator melting, and electrode material breakdown all occur serially with rising temperatures and can reach over 1000°C in extreme cases.

b) Low temperature effects

As temperatures below 0°C, LIBs degrade and have various effects [Ma et al., 2018]:

i) It is estimated that capacity of the LIBs decreases by 23% when its operating temperature reduces from 25°C to -15°C [Ma et al., 2018].

ii) Viscosity of the electrolyte will increase at low temperatures, thereby decreasing the ion conductivity and resulting in high internal resistance of the battery [Ma et al., 2018].

iii) At low temperatures, electrochemical reactions controlling charging and discharging run slowly, thereby increasing the charge transfer resistance of the battery [Mesha 2025]. The charge-transfer resistance of LIBs at low temperatures is triple than that in room temperature. It is normally higher in discharged battery than in charged battery. Hence, at low temperatures, it is difficult to charge a battery than discharging it [Ma et al., 2018].

iv) In cold conditions, especially during charging, movement of li-ions slow down and get accumulated on the surface of electrodes forming lithium plating, which is permanent and leads to decrease in capacity and life of the battery, as it disturbs the electrochemical structure of the cell [Ma et al., 2018, Mesha 2025]. These plating further forms dendrite which can penetrate separators and lead to internal short circuit [Ma et al., 2018].

c) Temperature differences

Due to cell manufacturing differences, variations in internal resistance of the battery create different charge states, thereby leading to temperature differences between the individual battery cells and results in thermal instability or thermal runaway [Cai et al., 2023]. Due to the heat generation and low thermal conductivity of Li-ions during higher-rate operation, temperature distribution is non-uniform across the cell thickness. These temperature differences lead to irregular current and resistance distribution, which will speed up the degradation of the battery [Iriyama et al., 2024]. It is essential to maintain uniform temperature throughout the cell and in between the cells inside the battery pack to avoid

localized heating or cold spots [Bao et al., 2025]. Temperature and SOC imbalances between cells can be compensated by charge balancing between the cells, whereas thermal balances are addressed by Battery thermal management systems (BTMS).

2.4.2 Heat generation mechanisms in batteries

Heat in Li-ion batteries are mainly due to of three types of heat: the irreversible heat produced due to internal resistance, the reversible heat produced due to reversible chemical reactions and the side reaction heat. It is given by the Eq. (1) [Guo et al., 2023; Shen et al., 2022; Maher et al., 2024].

$$Q_t = Q_i + Q_r + Q_s \quad (1)$$

Where, Q_t is the total amount of heat produced

Q_i is the amount of irreversible heat produced

Q_r is the amount of reversible heat produced

Q_s is the amount of side reaction heat produced

a) Side reaction heat Q_s: In practice, this heat is produced by some auxiliary reactions that occurs inside the battery and is ignored due to the absence of effects of phase-change [Guo et al., 2023; Maher et al., 2024].

b) Reversible heat Q_r: It is the heat produced during reversible placing and removal of Li^+ ions between the cathode and anode [Guo et al., 2023]. Reversible heat occurs during regular charging and discharging processes and reflects the entropic changes during the electrochemical reactions [Guo et al., 2023; Maher et al., 2024].

$$Q_r = I\,T\left[\frac{\Delta S}{N\,\mathrm{F}}\right] \quad (2)$$

Where, I represent current during charging or discharging in A

T is the operating temperature of the battery in K

ΔS is entropy change

N is the number of electrons interchanged in the chemical reaction in mol

F is the Faraday constant and is equal to 96,484.5 C/mol

c) Irreversible heat Q_i: Different types of irreversible heat generations in batteries are:

i) Ohmic heat Q_j: This heat is generated due to the internal resistance of the battery i.e. mainly in both electrode and electrolyte which prevents transportation of charges [Ma et al., 2018].

$$Q_j = I^2 R_j \tag{3}$$

Where, R_j is ohmic internal resistance of the battery

ii) Polarization heat Q_p: Polarization occurs at the surface of the electrode during charging and discharging of a battery, leads to a deviation between operating voltage and open circuit voltage of the battery [Guo et al., 2023]. This voltage drop increases charge transfer resistance at the electrode-electrolyte interface. When li–ions try to overcome this resistance, the heat is produced which is called as polarization heat [Ma et al., 2018].

$$Q_p = I^2 R_p \tag{4}$$

Where, R_p is ohmic internal resistance of the battery

iii) Heating due to mixing: During charging and discharging when Li–ions are in operation; the distribution of ions becomes uneven leading to mixing of ions and generates heat [Ma et al., 2018]. This heat can be neglected at high and low current rates with small particle sizes, which is the feature of commercial battery designs [Thomas et al.].

iv) Enthalpy change: This heat is generated due to change in phase of cathodes, primarily due to diffusion of Li–ions.

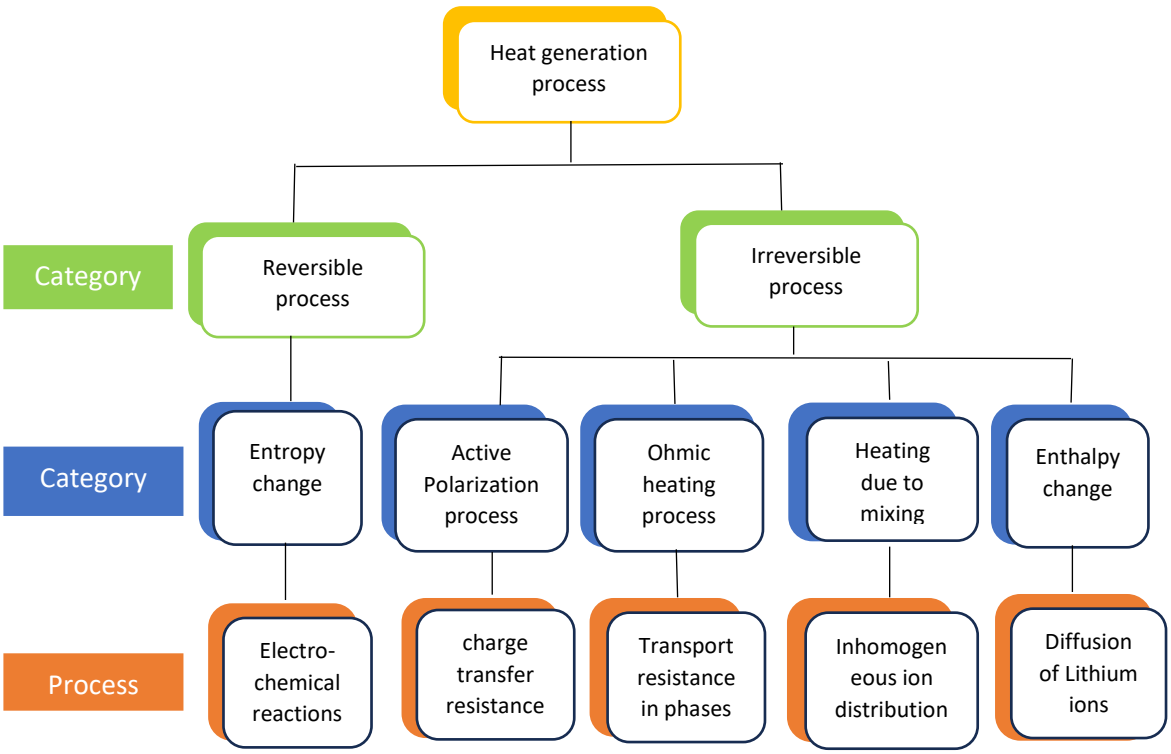

Figure 9: Heat generation process in batteries, redrawn from [Esmaeili & Janne Sari, 2017]

2.4.3 Factors influencing heat generation in batteries

The thermal performance of batteries plays key role in non-road mobile machines, affecting their functionality, safety, efficiency and longevity. Heat production in electrified off-road batteries is influenced by various intrinsic and extrinsic factors which are discussed in this section [Madani et al., 2024].

Intrinsic factors

Internal resistances like ohmic resistances generate joule heat in the form of I^2R losses as discussed in previous section. State of charge (SOC) describes how full the battery is, whereas Depth of discharge (DOD) describes how much capacity has been used, both effects Li-ion concentration gradient, thereby changing internal resistance and leads to heat generation [Madani et al., 2024]. Ageing refers to the overall battery degradation over time, whereas degradation mechanisms are the results effects of ageing, both are intensive in NRMMs due to their complex operating conditions and engine vibrations, which also leads to increase in internal resistance over time and generates joule heat [Madani et al., 2024;

Mocera et al., 2020]. There are two main types of ageing in Li-ion batteries: one is electrochemical damage, in which temperature and electrical load affect the growth of SEI layer and lithium-ion plating, the other is related to vibrations and thermo-mechanical deformation which leads to mechanical damage and material degradation [Madani et al., 2024; Mocera et al., 2020].

Non-road mobile machines undergoing intensive fast charging and discharge cycles at higher C-rates (rate of charge or discharge) or high-power applications produce excess heat [Madani et al., 2024; Lumikko, 2025]. Electrochemical reactions control charging and discharging, hence composition of the materials and design of the electrode may significantly affect heat generation [Madani et al., 2024].

Extrinsic factors

Heavy duty off-road applications involve heavy energy requirements from hydraulic lifting, drilling and material handling that impose heavy instantaneous loads and develop rapid heat build-up; mobile machines operate with unpredictable terrain, variable load and different duty cycles, and in dusty, freezing or humid environments that all challenge thermal management components to bear vibration, mechanical shock and chemical exposure for long service intervals [MEM Magazine, 2025]. Heavy-duty trucks and engineering vehicles with large load capacities place very large demands on their batteries, which are prone to overheating during long-term use, similarly, light trucks, agricultural vehicles, and transport vehicles characterized by frequent use and long working hours are prone to battery overheating and safety issues during continuous operation [Guchen, n.d]. In view of this, advanced thermal management should be designed into the non-road electrification systems early in the design phase to achieve effective, lightweight, compact, and rugged cooling solutions [MEM Magazine, 2025; Lumikko, 2025]. Optimization of cell architecture, module and pack designs and integration of an effective BTMS algorithm is crucial to control operational parameters and avoid excess heat generation rates [Madani et al., 2024].

2.5 Thermal management in NRMM batteries

Efficient Battery Thermal Management System (BTMS) is necessary for electric NRMMs due to its complex operating conditions and harsh environmental conditions such as

exposure to extreme temperatures, dust, vibration, and limited ventilation which increases the risk of overheating. Hence, it is important to control the temperature effectively and maintain optimum functionality of batteries and its surrounding power electronic components [Lumikko, n.d.; Sundar et al., 2023]. The BTMS faces major challenges in NRMMs due to space constraints, that the earlier machines for diesel engines can hardly accommodate additional cooling components, such as heat exchangers, hoses, and pumps [MEM Magazine, 2025]. Integrated thermal management systems (ITMS) consolidate cooling, heating, and degassing into modular units that reduce hoses and actuators by 30%, save weight, ease fitting, and minimize potential failure points [Patil et al., 2023; Zhu et al., 2025]. These should be lightweight, compact, and rugged solutions developed for specific power, size, duty cycles, and harsh environmental conditions of the NRMMs using air, liquid, or phase change materials. The current trends are to use multi-functional hybrid systems in the search for better efficiency and prolonged battery life [Li et al., 2023; Lagerstedt et al., 2025; YANMAR Technical Review, 2023; Guchen, n.d.; Lumikko, 2025].

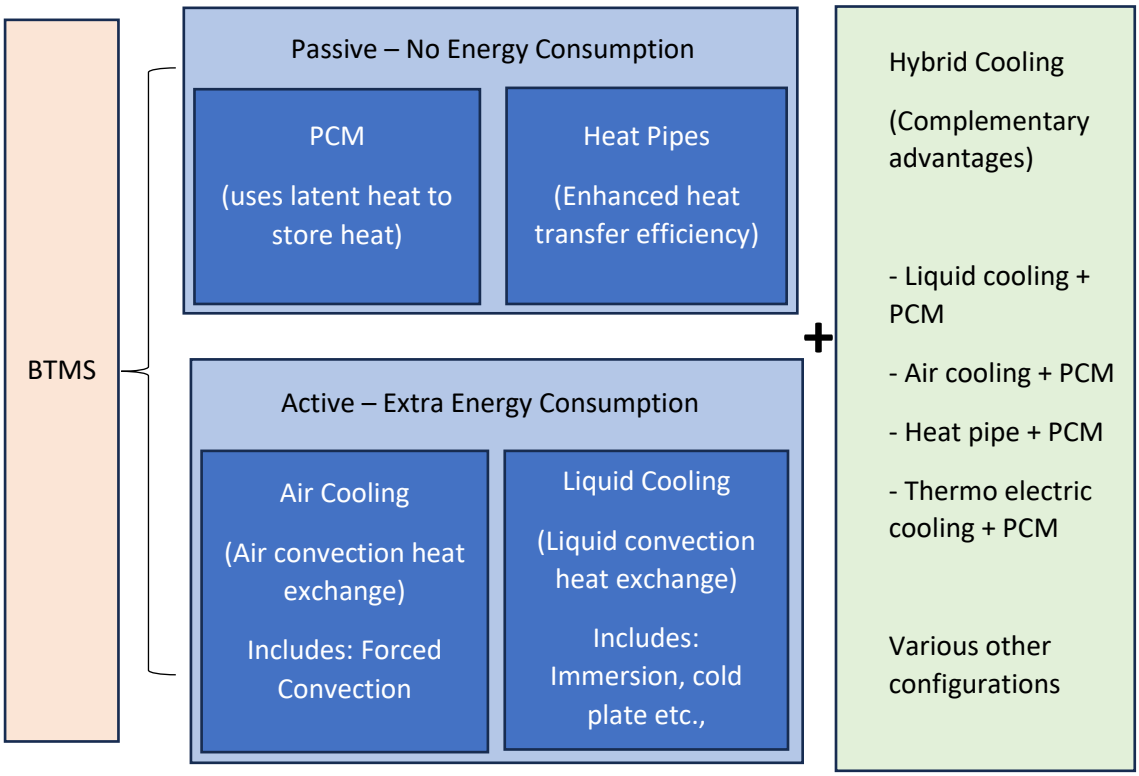

Figure 10: Classification of Battery Thermal Management (BTMS), redrawn from [Bao et al. 2025]

In general, battery cooling strategies are broadly classified into active, passive and hybrid cooling methods as shown in Fig 10 which are discussed in detail in the next sections.

2.5.1 Active cooling

Active cooling is one of the most common cooling methods which is widely used in BTMS of LIBs. It uses fans, pumps, or compressors for cooling, which needs external energy to operate and thereby enhances heat transfer to maintain safety battery temperature. Active cooling is implemented based on ambient conditions i.e., when the ambient temperature is within the normal range (0 to 35 °C), simple ambient air cooling is sufficient. However, at extreme temperatures (below 0 °C or above 35 °C), complex active systems- such as air conditioning-based refrigerant loops or hybrid phase change systems are required to maintain battery thermal performance [Zhang et al., 2024]. Further, active cooling may be divided into categories such as air cooling, liquid cooling and refrigerant cooling, among these, liquid and air cooling find a wide application because of their technological advance and efficiency.

For low-to-moderate thermal loads, air cooling is one of the oldest and widely used active cooling strategies. It works on the principle of convective heat transfer, in which heat generated in the battery modules is taken away by passing the air over the cell surfaces. The effective cooling performance depends on temperature difference between the battery and its surrounding ambient temperature, and the coefficient of convective heat transfer which is a function of airflow velocity, direction and turbulence [Bao et al., 2025]. Active air cooling includes forced convection.

Forced convection uses fans or blowers to force air over the surface of the battery as shown in Fig 11. This supports operation of high thermal loads by increasing the convective heat transfer coefficient and improve temperature distribution. In these systems, the strategic placement of fans and pathways for airflow can give advantages in temperature management and flexibility towards wide operating ranges of electric vehicles [Bao et al., 2025].

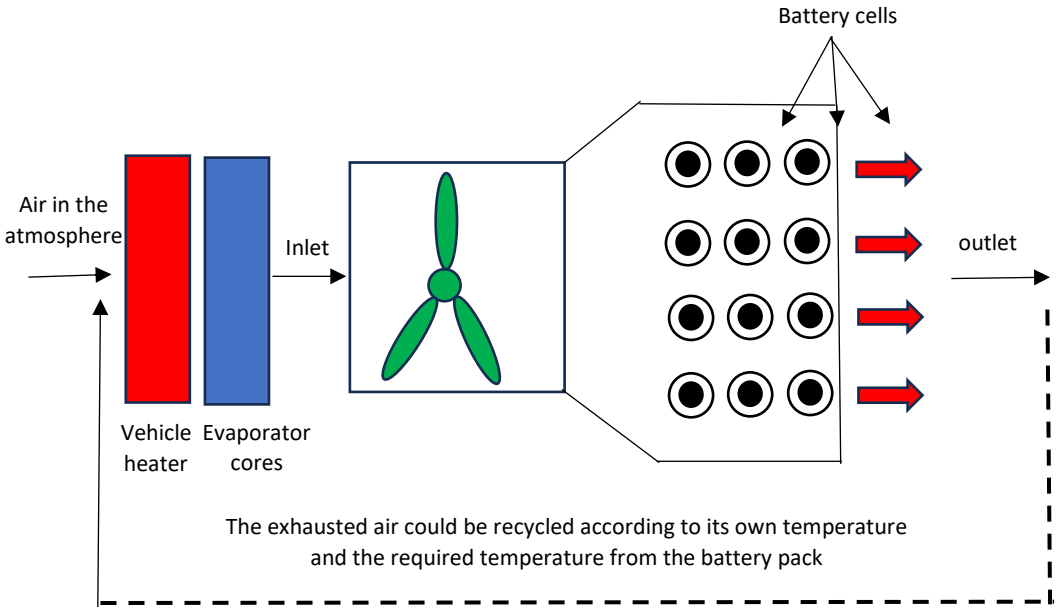

Figure 11: Diagrammatic illustration of active air cooling, redrawn from [Kharabati et al., 2024]

Direct cabin air systems can also be used, in which conditioned cabin air (hot/cool) flows through the battery pack to regulate its temperature, showing an integrated link between vehicle Heating, Ventilation and Air conditioning system (HVAC) and battery cooling system [Zhang et al., 2024]. Air cooling faces few challenges due to its low thermal conductivity and capacity, even though it is simple [Bao et al., 2025]. Solutions to these issues include structure improvements that reduce temperature differences [Zhang et al., 2024].

Liquid cooling has more heat removal capacity than air cooling and is mostly used in modern high-power-density battery systems. Based on contact between the coolant and the cells, liquid cooling falls into two categories: direct (immersion) and indirect (cold plate) systems [Bao et al., 2025].

In direct cooling or immersion cooling, the battery cells are immersed partially or completely into a dielectric liquid. Immersion provides low thermal resistance and hence it has effective uniform heat dissipation. Typically used immersion fluids are mineral oil, synthetic dielectric liquids, and fluorinated coolants. These systems provide excellent thermal regulation, preheating and even suppression of thermal runaway. However, some of the

challenges such as coolant compatibility, sealing reliability, complexity, and maintenance cost limit their use in broader applications [Bao et al., 2025].

Indirect liquid cooling uses cold plates or serpentine channels in which fluids flow without contacting the cells directly. The heat is conducted across solid interfaces, cell-plate-fluid, and extracted by forced convection in the channel. This cooling allows modular design and maintenance, hence it is widely suitable for both electric vehicles and storage systems. Heat transfer is slowed down in this cooling because of presence of multiple thermal resistance layers, hence careful design is required to reduce temperature differences [Bao et al., 2025].

Recent advancements in liquid cooling focus on the optimization of channel and cold plate designs to attain uniformity in cooling and reduce pumping power [Bao et al., 2025].

Liquid cooling needs more energy and complex components making it less suitable than simple, low maintenance passive methods for many space-constrained non-road mobile machines. But advanced integrated cooling represents the state-of-the-art for high power NRMM, providing better heat dissipation under heavy loads even with these drawbacks.

2.5.2 Passive cooling

Passive cooling in BTMS uses environmental conditions, material properties, and geometric changes for heat dissipation without using any external power input. They are more preferred because of their simple and compact design, which makes them cost-effective and long-term reliable. Common methods of passive cooling are natural air convection, incorporating phase change materials and heat pipes that efficiently regulate battery temperature at moderate thermal loads. Recent studies also focused on optimizing battery configurations, such as cylindrical cell arrangement and embedding fins or heat sinks and improve overall heat dissipation performance [Kharabati et al., 2024].

Natural convection works based on a buoyancy effect, hot air comes above the battery surface and is replaced by cooler air. Consequently, it lacks mechanical parts altogether and is thus very energy-efficient and mechanically simple. However, its low airflow and low heat transfer rates make natural convection to work only with low-power systems or those with sufficient natural ventilation [Bao et al., 2025].

The heat pipe (HP) is a vacuum-sealed, enclosed thermodynamic device that uses the phase change of the working fluid between its liquid and vapor states to efficiently transfer heat [Kharabati et al., 2024; Bao et al., 2025]. It is a passive and dual-phase heat transfer mechanism that can transmit massive amounts of heat with minimum temperature variation. A typical HP consists of a condenser, an adiabatic section and an evaporator, which contained in a metallic container that encloses the working fluid and wick structure, which together provide capillary-driven circulation of the liquid between the evaporator and condenser regions [Kharabati et al., 2024]. The properties of the working fluid are directly related to its thermophysical characteristics, which affect its heat transport capacity [Kharabati et al., 2024; Bao et al., 2025].

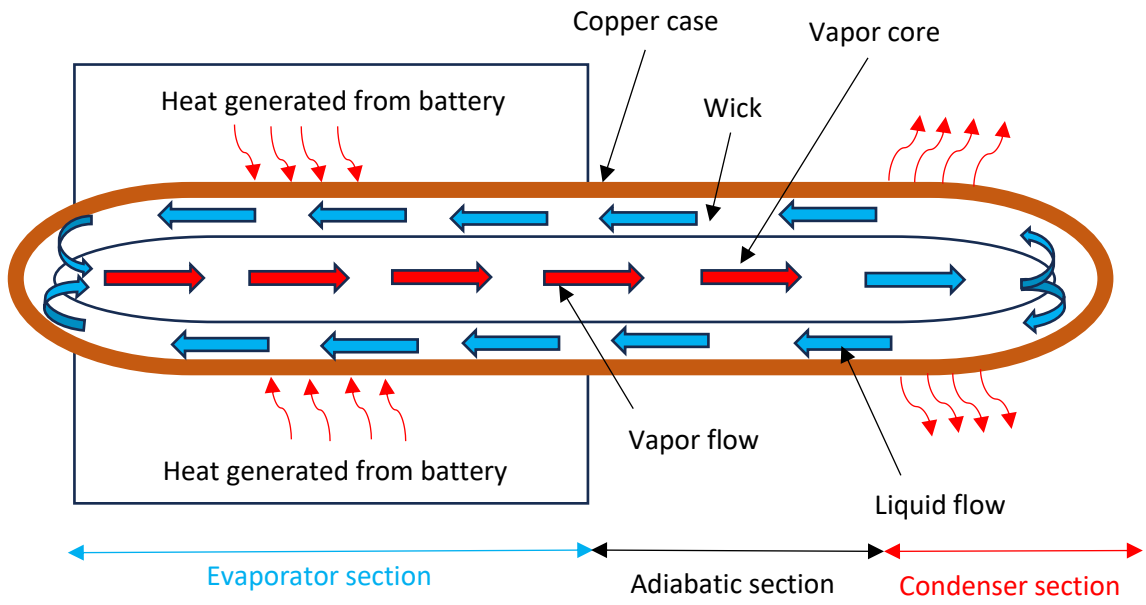

Figure 12: Schematic of heat pipe operation, redrawn from [Kharabati et al., 2024]

As shown in Fig 12, during its operation, the heat input at the evaporator vaporizes the working fluid of the device, increases the local vapor pressure, and drives the vapor toward the condenser [Bao et al., 2025]. As the vapor reaches the condenser, it condenses back into liquid form, by releasing its latent heat and capillary action through the wick, returning to the evaporator [Kharabati et al., 2024; Bao et al., 2025]. This continuous process of evaporation and condensation allows efficient unidirectional heat transfer with no external power input or moving parts and gains high thermal conductivity, commonly several

thousand W/m·K [Bao et al., 2025]. Because of the compact structure, passive operation, and excellent reliability, HPs find widespread applications in electronics cooling, power electronics, automotive systems, aerospace, and, increasingly, in battery thermal management systems, where they effectively remove heat and maintain cell temperature uniformity [Kharabati et al., 2024; Bao et al., 2025]. These advantages also include lightweight design, long service life, resistance to vibration, and low maintenance [Kharabati et al., 2024]. Conventional heat pipes, loop heat pipes, capillary pumped loops, pulsating heat pipes, and vapor chambers are the different configurations of HPs proposed so far for various thermal management applications [Bao et al., 2025].

2.5.3 PCM-based passive cooling

PCM-based passive cooling systems leverage unique thermal properties of PCMs to keep the temperature of a battery within an optimal operating range by storing and releasing latent heat during phase change, normally melting and solidification [Zhi et al., 2022; Kharabati et al., 2024]. In such a system, batteries are usually embedded in a simple-operating, compact, and cost-effective module that offers much better temperature uniformity and reduction of maintenance requirements compared to conventional cooling methods [Zhi et al., 2022]. During melting, PCMs can absorb a large amount of latent heat at almost constant temperature, allowing for effective temperature control during transient/high-rate discharge [Li et al., 2023; Chen et al., 2019]. Material selection with melting points between 20–40 °C can be selected to cover the optimal operational range of lithium-ion batteries [Li et al., 2023]. Passive mode operation does not require any external energy consumption to maintain performance stability and safety during high-power operations [Pilali et al., 2025].

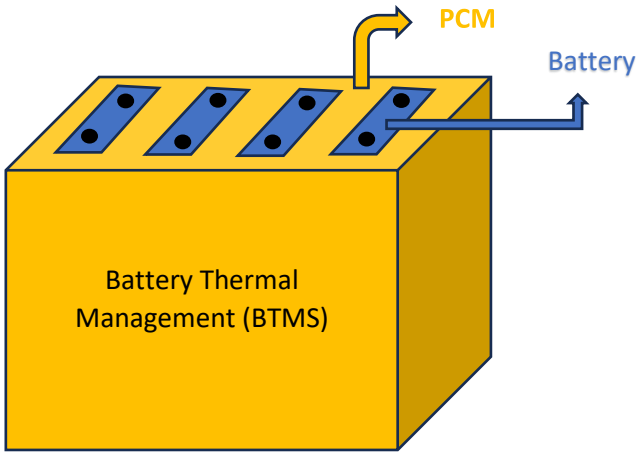

Figure 13: Prismatic battery module with PCM, redrawn from [Rasool et al., 2024]

PCM-based BTMS aligns well with sustainability goals due its low energy consumption and extends battery life by avoiding thermal degradation [Pilali et al., 2025].

Working principle of PCM

As shown in Fig 14, when the battery temperature rises during charging or discharging, the Phase change materials [PCM] absorb this heat and stores as sensible heat [Podara et al., 2021]. Sensible heat is the heat that a material absorbs or releases after and before the phase transition [Kharabati et al., 2024]. At the phase change temperature (melting point of PCM), PCM stores extra heat in the form of latent heat instead of rising its temperature [Podara et al., 2021].

During phase change, the heat absorbed or released is called as latent heat [Kharabati et al., 2024]. The temperature of the PCM remains constant during this phase change even though it absorbs heat. This latent heat storage and the dissipation of heat through natural convection when the PCM has melted, cools the battery efficiently, thereby providing efficient heat control ability and constant ambient temperature to the battery [Zhi et al., 2022; Chen et al., 2019].

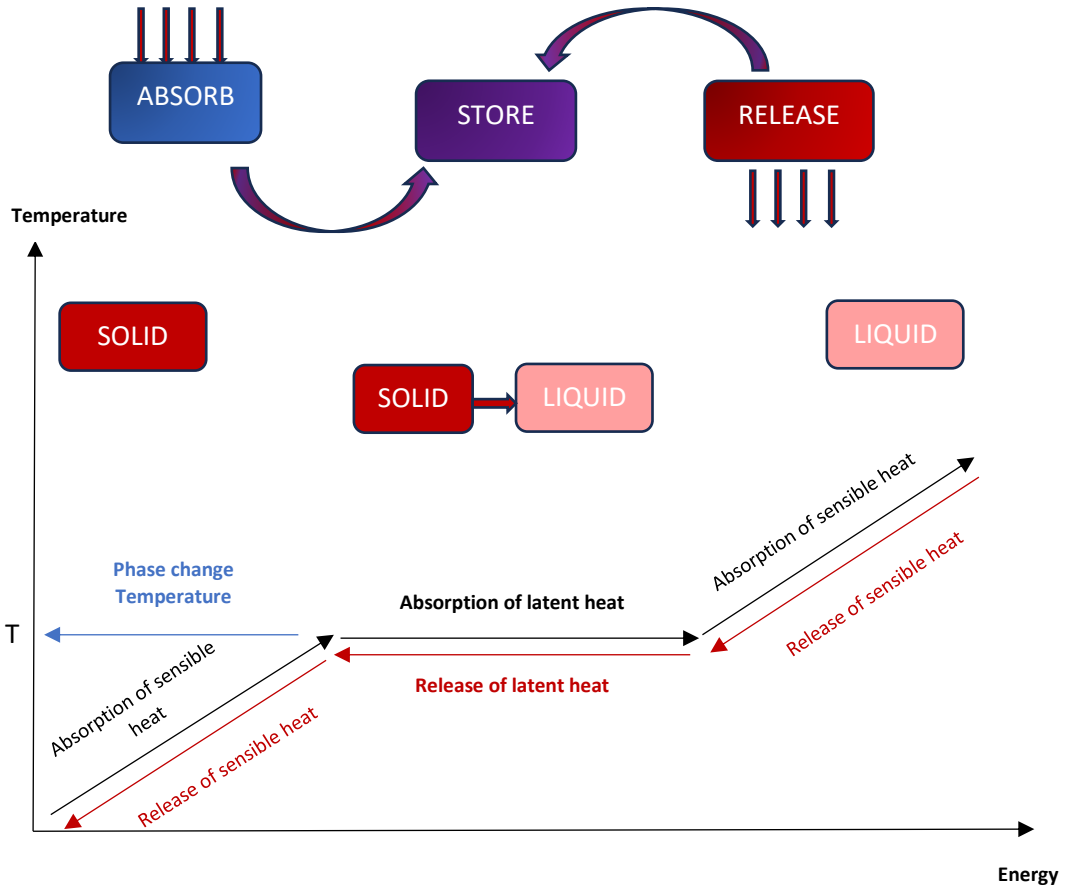

Figure 14: Working principle of PCM, redrawn from [Podara et al., 2021; Kharabati et al., 2024]

Selection criteria for PCM

Identifying and selecting suitable PCM materials for BTMS is essential to maintain efficient heat regulation, safety and durability of batteries. Suitable PCMs should have a high latent heat of phase change and specific heat capacity, which makes them to absorb large amounts of heat and give it out, while having high thermal conductivity and low density [Zhi et al., 2022; Chen et al., 2019; Pilali et al., 2025]. Their melting point or phase change temperature should be within the operating temperature range of lithium-ion batteries for effective heat absorption and release during charge–discharge cycles [Zhi et al., 2022; Pilali et al., 2025]. PCMs should have very low volume change and subcooling, and there should be no phase separation during transitions, thereby maintaining shape stability and chemical reliability. Apart from this, PCMs must be non-toxic, corrosion-resistant and non-flammable, to ensure better safety of the whole battery system. There are some other important practical factors

like low cost, ease of availability, good durability, and ease of packaging that are essential in selection of PCMs [Zhi et al., 2022; Chen et al., 2019].

The thermal conductance of PCMs has a strong impact on the ability of PCMs to transfer heat through them effectively, it is important to improve their conductivity and thereby reduce temperature gradients and allow uniform heat dissipation [Pilali et al., 2025]. The best-suitable PCM for BTMS in lithium-ion batteries combines an appropriate melting point, high latent heat, stable chemical and physical properties, good thermal conductivity, and safety with cost-effectiveness [Zhi et al., 2022; Chen et al., 2019; Pilali et al., 2025].

2.5.4 Classification of PCM

As shown in Fig 15, the classification of PCM is based on three types i.e., temperature, phase change, and material which are further divided into many types as discussed in next sections. The selection of the type of PCM should fulfil the thermal criteria and should be application specific to prevent thermal runway of the batteries [Kharabati et al., 2024].

Phase-transition type PCMs

Based on the phase-transition they undergo, PCMs are of 4 types: solid-solid, solid-liquid, solid-gas, and liquid-gas. In solid-solid transitions, heat is released or absorbed as there are changes in crystal structure of the material. During transition, these materials does not change much in terms of volume, which is an advantage, but the main disadvantage is that it has very low latent heat [Mika et al., 2025]. In practical, it is not favourable to utilize solid-gas and liquid-gas transitions because the produced gas occupies a large volume, and the substantial volume changes of such PCMs require a special design of systems and structures [Zhi et al., 2022; Mika et al., 2025]. In fact, solid-solid and solid-liquid PCMs play a dominant role in many cold and heat storage applications, including BTMS and solar energy utilization [Zhi et al., 2022].

Solid-liquid PCMs are favoured as they store or release relatively high amounts of latent heat, operate effectively across a wide temperature spectrum, typically from 0 to ~150 °C and involve relatively low volume change and lower vapor pressure than liquid-to-gas or solid-to-gas transitions. The production process is relatively simple and inexpensive [Kharabati et al., 2024].

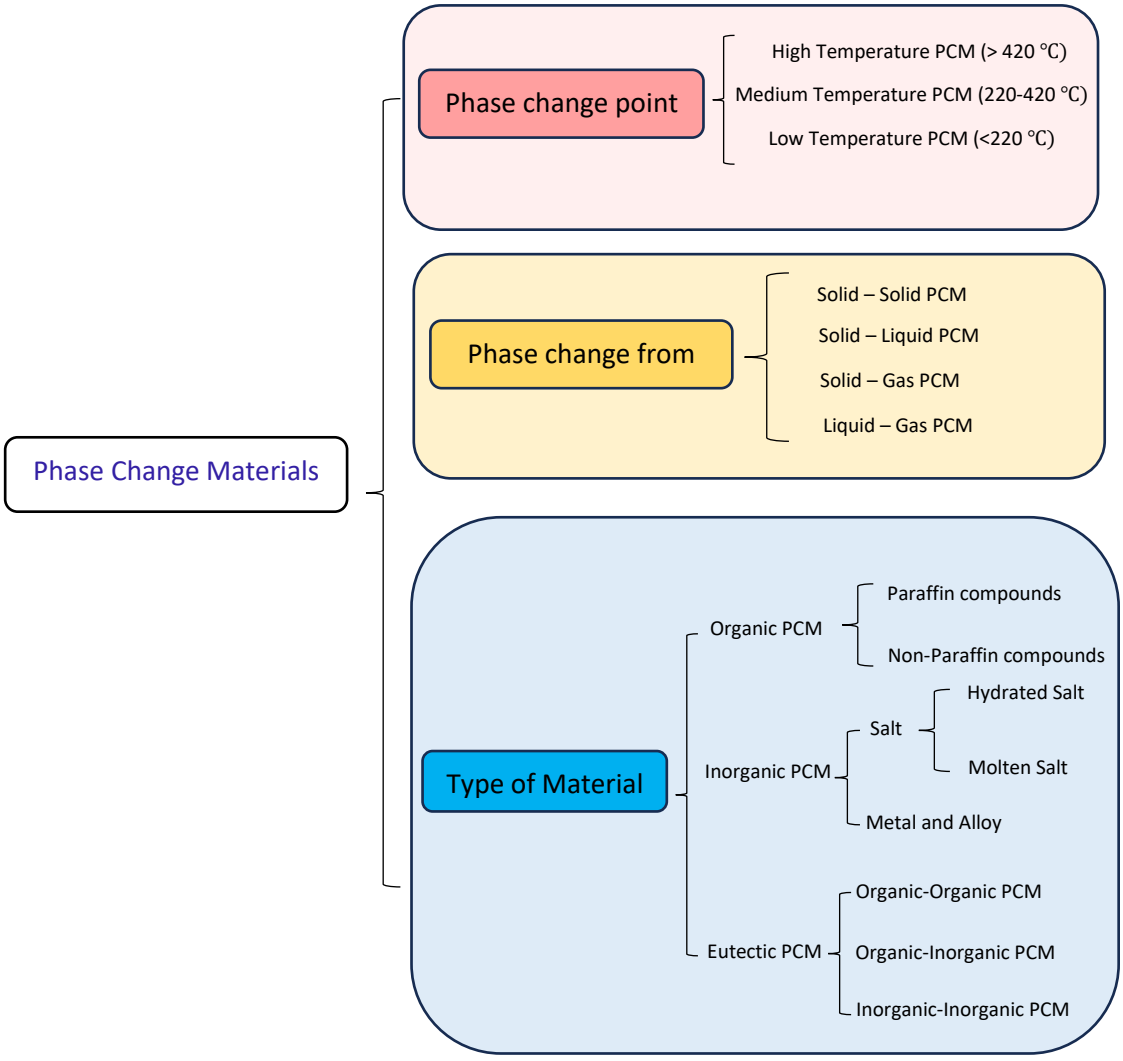

Figure 15: Classification of PCM, redrawn from [Zhi et al., 2022]

Beyond these advantages, solid-liquid PCMs are commercially available, non-hazardous, and do not have any toxic environmental effects. They also have a good chemical compatibility with conventional construction materials [Kharabati et al., 2024].

Among BTMS, solid-liquid PCMs have wider applications because of their controllable volume change and appropriate phase-change properties. Materials like paraffin, a typical solid-liquid phase-change material, are often adopted. In this aspect, the high latent heat, appropriate melting point are the crucial parameters: a high latent heat will contribute much to lower the temperature and temperature difference inside the battery pack [Chen et al., 2019]. Solid-liquid PCM is further classified based on material composition i.e. organic, inorganic and eutectic mixtures which are discussed in the below sections.

Temperature based PCMs

PCMs are classified into high-temperature, medium-temperature and low-temperature based on their phase change temperature. According to Alehosseini et al., 2020 & Zhi et al., 2022 phase change temperatures for these are greater than 420 °C for high-temperature, 220-420 °C for medium-temperature and less than 220 °C for low-temperature. On the other hand, Cai et al., 2023 classifies these PCMs based on their melting points i.e. low temperature PCMs with less than 100 °C, middle temperature PCMs between 100-300 °C, and high temperature PCMs greater than 300 °C. There are many other studies showing different temperature ranges for these PCM classification. But overall, PCMs used in BTMS have melting points between 20-60 °C i.e. low-temperature PCMs which align well with the battery operating temperature 15 °C to 40 °C [Zhi et al., 2022; Li et al., 2023; Guan et al., 2024]. Melting temperatures of few PCMs in the range from 0 °C to 100 °C are shown in Fig 15. It is studied that melting point of Paraffin is 40-50 °C which is well suitable for BTMS and is our main interest in this thesis [Cai et al., 2023].

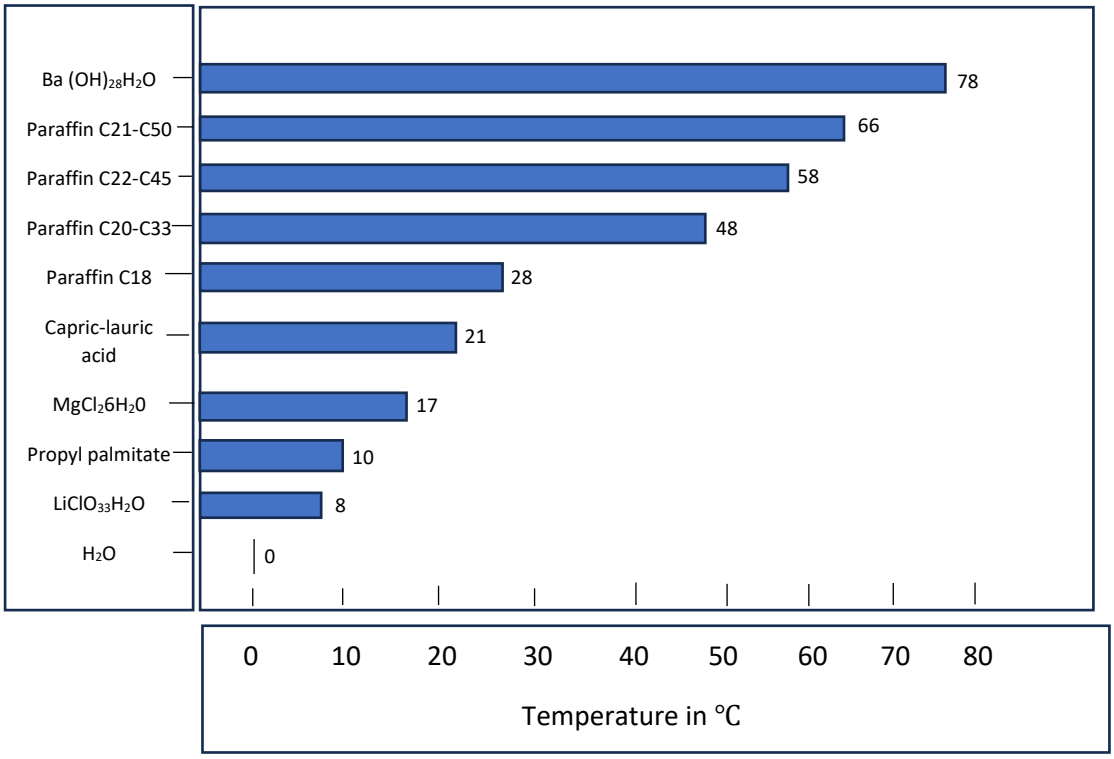

Figure 16: PCMs in the range of 0 °C to 100 °C melting temperatures, redrawn from [Huber et al., 2017]

Material composition based

PCMs are classified into three categories based on the material composition i.e. Organic PCMs, Inorganic PCMs and Eutectic PCMs

Organic PCMs

Organic PCMs are hydrocarbon-based materials and are divided into two types, Paraffin PCMs and non-paraffin PCMs. Paraffin contains straight chain n-alkaline with the chemical formula C_nH_{2n+2} [Kharabati et al., 2024; Guan et al., 2024]. Melting temperature lies in between 20-70 °C and increases with the chain length. They usually contain hydrocarbon chains with whereas pure paraffins have single chain molecules with about 14-40 carbon atoms [Podara et al., 2021].

Non-Paraffin PCMs include fatty acids, esters, alcohols, glycols and other derivatives [Kharabati et al., 2024; Guan et al., 2024; Pilali et al., 2025]. They have wider melting temperature range between 0-200°C depending on their molecular structure. Fatty acids are effective due to their high heat of fusion and suitable phase change temperature [Pilali et al., 2025]. Non-paraffin PCMs are sustainable and biodegradable materials as they can be obtained from bio sources. These PCM are non-toxic and less flammable but are more corrosive and expensive when compared to paraffin based PCMs [Podara et al., 2021].

Paraffin-based PCMs show high latent heat, low subcooling, and minimal volume change with good thermal stability [Podara et al., 2021; Pilali et al., 2025]. These materials are chemically inert, noncorrosive, and compatible with most construction materials, and hence are suitable for applications with repeated phase transitions like energy storage and thermal regulation in batteries [Podara et al., 2021; Pilali et al., 2025]. Paraffin-based PCMs can practically withstand over 1000 melting/freezing cycles without degradation. In addition, several paraffin PCMs melt within the favorable temperature range of 45–60 °C [Pilali et al., 2025]. Paraffins are employed with various carbon-based materials and metal materials forming composite paraffin PCMs to enhance their thermal conductivity and avoid leakage in the process of solid-liquid transition [Zhi et al., 2022].

Despite such advantageous properties, organic PCMs also exhibit various drawbacks: relatively low thermal conductivity, low density, and high flammability may restrict their direct use in some high-heat applications [Podara et al., 2021; Guan et al., 2024]. In contrast,

organic acid PCMs have high latent heat, although lower thermal conductivity can reduce performance [Guan et al., 2024].

Overall, organic PCMs-both from the paraffinic and non-paraffinic family-present very versatile melting point ranges with usually good thermal stability, recyclable states of aggregation, and compatibility for a wide application field in heat storage and temperature control. [Kharabati et al., 2024; Podara et al., 2021; Pilali et al., 2025; Guan et al., 2024].

Table 3: Material modified PCMs and their thermal storage characteristics, adapted from [Zhi et al., 2022]

Type of PCM	**Material**	**Melting Temperature (°C)**	**Latent heat (J/g)**	**Thermal conductivity (W/m. K)**
Carbon materials modified Paraffin based PCMs	Paraffin/EG/Activated carbon	49.79	155.2	5.591
	RT44HC/Fumed Silica (composite 60%/40%)	41.5	133.4	0.18
	RT35HC/Graphene oxide	36.80	240.83	-
Metal modified Paraffin based PCMs	Paraffin/Aluminum (composite 80%/20%)	53.07	118.2	-

Inorganic PCMs

Inorganic PCMs primarily include salt hydrates and metallic PCMs, both of which have been widely studied for thermal energy storage applications [Kharabati et al., 2024; Podara et al., 2021; Guan et al., 2024]. Salt hydrates are ionic compounds with the general chemical formula is $AB{\cdot}nH_2O$ in which the phase change takes place by means of the dehydration or hydration reaction of the salt [Podara et al., 2021; Guan et al., 2024]. They contain high mixture of inorganic salts and water, and thus they have a high energy storage density and thermal conductivity, which makes them a good option for large-scale energy storage with low cost [Guan et al., 2024]. Overall, inorganic PCMs exhibit high enthalpy, low volumetric change, and non-flammability, but most of their supercooling, corrosivity, and phase segregation problems remain as considerable drawbacks that need more material

optimization and encapsulation methods [Podara et al., 2021; Pilali et al., 2025; Guan et al., 2024].

Most inorganic salt hydrates have a phase transition temperature below 120 °C and high latent heat of fusion, hence they are used in low-temperature applications, such as the solar energy and BTMS [Pilali et al., 2025; Guan et al., 2024]. From the point of view of practical applications, the advantageous features of salt hydrates include high thermal conductivity, non-flammability, and low toxicity, ensuring safety and operational stability in energy systems [Pilali et al., 2025]. However, their practical application is clearly limited by factors such as incongruent melting, which can result in the segregation of phases and deterioration of energy storage performance during multiple charge-discharge cycles [Podara et al., 2021]. Poor nucleation properties, leading to supercooling of the liquid phase, along with corrosion, toxicity, and limited compatibility with some construction materials, are other drawbacks of salt hydrates [Podara et al., 2021; Pilali et al., 2025].

Metallic PCMs such as Cu, Al, and Ga show phase change temperatures that are higher than 500 °C, thus ideal for high-temperature applications like production of solar power and waste heat recovery in industries [Guan et al., 2024].

Eutectic PCMs

Eutectic PCMs are materials made up of mixtures containing at least two components, designed such that their melting temperature is lower than any constituent's [Kharabati et al., 2024]. They can be organic, inorganic, or a combination of both types of PCMs which make way for wide range of eutectic mixtures with desired thermal characteristics [Podara et al., 2021; Guan et al., 2024]. The eutectic composition provides the opportunity to tune the key thermal properties, like latent heat and phase change temperature, allowing tailoring for specific applications [Podara et al., 2021].

Eutectic PCMs can be binary or multicomponent systems and can be viewed as combinations such as organic-organic, inorganic-inorganic, or organic-inorganic blends. This will prevent or minimize the disadvantages of individual PCMs and improve their applicability in real energy storage and temperature control applications [Guan et al., 2024]. Of these, organic eutectic mixtures exhibit several specific advantages with respect to inorganic or hybrid eutectic systems, such as long-term stability, high phase change enthalpy, ease of

impregnation into porous material matrixes due to better chemical compatibility and surface tension properties [Podara et al., 2021].

The main disadvantages of eutectic PCMs, especially in organic-based, are the high cost that prevents their use in practical applications [Podara et al., 2021]. However, their easily tunable melting temperatures, effective energy storage capabilities, and compositional flexibility make eutectic PCMs a more popular class of materials for specific thermal management applications [Kharabati et al., 2024; Podara et al., 2021; Guan et al., 2024].

Table 4: Examples of few PCMs and their thermal storage characteristics

Type of PCM	**Material**	**Melting Temperature (°C)**	**Latent heat (J/g)**	**Thermal conductivity (W/m. K)**	**Author**
Organic (Paraffin based)	Paraffin/EG (Composite-(80%-30%)/ (20-70%)	42.03-43.05	166.2–47.76	2.77–19.26	[Zhi et al., 2022]
Organic (non-paraffin based)	Stearic acid/Silicon carbides powder (7.18%/92.82% composite)	53.40	12.87	0.719	[Zhi et al., 2022]
Inorganic	MgSO4•7H2O/Urea resin	48.36	25.46	0.3315	[Zhi et al., 2022]
Eutectic mixture	Capric Acid-Palmitic Acid	26.2	177	-	[Podara et al., 2021]

2.5.5 Hybrid cooling

Hybrid BTMS combines passive techniques like PCMs or heat pipes with active methods such as forced air or liquid circulation. Hybrid systems take advantage of the strengths while minimizing drawbacks [Zhi et al., 2022; Bao et al., 2025; Chen et al., 2019]. These systems address thermal challenges in high energy density LIBs through passive components serving as thermal buffers during peak loads, fast charging, or transient conditions by absorbing latent heat to handle spikes in temperature, while active elements provide a rapid response and prevent saturation of the PCM by removing the accumulated heat [Bao et al., 2025; Chen

et al., 2019]. Hybrid configurations include different approaches such as using PCM with air/liquid cooling or heat pipes for enhanced conductivity and provide outstanding safety, a long lifetime of batteries, energy efficiency, reduced duty cycles of the active components, and fail-safe operation; these hybrids become an ideal solution for electric vehicles under dynamic applications [Bao et al., 2025; Kharabati et al., 2024].

3 Methodology

In this section, we will discuss methodologies adopted for this experimental research. It gives an overview about the battery specification and their configuration, instruments used, types of tests conducted and their test plans, and the experimental setup.

3.1 Battery specification and configuration

3.1.1 Battery specification

In this experimental research, Prismatic Li-ion cells from the manufacturer Phylion are used as shown in Fig 17. The specifications of the battery are as given in below Table 5.

Figure 17: Phylion 14 Ah Prismatic Li-ion cell

Table 5: Specifications of the battery cell used in the experiment

Parameters	**Values**
Manufacturer name	Phylion
Manufacturer part number	ISP18/66/133(14) HA
Model	Prismatic
Rated capacity	14 Ah (1C / +25°C)
Rated voltage	3.65 V
Chemical Composition	Li-ion
Housing	Aluminum
Energy	51.8 Wh
Operating voltage range	2.75 V ~ 4.2 V
Maximum charging voltage	4.20 V
Standard charging current	14 A / 1C
Maximum continuous discharge current	42 A / 3C
Maximum discharge current	70 A / 5C (30 seconds)
Self-discharge rate	≤ 3% / month
Internal resistance	≤ 3 mΩ
Number of cycles	1000
Operating temperature (charging)	0 °C ~ 45 °C
Operating temperature (discharging)	-30 °C ~ 50 °C
Storage temperature	-20 °C ~ 45 °C
Dimensions	66 x 133 x 18 mm
Weight	0.32 kg

By specification, the Phylion ISP18/66/133(14) HA is a high-performance prismatic Li-ion cell that can support high discharge currents, up to 3C continuous and 5C for short periods, at low internal resistance and housed in robust aluminium case. It is therefore suitable for dynamic cycling experiments. Compared to other formats, the prismatic design allows better heat spreading and better structural stability for operation at high power.

3.1.2 Battery configuration

In this experiment, we use two types of battery configurations:

i) Individual prismatic cells for the preliminary tests

ii) A 2S2P (two-series, two-parallel) configuration for the NRTC experiment

This dual-level approach enables detailed baseline measurements on single cells, whereas the pack configuration better represents a realistic application under transient load conditions. For the transient load cycles, two of these individual cells are connected in series, and this series-pair is then paralleled with another identical series-pair, which forms a 2S2P configuration as shown in Fig 18. This doubles both the pack voltage relative to a single cell and the pack capacity, and this helps in more realistic simulation of an application-level battery pack in non-road machinery while staying within the safe operating limits of the test setup.

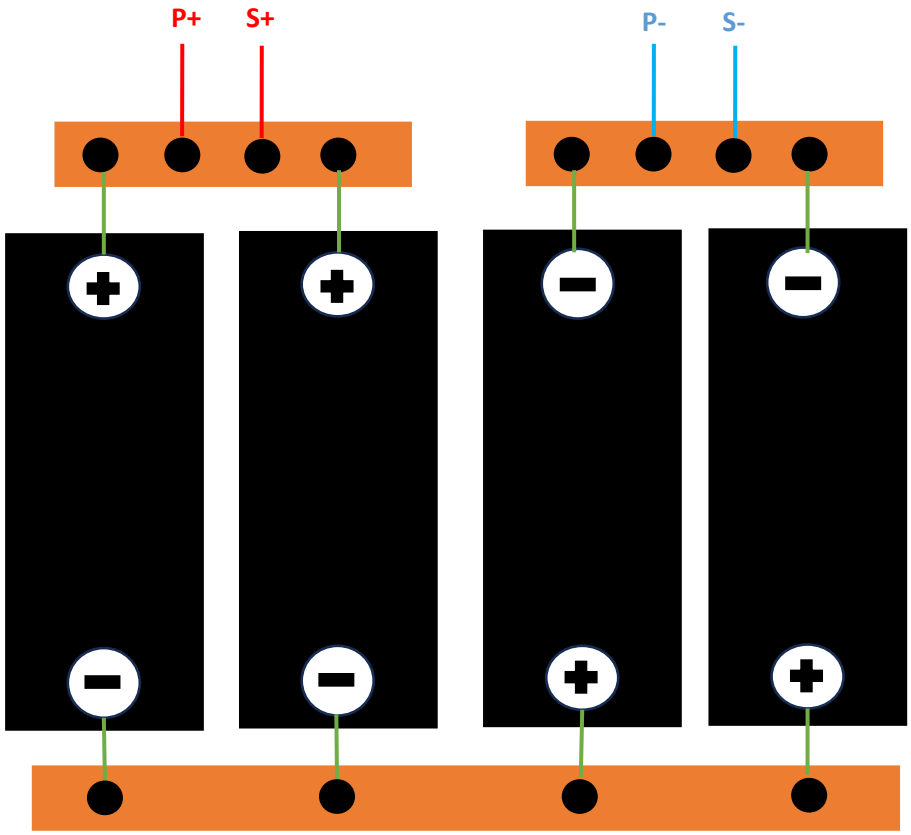

Figure 18: Schematic representation of 2S2P configuration

We choose 2S2P configuration for our experiment due to following advantages:

a) Voltage scaling: By connecting cells in series, the nominal pack voltage becomes ~7.4 V (2 × 3.7 V). Even though NRMM operate at higher voltages (ex: 48VDC or 400VDC), this low voltage is set due to the limitations of available number of cells and battery cycler used in this experiment.

b) Capacity and current capability: 2S2P configuration doubles the usable capacity and spreads the load between cells, reducing stress per cell under high-current discharge. Each cell allows continuous discharge of up to 3C, or 42 A, so the 2S2P pack configuration should safely deliver up to 84 A continuous, which also corresponds to 3C at the pack level. Therefore, running the pack at 2C is well within the rated limits and will ensure reliable behaviour over dynamic NRTC load cycles while still giving a good margin for safety.

c) Thermal balance: The 2S2P configuration helps to study PCM-mediated heat spreading between cells and temperature uniformity in small battery module.

3.2 Instrumentation

3.2.1 Biologic BCS-915 and BT-Test software

The Biologic BCS 915 (Figure 19) is a high power, modular battery cycler providing 8 independent channels, each capable of ±15 A, with the option to parallel channels (e.g., channels 1-2, 3-4 etc or 1-4 or 5-8) to reach much higher currents, i.e., up to ±120 A. It supports five current ranges, delivers very high precision (18-bit resolution for current and voltage), fast data sampling, and has a built-in native Electrochemical Impedance Spectroscopy (EIS) capability from 10 MHz to 10 kHz. Its specifications are as given in Table 6.

Table 6: Biologic BCS-915 specifications

Parameters	Values
Number of channels	8
Cell Connection	4 terminal leads
Power	1700W (VA), 100-240VAC, 50-60Hz
Max current per channel	±15 A continuous
Max power per channel	105 W
Voltage measurement range	0-9 V
Current measurement range	±10 A, ±1 A, ±100 mA, ±10 mA, ±1 mA
Input impedance	100 mΩ, 6pF typical
Input Bias current	< 1 nA
Bandwidth (-3 dB)	4 kHz
Auxiliary inputs / Outputs	1 analog input, 2 digital inputs, 1 digital output, 1 analog output, 8 thermocouple inputs.

Figure 19: Side and front view of BCS-915 cycler

The BT Test module, part of Biologic's BT Lab® Suite, is used to design, run, and monitor complex test plans. It supports up to 128 steps per test, and you can use control modes including constant-current (CC), constant-voltage (CV), power control, Direct Current Internal Resistance (DCIR), Galvano Alternating Current Internal resistance (ACIR), Galvanostatic Electrochemical Impedance Spectroscopy (GEIS), loops, and rest periods. Tests can be monitored in real-time, parameters can be adjusted "on-the-fly," and safety limits can be configured individually for each channel to ensure protection

The BT Test software allows us to program and run test plans easily: including CC CV, GEIS, Open circuit voltage (OCV), and NRTC, for both modules, with real time data monitoring and per channel safety control.

3.2.2 Hioki LR8450-01 Memory HI Logger

The Hioki LR8450-01 Memory HI Logger (Fig 20) which is a variant of standard model Hioki LR8450 is a high-speed, multi-channel data logger capable of precise measurement of physical signals such as temperature, voltage, and resistance. It supports both plug-in and wireless measurement modules, allowing a high channel count and flexible configuration. The instrument features 8 configurable alarm outputs on the external control terminals, which can be triggered based on user-set conditions (e.g., a temperature threshold). Detailed specifications are in included in Table 7.

Figure 20: Hioki LR8450-01 Memory HI Logger

Table 7: Specifications of Hioki Temperature LR8450-01 Memory Hi logger

Parameters	**Values**
Max. sampling interval	1ms
Maximum connectable units	4 plug-in + 7 wireless
Max. measurement channels	Up to 330 channels (with plug-in + wireless)
Pulse / Logic input	8 channels, common GND, non-isolated; formats: contact, open collector, voltage
Recording intervals	1 ms, 2 ms, 5 ms (when using 1 ms/S-modules), 10 ms – 1 hour (22 selectable)
Storage media	SD card (SD / SDHC), USB drive
Display	7″ TFT colour LCD (800 × 480)
Alarm output	100 mΩ, 6pF typical
Power supply	AC (Z1014, 100–240 V), 2× battery pack (Z1007), 10–30 V DC externa

This temperature monitoring using k type thermocouple is indispensable to our passive thermal management study: recording the thermal behaviour of both modules and the ambient allows us to see how the PCM acts on heat redistribution, detect possible hotspots, and ensure safe operations. LR8450-01 is being able to drive an alarm output directly to the cycler and can guarantee that critical thermal events will be responded to in a very short time.

3.3 Experimental setup

In our experimental setup, we have two modules – one with PCM (4 cells with PCM spacers in between) and the other without PCM (4 cells with regular spacers in between). Each module is placed inside a 3D-printed PET (Polyethylene Terephthalate) battery enclosure designed to accommodate 4 cells with spacers. For the PCM-based module, honeycomb spacers are used to place between the cells which are filled with RT35HC phase-change material from the manufacturer Rubitherm and are then enclosed with baking sheets to

prevent any potential leakage during thermal cycling as shown in Fig 21. In the case of the module without PCM, wave-shaped spacers were placed between the cells, with drilled openings at the bottom to enable natural air convection and heat dissipation as shown in Fig 22. Following the module configurations, the experimental setup description proceeds with the arrangement for single cell testing and the 2S2P cell configuration.

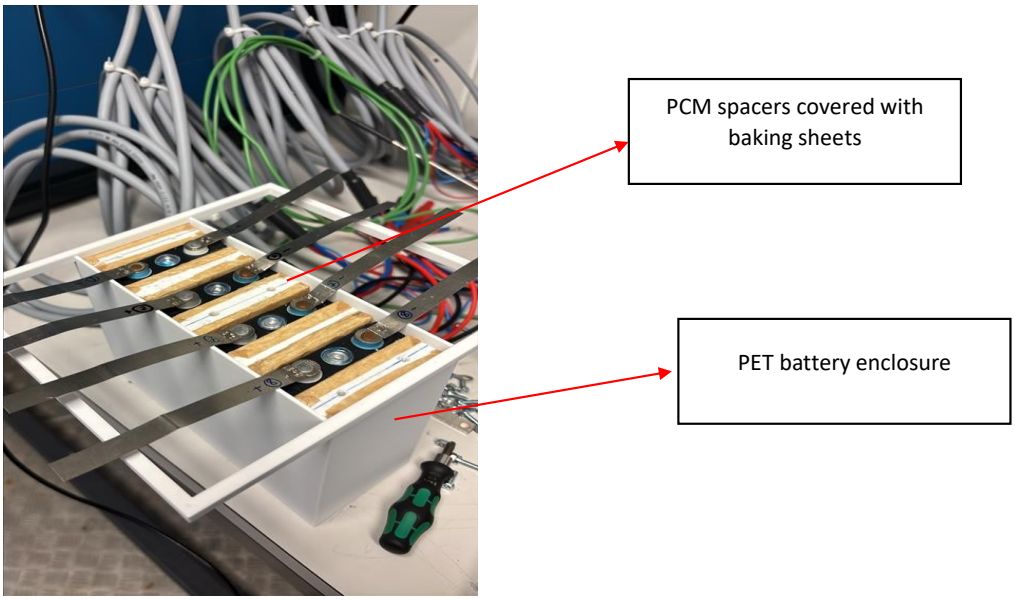

Figure 21: Single cell arranged with PCM spacer and PET housing

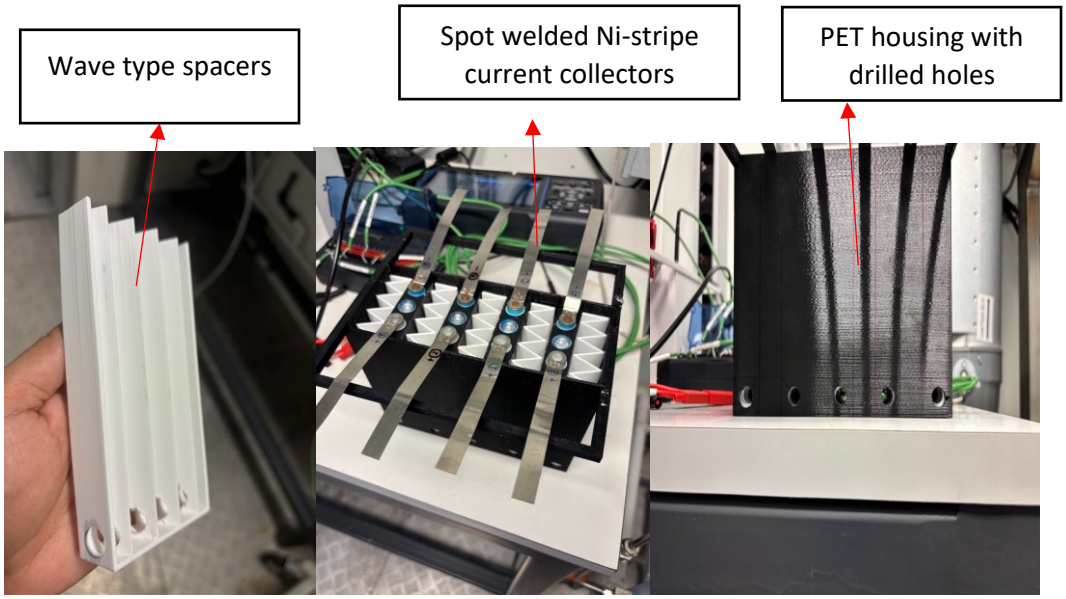

Figure 22: Single cells arranged with wave type spacers and PET housing

In the single-cell setup, eight individual battery cells are separately connected to the BCS-915, with one cell per channel without paralleling as shown in Fig 23. This setting enables each cell to be tested individually for the preliminary tests i.e. capacity, OCV, and GEIS (as discussed in Section 3.4.3 to 3.4.5) hence allowing the highly precise characterization of each cell's intrinsic electrochemical behaviour without interference from other cells. The main aim at this stage is to determine the health of the batteries, since these will be the same eight cells that later form the 2S2P modules, with 4 cells in the PCM module and 4 cells in the no-PCM module.

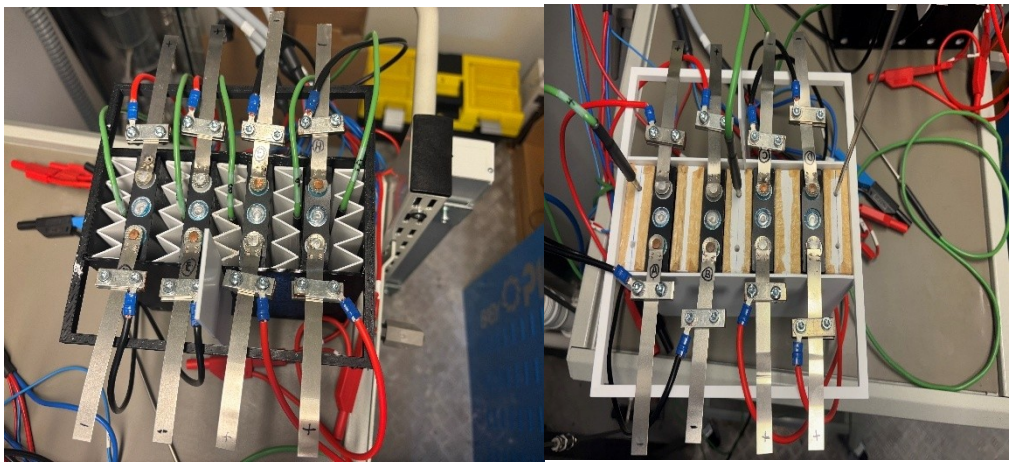

a) Single cells in No PCM module b) Single cells in PCM module

Figure 23: Single cell arranged for preliminary tests

After completing the preliminary analysis of the batteries, the cells are configured into a 2S2P arrangement, forming two modules suitable for the NRTC test (Fig 24). To deliver the required current need for our 2S2P, we parallel channels 1-4 for the non-PCM module and channels 5-8 for the PCM module on the BCS-915, allowing us to reach up to 60A with 4 channels and to monitor both modules independently and simultaneously. This configuration enables us to cycle and monitor each module (PCM vs. non PCM) with high precision and independence.

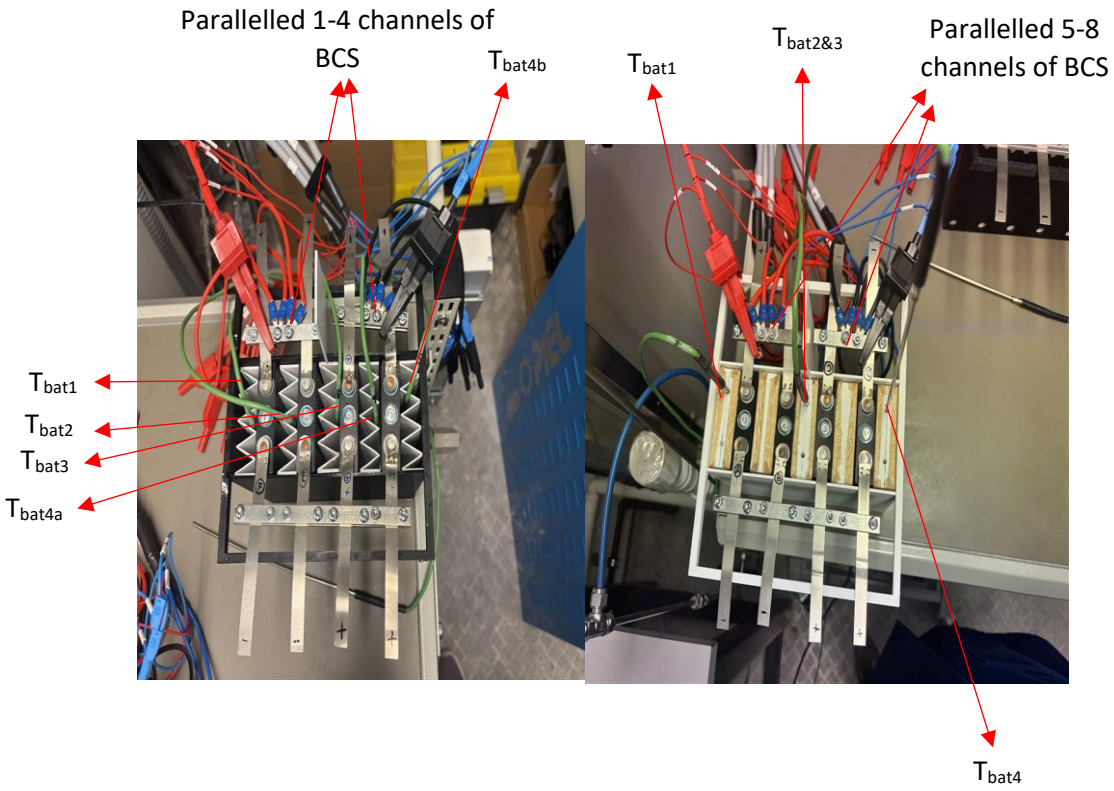

a) 2S2P without PCM b) 2S2P with PCM

Figure 24: Cell arrangement in 2S2P configuration for both modules

In this experimental setup, we use 10 temperature channels on the LR8450-01: channels 1-5 (T_{bat1}, T_{bat2}, T_{bat3}, T_{bat4a}, T_{bat4b} i.e. 5 temperature sensors for 4 batteries) monitor the module without PCM, channels 6-8 (T_{bat1}, $T_{bat2\&3}$, T_{bat4} i.e. 3 temperature sensors for 4 batteries) monitor the module with PCM as shown in Fig 24, and channels 9-10 (T_{amb1} and T_{amb2}) measure the ambient temperature as shown in Fig 25. The sensors are measuring the cell surface temperature in the non-PCM module and the PCM temperature in the PCM module. The measurements are saved every 1 second, and we configure an alarm to trigger if any battery temperature rises above 45 °C. This alarm is wired to the BCS-915's analog input via the external control terminal, so that when the threshold is exceeded, the cycler immediately stops, providing a real-time safety shut-down. Entire experimental setup is as shown in Figs 25 and 26.

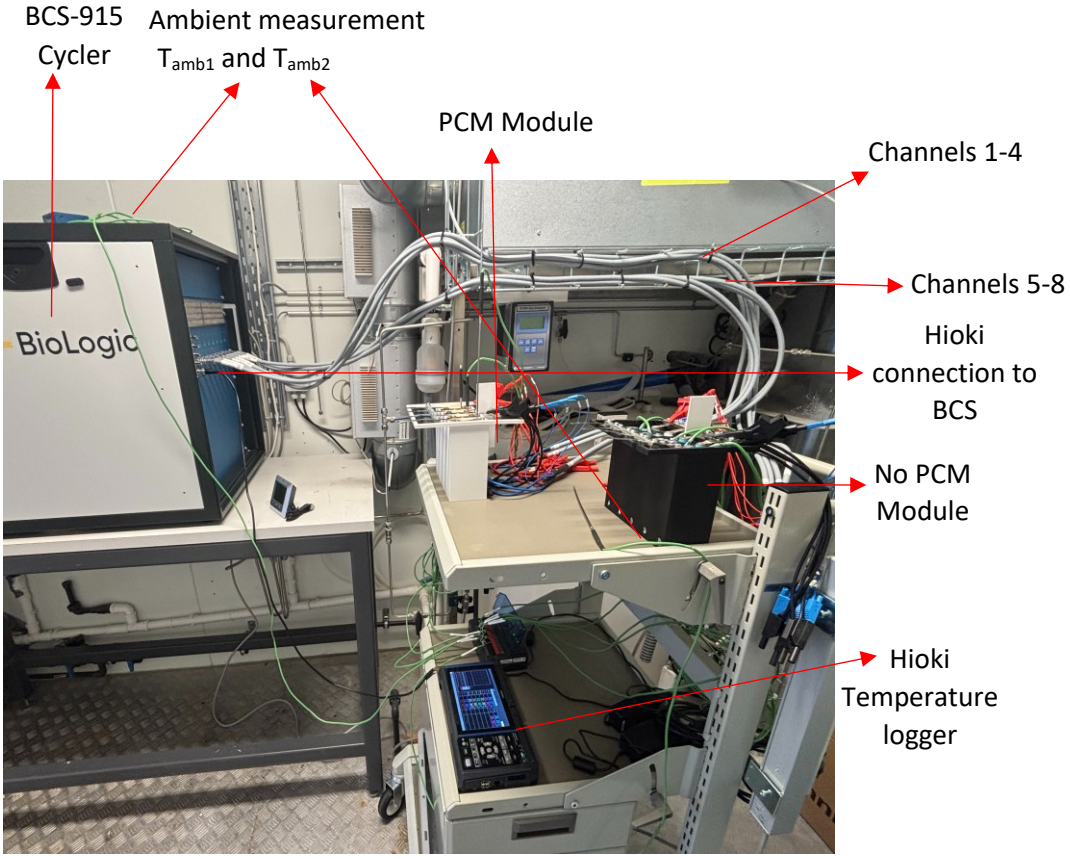

Figure 25: NRTC test experimental setup

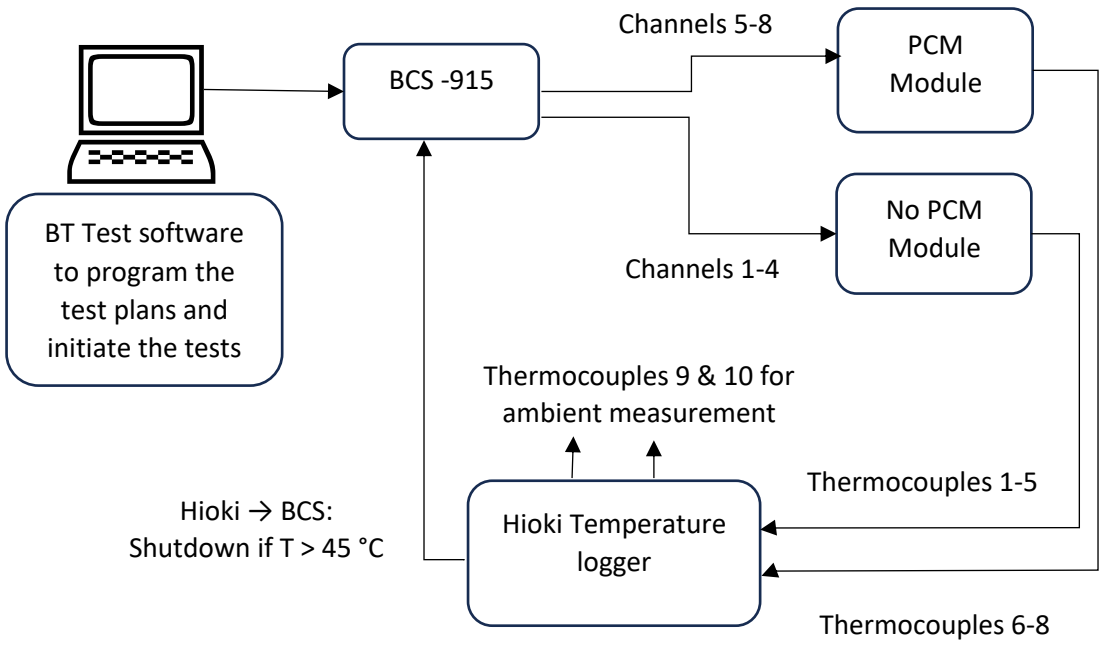

Figure 26: Schematic of the experimental setup

3.3.1 Thermal sizing of PCM and battery module

In this experiment, we have used 5 honeycomb structured spacers for the PCM module, and the mass of PCM m_{PCM} used in the module is given by the equation:

$$m_{PCM} = V_t \times \rho_{PCM} \quad (5)$$

Where, V_t is the total volume of the PCM spacers

ρ_{PCM} is liquid density of PCM

Assuming if the battery cells and the PCM absorb all the heat generated, with no heat losses to the ambient during continuous charge (1.5C)-discharge (2C) cycling over a specified operating period before a rest, and the cell temperature is required to remain below 45 °C throughout this interval. Under these conditions, the total heat generation in the module is described by the sum of the irreversible and reversible heat contributions, which are given by [Murashko et al., 2020]:

$$P_i = nR_{int}I^2 \quad (6)$$

$$P_r = -nIT\frac{dOCV}{dT} \quad (7)$$

Where, n is number of batteries used in PCM module

R_{int} is the internal resistance of the battery

I is the applied current

T is the battery temperature

OCV is the open-circuit voltage.

As the determination of $\frac{dOCV}{dT}$ is practically difficult, and [Yuan et al., 2024] show that the reversible heat is usually small when compared to irreversible heat, hence it is neglected.

As P_{rev} is neglected, only P_{irr} is considered for heat generation, and it is given by the equation:

$$Q_i = P_i \times \Delta t \quad (8)$$

where, Δt is the time interval over which heat is generated.

Heat absorbed by the battery cells $Q_{sens,bat}$ is given by the equation:

$$Q_{sens,bat} = nm_{bat}c_{bat}\Delta T \quad (9)$$

where, m_{bat} is mass of the battery

ΔT is temperature rise of the battery

c_{bat} is the specific heat capacity of the battery

Heat absorbed by the PCM $Q_{tot,PCM}$ is given by the equation:

$$Q_{t,PCM} = Q_{sens,PCM} + Q_{lat,PCM} \quad (10)$$

Where $Q_{sens,PCM}$ is sensible heat of PCM, $Q_{sens,PCM} = m_{PCM}c_{PCM}\Delta T$ (11)

$Q_{lat,PCM}$ is latent heat of PCM, $Q_{lat,PCM} = m_{PCM}f_m\Delta H_{PCM}$

$$Q_{t,PCM} = m_{PCM}(c_{PCM}\Delta T + f_m\Delta H_{PCM}) \quad (12)$$

Where, c_{PCM} is specific heat capacity of PCM

ΔH_{PCM} is latent heat of fusion of PCM

f_m is the melt fraction of the PCM and is assumed to be $f_m = 1$

The input parameters used for these calculations are given in below Table 8:

Table 8: Input parameters for PCM and battery thermal sizing

Parameter	Value	Source/Note
Total Volume of the PCM Spacer	10.39 mm	Appendix 3
Liquid density of PCM, ρ_{PCM}	0.77 kg/dm^3	Appendix 2
Number of batteries, n	4	Experimental Setup 3.3
Mass of the battery, m_{bat}	0.32 kg	Appendix 1
Specific heat of the battery, c_{bat}	0.83×10^3 Jkg^{-1}K^{-1}	Appendix 1
Internal resistance of the battery, R_{int}	3 mΩ	Appendix 1
Current applied to single cell, I	28 A	2C-rate charging current
Temperature rise of the battery, ΔT	20K (25-45°C)	Assumption
Time taken for CC charging, Δt	1618 s	Time taken for CC charging
Specific heat capacity of PCM, c_{PCM}	2 kJ kg^{-1}K^{-1}	Appendix 2
Latent heat of fusion of PCM, ΔH_{PCM}	240 kJ kg^{-1}	Appendix 2

Using the above Eqs. (5)-(12) and input parameters from Table 8, the calculated values are shown in Table 9 and detailed calculations can be found in Appendix 3.

Table 9: Calculated thermal sizing of PCM and Battery

Parameter	Value
Mass of the PCM, m_{PCM}	0.45 kg
Irreversible heat generation power, P_i	9.048 W
Heat absorbed by the battery cells $Q_{sens,bat}$	5.9 Wh
Sensible heat of PCM, $Q_{sens,PCM}$	5.04 Wh
Latent heat of PCM, $Q_{lat,PCM}$	30 Wh
Heat absorbed by PCM, $Q_{t,PCM}$	35.04 Wh

Table 9 indicates that, if heat losses to the surroundings are neglected, the available PCM mass is sufficient to limit the cell temperature rise to approximately 20 °C above ambient for about 4 h 21 minutes under continuous 2 C charge-discharge cycling, corresponding to an ohmic heat generation power of P_{irr} = 9.048 W and a combined thermal capacity of the batteries and PCM of $Q_{sens,\,bat} + Q_{t,PCM} \sim 41$ Wh.

3.4 Battery testing methodologies

In this section, we will learn about various battery test methodologies used in this experiment. Before we start the main experiments, it is essential to conduct certain preliminary tests on the batteries to determine the battery's initial health and their performance. These pre-tests: capacity, OCV and GEIS provide a detailed baseline for the cell's initial state and ensures that the subsequent experiments are more reliable and reproducible. Once these pre-tests are completed, the main NRTC test is conducted which is the core of this research. Along with these, it is also essential to learn about the basic charging / discharge protocols like CC-CV charge and CC charge/discharge.

3.4.1 CC-CV (Constant current - Constant voltage) charge

The CC-CV charging protocol is an industrially accepted procedure for lithium-ion batteries. The battery voltage rises linearly until it hits a cut-off value-for example 4.2 V per cell.

When that voltage is achieved, the charger changes to the CV mode. In that mode, the voltage is maintained constant, while the current decreases slowly because the battery approaches full charge. The completion of charge normally occurs when the current drops below some small cutoff, such as C/10. This two-step approach provides a reasonable compromise: the CC segment allows for the rapid bulk charging of the cells, while the CV segment permits safe topping without overvoltage and thus allows full capacity to be reached and maximizes life.

3.4.2 CC (Constant Current) charge and discharge

In CC mode, the current is kept constant during either charging or discharging, irrespective of the batteries' voltage. In charging applications, CC provides the ability for quick charge input up to a specified voltage cutoff. Testing usually utilizes CC discharge to determine a battery's capacity: discharging at a constant current to a specified lower voltage limit accurately measures how much charge the battery holds. Although operation in CC mode is simple and effective, relying on CC charging alone, without a subsequent CV phase, risks overcharging, while CC discharge to voltages that are too low can result in irreversible degradation if not properly controlled.

3.4.3 Capacity test

The capacity test measures the charge-storing capability of the battery under controlled conditions. By CC charging and discharging the cell with known currents, we measure the total amount of charge in ampere-hours or watt-hours that the cell can provide. This measured capacity serves for the calibration of the experimental protocol (for instance, defining the proper depth of discharge for successive cycles). Further, it also helps in diagnosing possible degradation from expected performance over the course of the tests.

3.4.4 Open-Circuit Voltage (OCV) test

The OCV test records the cell voltage by applying a small current after having a certain rest period. This test helps to map SoC versus voltage relationship which is important for good

battery modelling and monitoring. Furthermore, the OCV-SOC characteristic is abnormal in cases of self-discharge or leakage, for example, which provides insight into cell health before further testing.

While true open-circuit voltage (OCV) is measured with no external current, in practice we apply a very low current (300 mA) to approximate the OCV value. This "pseudo-OCV" method minimizes polarization effects and allows the voltage to closely reflect the equilibrium potential, while keeping the measurement time reasonable.

Initially Capacity and OCV tests are conducted as a single experiment for all the eight cells individually with the test plan as shown in Table 10. Safety limits for these tests are set as: Umin $\leq$ 2.8V, Umax $\geq$ 4.3V and I $\geq$ 15 A.

Table 10: Test plan for Capacity and OCV test

Test	Step	Task	Duration/Limit	Purpose
Capacity Test	1	CC-CV charge	CC with 7 A until 4.2 V, then CV until current falls to 500 mA	Measure full charge capacity
	2	Rest	15 min	Allow cell to stabilize thermally / electrochemically
	3	CC discharge	7 A until 3.0 V	Measure usable capacity on discharge
	4	Rest		Recovery before next cycle
OCV Test	1	CC discharge	300 mA until 3.0 V	Low-current steps to approximate open-circuit voltage
	2	Rest	1 min	Letting the voltage to settle slightly
	3	CC charge	300 mA until 4.2 V	Bring to full charge slowly
	4	Rest	30 min	Allow equilibrium to approach true OCV
	5	CC discharge	300 mA until 3.0 V	Step discharge to see OCV behaviour
	6	Rest	30 min	Let cell re-equilibrate

3.4.5 Galvanostatic Electrochemical Impedance Spectroscopy (GEIS) test

Galvanostatic electrochemical impedance spectroscopy applies a small alternating current across a range of frequencies and measures the voltage response. This test investigates internal electrochemical processes such as charge-transfer resistance, diffusion processes, and double-layer capacitance, where the high-frequency resistance (HFR) is defined as the real impedance at the point of zero imaginary impedance (high-frequency intercept on the Nyquist plot's real axis). The obtained impedance spectrum provides the basis necessary for equivalent circuit modelling and for the evaluation of internal cell states. The feasibility of detecting increased internal resistances or other anomalies beforehand, which may affect long-term performance or safety, is enabled by performing GEIS before experiments.

Capacity and OCV tests are followed by GEIS test as per the test plan in Table 11, with the safety limits set as: Umin ≤ 2.8V, Umax ≥ 4.3V and I ≥ 15 A.

Table 11: Test plan for GEIS test

Test	Step	Task	Duration/Limit	Purpose
Impedance spectroscopy (GEIS)	1	CC-CV charge	CC with 7 A until 4.2 V, then CV until current falls to 500 mA	Prepare 100% SoC
	2	Rest	15 min	Let the cell equilibrate at 100% SoC
	3	Galvanostatic frequency sweep + EIS	10 mHz → 10 kHz (log scale), Amplitude =1 A, Nd = 10, Na = 1, pw = 0.1, drift correction off	Record impedance spectrum at 100% SoC
	4	CC discharge	7 A until ~50% SoC (t = 1 h)	Move to mid SoC for second EIS measurement
	5	Rest	30 min	Stabilize at 50% SoC
	6	Galvanostatic frequency sweep + EIS (repeat)	Same as step 3	Record impedance spectrum at 50% SoC
	7	Rest	30 min	Final stabilization after EIS

3.4.6 Non-Road Transient Cycle (NRTC) test

The experimental work focuses on the NRTC test. Non-Road Transient Cycle is a standard transient test cycle originally developed for nonroad machines as shown in Fig 28, defined by ISO 8178-4 and used in global regulatory frameworks. This cycle lasts for about 1,238 seconds with currents that vary with respect to each time interval [Diesel Net, n.d.; Transport Policy, n.d.; UNECE, 2011]. In an engine test cell, normalized speed and torque profiles are "denormalized" to match the characteristics of the engine under test, and the test is executed [UNECE, 2011].

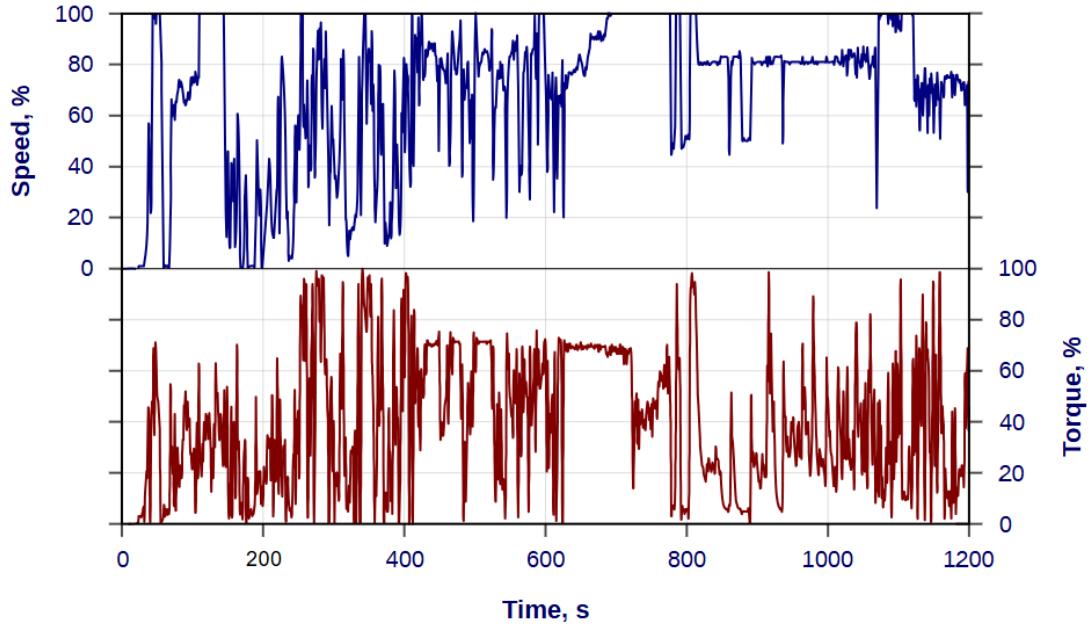

Figure 27: Normalized speed and torque over NRTC cycle, adapted from [DieselNet, n.d.]

In the framework of this thesis, NRTC simulates realistic transient load conditions analogous to non-road machinery by converting the standardized normalized engine speed ($v_{norm(t)}$) and torque profile ($\tau_{norm(t)}$) (as shown in Fig 27) through denormalization using the specific engine's maximum torque curve ($\tau_{max(v(t))}$) and rated speed (v_{rated}) into equivalent battery current ($I_{bat(t)}$) demands that reflect the power requirements of electrified NRMM operation by using below Eqs. (13)-(16) [40 C.F.R. Part 1065, 2005; Di Luca et al., 2020]. This approach enables investigation of battery performance, temperature behaviour, degradation, and possibly emissions-relevant behaviours under those cycles. For one NRTC discharge, the resulting average power P_{ave} is given by:

$$P_{avg} = x\%P_{max} \quad (13)$$

Where, P_{max} is maximum Power reached during the NRTC discharge

x% is the ratio of average to maximum power and x% ≈ 29%

Now, Power and Battery current conversion:

$$\text{Engine Power demand, } P_{eng(t)} = \frac{2\pi \times v(t) \times \tau(t)}{60 \times 1000} \quad (14)$$

$$\text{Battery Power, } P_{bat(t)} = \frac{P_{eng(t)}}{\eta} \quad (15)$$

$$\text{Battery Current, } I_{bat}(t) = P_{bat}(t)/U_{bat}(t) \quad (16)$$

As variable current discharge was used for the battery cycler, the voltage effect was neglected and Ibat was directly correlated to the engine power and therefore is given by:

$$I_{bat}(t) = aP_{bat}(t)$$

Where, η is powertrain efficiency

U_{bat} is Battery voltage

t is the time

a is proportionality factor and is selected such that the Pmax corresponds to 2C discharge.

For the NRTC experiments, the cells are configured in a 2S2P arrangement. Before starting the full NRTC, we perform preliminary charge-discharge cycles at 1C and 1.5C to condition the modules and then proceed to the NRTC test using our designed protocol as per the test plan in Table 12 and Table 13 respectively. Safety limits for these tests are set as: Umin ≤ 5.6V, Umax ≥ 8.6V and I ≥ 60A.

Table 12: Charging and discharging protocol at 1C and 1.5C for 2S2P configuration

Test	Step	Task	Duration/Limit
	1	Rest	2 min
3 Cycles @ 1C	2	CC-CV charge	CC with 1C (28 A) until 8.4 V, then CV until current falls to 1 A
	3	Rest	15 min
	4	CC discharge	1C (28 A) until 6.0 V
	5	Rest	15 min
2 Cycles @ 1.5C	1	Rest	2 min
	2	CC-CV charge	CC with 1.5C (42 A) until 8.4 V, then CV until current falls to 1 A
	3	Rest	15 min
	4	CC discharge	1.5C (42 A) until 6.0 V
	5	Rest	15 min

For the NRTC cycle, we upload a csv file which contains the time profile until 1,238 seconds with currents that vary with respect to each time interval. Current values are specified at an interval of 0.5s (i.e., the 0.5 s and 1 s values are identical). The maximum current value chosen was -56 A (2C discharge) with an average current of -15.86A (0.58C-rate). Five loops were grouped within one NRTC discharge i.e. in “AUP” (Table 13) to make sure complete depletion of the battery.

Pre-tests provide initial characterization of capacity, voltage-SoC curves, and internal impedance, while NRTC cycling stresses the battery under realistic transient non-road duty conditions. Combining these establishes a solid baseline for interpreting NRTC-induced effects on degradation, thermal behaviour, efficiency, and other performance metrics.

Table 13: NRTC test plan for 2S2P configuration

Test	Step	Task	Duration/Limit	Purpose
NRTC Test	1	CC-CV charge	CC with 1.5C (42 A) until 8.4 V, then CV until current falls to 1 A	Ensuring battery is fully charged before it starts discharging with NRTC profile
	2	Rest	15 min	Stabilizing the module
	3	LOOP	50 Cycles of Steps 4-7	To study the transient load conditions, 50 cycles are required
	4	AUP (Apply CSV profile)	I Range 40 A, Time format = TIME, Scale = 1.8667, Loop = 5 Cycles	Apply scaled NRTC current profile from CSV (original 30 A max scaled to 56 A), 5 loops for full discharge
	5	Rest	15 min	Stabilizing the module
	6	CC-CV charge	CC with 1.5C (42 A) until 8.4 V, then CV until current falls to 1 A	charging the battery again before it starts discharging with NRTC profile
	7	Rest	15 min	Stabilizing the module

4 Results

This section discusses the key results obtained from the battery testing like initial characterisation, their thermal response to different cycling conditions (with and without PCM) and NRTC duty cycle on PCM module and the metrics of the batteries post-NRTC.

4.1 Initial characterization test results: capacity, OCV and GEIS

4.1.1 Initial capacity test results

Fig 28 shows the initial constant-current discharge capacity (Q) for each of the eight cells at 1/2 C-rate i.e. 7A. The discharge capacities after NRTC are spread between 14.56 Ah and 15.13 Ah, with an average of around 14.92 Ah and a standard deviation of about 0.18 Ah, indicating small variation and good consistency among the cells. While the nominal cell capacity is 14 Ah, the measured capacity of some cells slightly exceeds the nominal capacity, this is typical for manufacturer tolerances and indicates the cells were tested in a fresh state. This small variation in capacity indicates all eight cells will have similar performance under identical cycling conditions and thus all are suitable for assembly into the 2S2P modules used in the passive thermal management experiments.

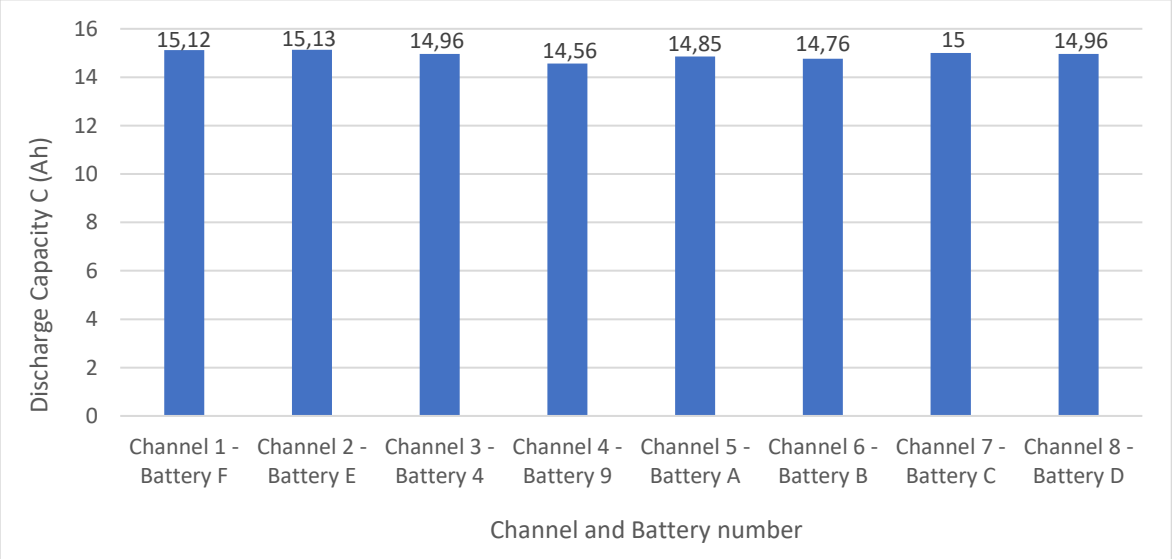

Figure 28: Initial discharge capacities of experimental batteries before NRTC

4.1.2 Initial OCV test results

Fig 29 presents the open-circuit voltage behaviour for the eight battery cells derived from the low-current step OCV test. In this test, each cell was first discharged at a constant current of 300mA to 3.0V, followed by short rest periods and subsequent low-current charging and discharging steps with intermediate rests to let the terminal voltage relax towards open-circuit conditions. However, there is an error in the implemented OCV test protocol: the test was stopped after 48 h, and during the final constant-current charging step at 0.3 A the maximum cell voltage reached only about 4.11 V, meaning that the cells were not fully charged and the OCV curves are therefore incomplete. This limitation is also visible in Fig. 29, where the voltage-SOC curved do not extend up to the nominal upper-cutoff voltage of 4.2 V. Because of this protocol error and the resulting incomplete OCV profiles, the discharge capacities originally extracted from the OCV test are not reported.

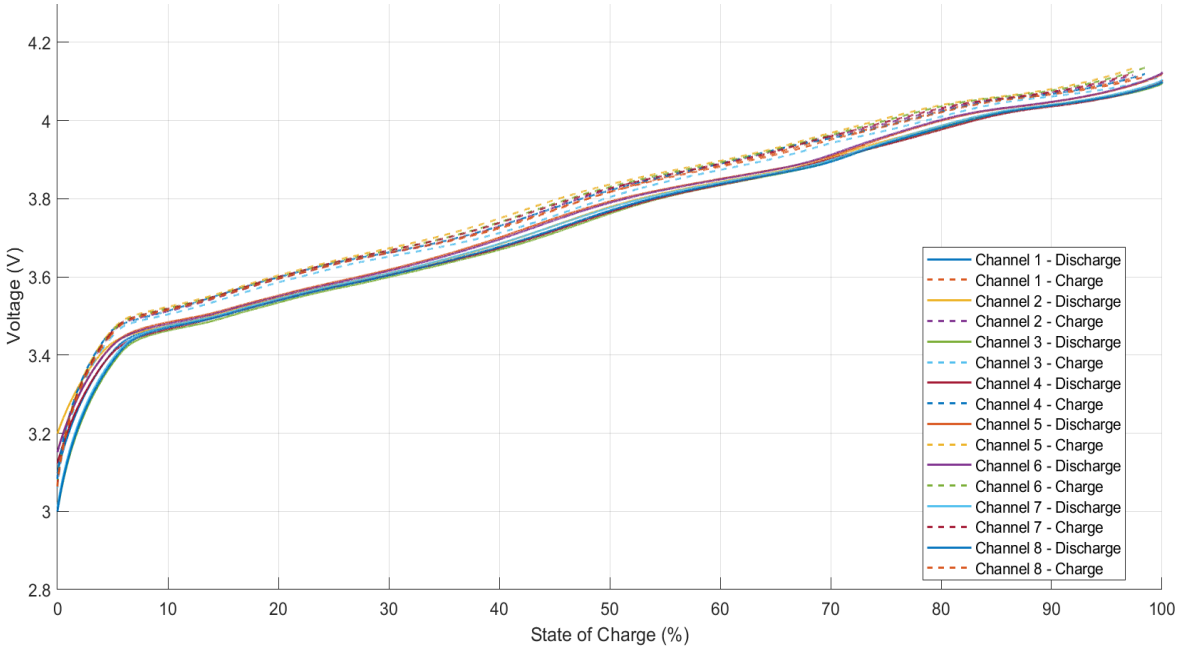

Figure 29: Charge and Discharge Curves - Voltage vs SOC

4.1.3 Initial GEIS test results

Fig 30 presents the results for the GEIS test performed on the eight cells measured at 100% SOC. The Nyquist plots' high-frequency resistance (HFR) is in the range between 12.6 to 15.3 mΩ for all channels, with an overall mean of approximately 14.0 mΩ and a standard

deviation of about 0.9 mΩ, indicating moderate channel-to-channel variation. The diameter of the main semicircle reflects the combined charge-transfer and interfacial resistances and ranges between approximately 2-4 mΩ between the cells. No additional semicircles, secondary arcs, or long diffusion tails are observed, meaning that the charge transfer properties are uniform and there is minimal variance in the double-layer or mass-transport phenomena at full charge.

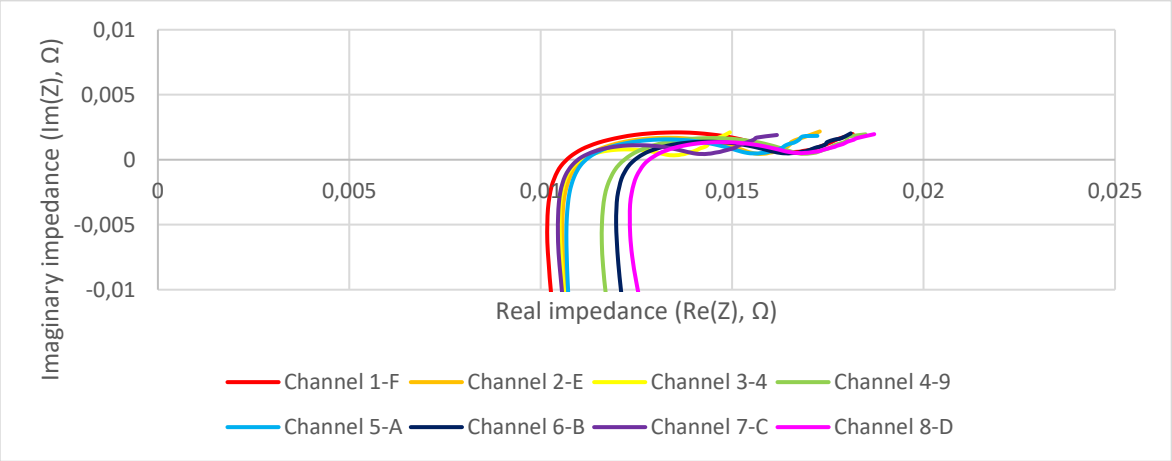

Figure 30: Nyquist plot of EIS at 100% SOC

In Fig 31, after the cells have been discharged to about fifty percent state of charge, the HFR range from 12.6 Ω to 15.0 mΩ, with a mean of about 13.8 mΩ and a standard deviation of roughly 0.9 mΩ, again indicating moderate channel-to-channel variation. There is also a slight reduction in the semicircle diameter due to small decrease of charge-transfer resistance typical for lithium-ion cells at mid-state of charge. In both measurement states, all eight cells show closely clustered impedance spectra with minor deviations, thus confirming consistent internal resistance characteristics. This resemblance also confirms that the batch is qualified to make balanced two-series-two-parallel modules and ensures that subsequent module-level tests reflect real experimental variables rather than outlier electrochemical behaviour.

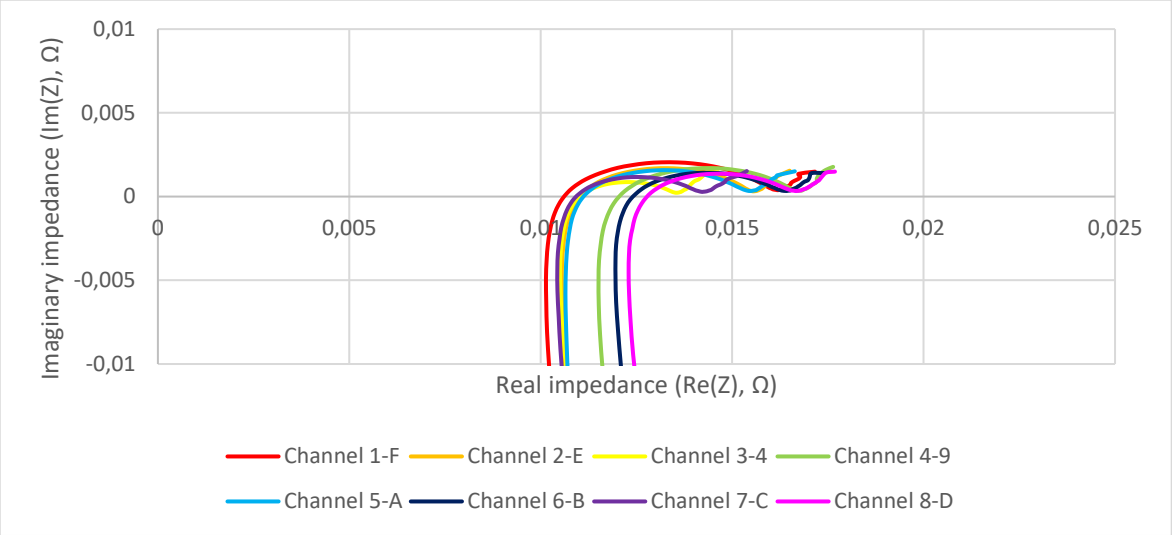

Figure 31: Nyquist plot of EIS at 50% SOC

4.2 Temperature response of 2S2P modules under 1C and 1.5C cycling with and without PCM

The thermal response of the PCM and non PCM 2S2P modules was evaluated using three consecutive 1C cycles and two 1.5C cycles as shown in Table 12. The third 1C cycle and the second 1.5C cycle were selected as representative, since the temperature profiles had stabilized by these cycles and the electrical behaviour was highly repeatable. For both PCM and non-PCM modules, the measured discharge capacities at 1C and 1.5C were almost identical between the two modules and close to the nominal value defined by the cycling protocol. The discharge cut-off voltage of 6.00 V was reached within about 10 mV (5.99-6.00 V) and the charge cut-off voltage of 8.40 V within about 1 mV (8.39-8.40 V) in all tests, indicating that both modules were cycled under comparable electrical conditions. These consistent electrical conditions ensure that any differences in temperature behaviour can be attributed to the presence or absence of PCM rather than to differences in loading. The temperature analysis focuses on the CC-CV charging steps of the representative cycles, because the highest cell temperatures in both modules occurred at the end of the CC-CV charge, whereas the previous constant current discharge phases produced lower peak temperatures and do not define the worst-case thermal conditions.

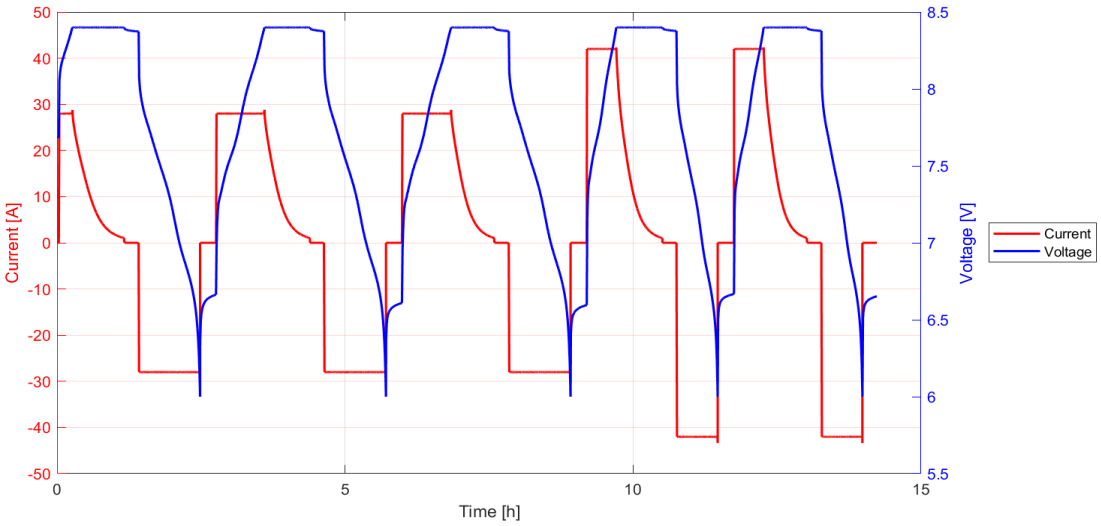

Figure 32: Current and Voltage Profiles of 2S2P modules at 3 cycles of 1C rate and 2 cycles of 1.5C rate

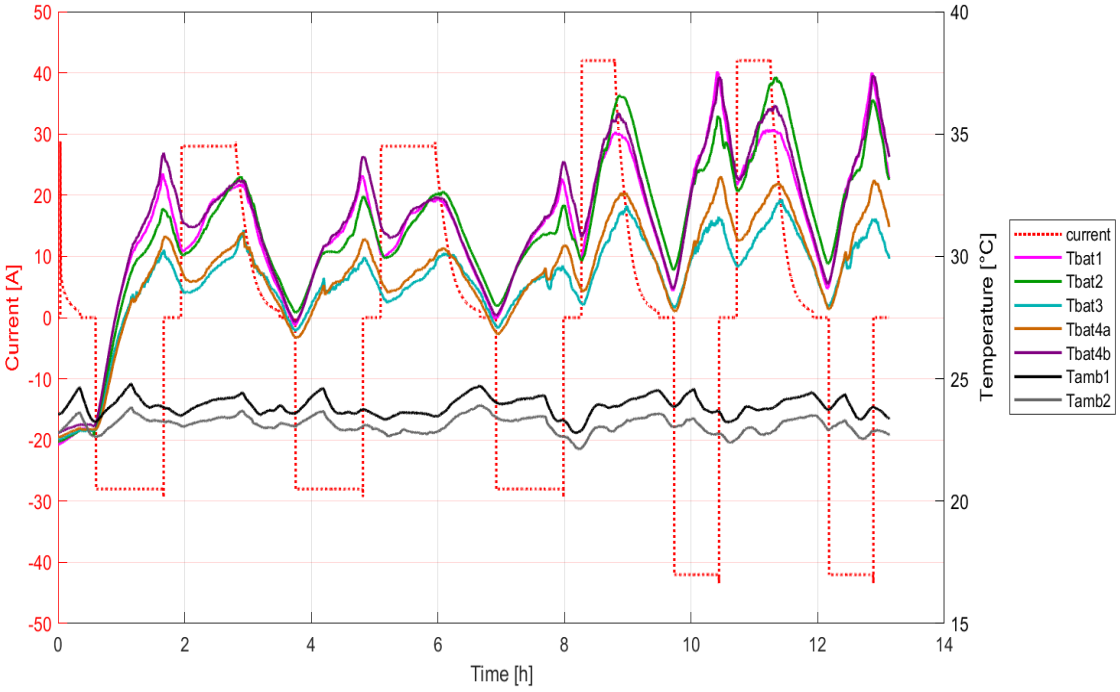

Figure 33: Current and Temperature Profiles of Non PCM module at 3 cycles of 1C rate and 2 cycles of 1.5C rate

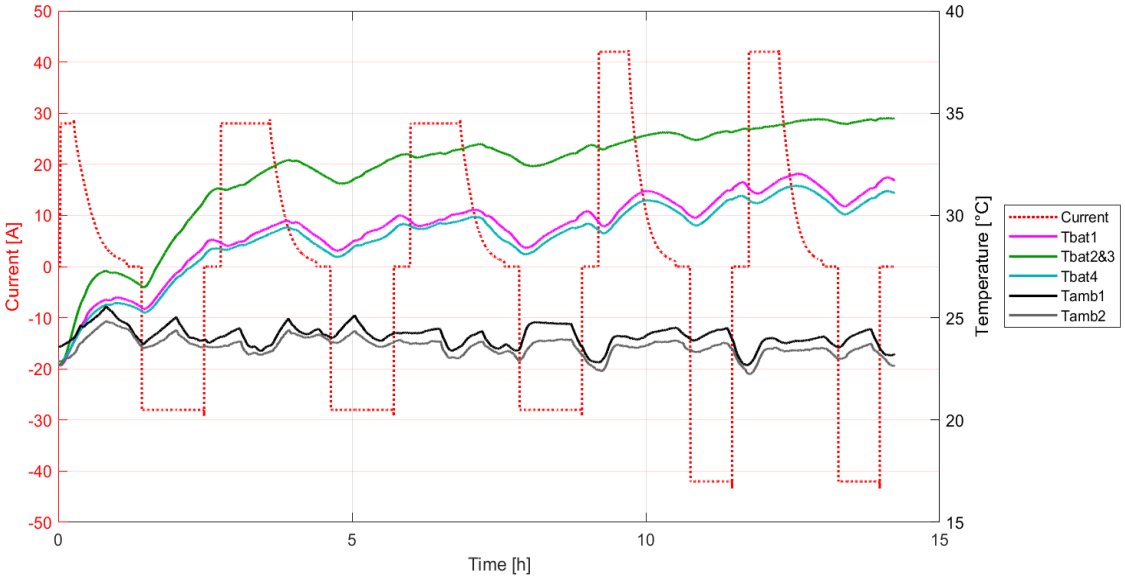

Figure 34: Current and Temperature Profiles of PCM module at 3 cycles of 1C rate and 2 cycles of 1.5C rate

At 1C, both modules operated in a similar temperature range and showed relatively small gradients. As shown in Fig 34, the maximum temperatures recorded during the CC-CV charge of cycle 3 in the PCM module were 30.28 °C, 33.49 °C and 29.94 °C at T_{bat1}, middle sensor $T_{bat2\&3}$, and T_{bat4} respectively. In this cycle, the average ambient temperature observed was 23.74 °C and the relative temperature rises above ambient were therefore 6.54 °C, 9.75 °C and 6.20 °C for T_{bat1}, $T_{bat2\&3}$ and T_{bat4}, respectively (Fig 35). In the non PCM module (Fig 33), the maximum temperatures of the five sensors were 32.35 °C (T_{bat1}), 32.64 °C (T_{bat2}), 30.14 °C (T_{bat3}), 30.35 °C (T_{bat4a}) and 32.42 °C (T_{bat4b}), with an average ambient temperature of 23.44 °C, and the corresponding temperature rises above ambient were 8.91 °C, 9.20 °C, 6.70 °C, 6.91 °C and 8.98 °C as shown in Fig 35. At this C rate, the overall sensor to sensor gradient was modest for both designs as shown in Table 14: in the PCM module the difference between the hottest and coolest sensor was 3.55 °C, while in the non PCM module it was 2.50 °C.

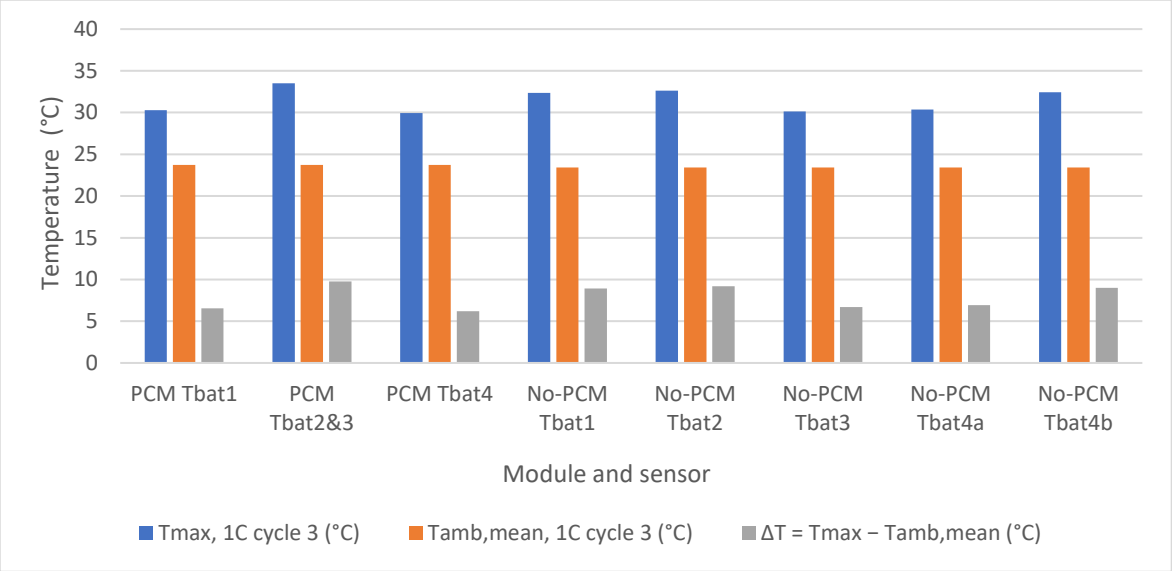

Figure 35: Maximum cell temperatures and temperatures rise above ambient during CC-CV charging at 1C (cycle 3) for PCM and non-PCM modules

Table 14: Sensor-to-sensor temperature gradients during CC-CV charging at 1C (cycle 3) for PCM and non-PCM modules

Module	Parameter	Value (°C)
PCM	$T_{max,\,hot} - T_{max,\,cool}$	3.55
PCM	$T_{bat2\&3,\,max} - T_{bat1,\,max\,(middle\,-\,edge)}$	3.21
PCM	$T_{bat2\&3,\,max} - T_{bat4,\,max\,(middle\,-\,edge)}$	3.55
No-PCM	$T_{max,\,hot} - T_{max,\,cool}$	2.5
No-PCM	$T_{bat1,\,max} - T_{bat3,\,max}$	2.21
No-PCM	$T_{bat2,\,max} - T_{bat3,\,max}$	2.5
No-PCM	$T_{bat4b,\,max} - T_{bat4a,\,max}$	2.07

The differences between the PCM and non-PCM modules became more noticeable at the higher 1.5C rate. In the PCM module (Figs 34 and 36), the maximum temperatures during the CC-CV charge of cycle 2 were 32.04 °C at T_{bat1}, 34.71 °C at $T_{bat2\&3}$ and 31.46 °C at T_{bat4}, with a mean ambient temperature of 23.53 °C. The corresponding temperature rises above ambient were 8.51 °C, 11.18 °C and 7.93 °C. In contrast, the non-PCM module (Fig 33), reached significantly higher temperatures under the same electrical conditions: T_{bat1}, T_{bat2}, T_{bat3}, T_{bat4a} and T_{bat4b} peaked at 35.19 °C, 37.31 °C, 32.33 °C, 33.01 °C and 36.17 °C, respectively, with a mean ambient of 23.52 °C. The resulting temperature rises above

ambient were 11.67 °C at T_{bat1}, 13.79 °C at T_{bat2}, 8.81 °C at T_{bat3}, 9.49 °C at T_{bat4a} and 12.65 °C at T_{bat4b} (Fig 36), showing that the non-PCM module operated several degrees hotter than the PCM module at this higher C-rate. The temperature differences were also larger in the non-PCM case as shown in Table 15: for the PCM module, the difference between the hottest and coolest sensor during CC-CV charging in cycle 2 was 3.25 °C, whereas in the non-PCM module the corresponding overall gradient reached 4.98 °C.

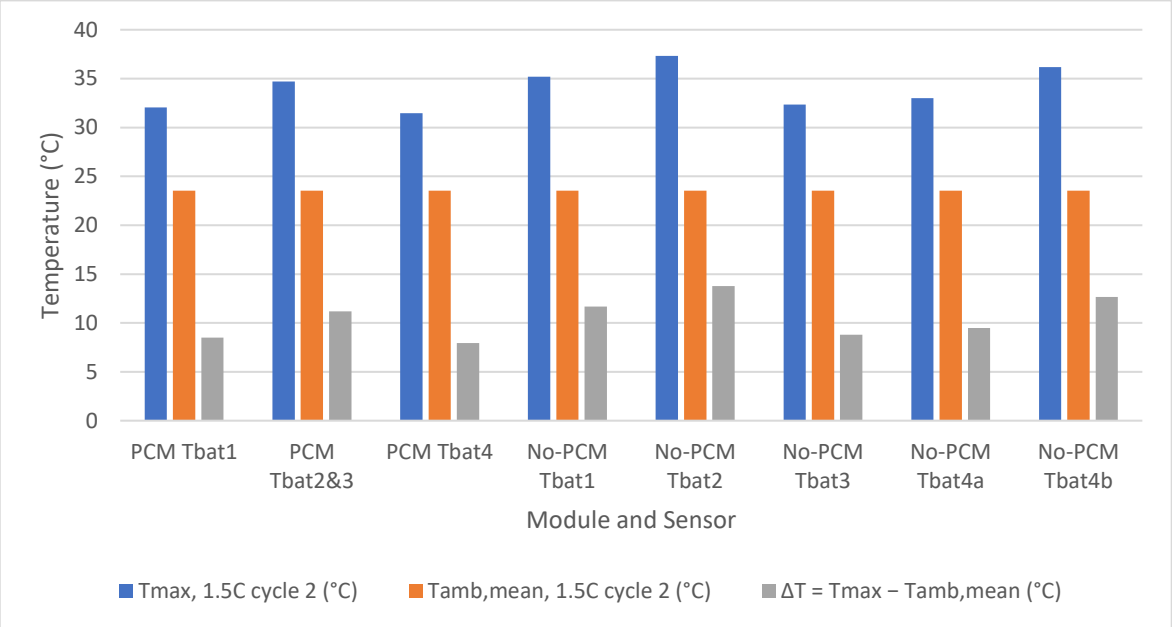

Figure 36: Maximum cell temperatures and temperatures rise above ambient during CC-CV charging at 1.5C (cycle 2) for PCM and non-PCM modules

Table 15: Sensor-to-sensor temperature gradients during CC-CV charging at 1.5C (cycle 2) for PCM and non-PCM modules

Module	Parameter	Value (°C)
PCM	$T_{max,\,hot} - T_{max,\,cool}$	3.25
PCM	$T_{bat2\&3,\,max} - T_{bat1,\,max\,(middle\,-\,edge)}$	2.67
PCM	$T_{bat2\&3,\,max} - T_{bat4,\,max\,(middle\,-\,edge)}$	3.25
No-PCM	$T_{max,\,hot} - T_{max,\,cool}$	4.98
No-PCM	$T_{bat1,\,max} - T_{bat3,\,max}$	2.86
No-PCM	$T_{bat2,\,max} - T_{bat3,\,max}$	4.98
No-PCM	$T_{bat4b,\,max} - T_{bat4a,\,max}$	3.16

The temperature differences between sensors can be explained by the physical layout of the two modules. In the PCM module, the middle sensor $T_{bat2\&3}$ is located between the two inner prismatic cells, so heat generated in both cells accumulates in this region before being redistributed through the PCM layer. As a result, $T_{bat2\&3}$ remains about 3-3.5 °C warmer than the edge sensors at both 1C and 1.5C, while the overall sensor-to-sensor temperature differences are limited to roughly 3-3.5 °C. In the non-PCM module, by contrast, the higher temperatures at T_{bat1}, T_{bat2} and T_{bat4b} compared to T_{bat3} and T_{bat4a} (T_{bat1} and T_{bat2} were 2.86 °C and 4.98 °C warmer than T_{bat3}, respectively, while T_{bat4b} was 3.16 °C warmer than T_{bat4a}) are not related to a middle-edge effect, but to their proximity to busbars and screw connections and to more shielded surfaces, where local ohmic/contact heating and reduced natural convection caused few degrees increase in surface temperature. These position-dependent effects become more pronounced at 1.5C, particularly in the non-PCM module, where the absence of PCM allows such local hot spots to develop more strongly, whereas in the PCM module the phase change material spreads heat more uniformly and reduces the sensitivity of surface temperature to exact sensor location.

Overall, CC-CV charging and CC discharging tests explain that at 1C both modules operate with similar peak temperatures and have small gradients, but at 1.5C the non PCM module shows high temperature rises above ambient and larger cell to cell differences than the PCM module. At 1C, the highest temperature observed in the PCM module was 33.49 °C compared with 32.64 °C in the non PCM module, showing that the effect of PCM on higher temperature is low at this C rate. At 1.5C, the PCM module reached a maximum temperature of 34.71 °C, while the non PCM module reached 37.31 °C. The maximum temperature of the PCM module therefore remained just below the PCM (RT35HC) melting point of approximately 35 °C, so only limited latent-heat buffering was activated at this C-rate. Hence, PCM reduces the maximum cell temperature by approximately 2.60 °C at higher C-rates. Compared to ambient, the hottest PCM sensor rose about 11.20 °C above ambient, whereas the hottest non PCM sensor rose about 13.80 °C, so the PCM layer reduced the maximum temperature rise by roughly 2.50-3.00 °C while also limiting the temperature gradients among the batteries to around 3 °C instead of nearly 5 °C. These observations confirm that the PCM layer moderates hot spot formation and reduces temperature non uniformity within the module under higher cycling rate, providing a clear advantage for passive thermal management.

4.3 Temperature response of 2S2P modules under NRTC duty cycle with PCM Module

The thermal behavior of the PCM-equipped 2S2P module was further investigated under a non-road transient cycle (NRTC) representative of realistic mobile machine operation. In this test, the module was subjected to 20 consecutive NRTC discharge (2C, 56A)-CC-CV charge (1.5C, 42A) cycles over a total duration of approximately 70 h, while current ,voltage, three cell temperatures and two ambient temperatures were recorded continuously. One stabilized cycle (cycle 3) is first analyzed in detail to characterize the electro-thermal response within a single NRTC event, after which the evolution of peak temperatures and temperature gradients over all 20 cycles is examined to assess the long-term performance of the passive PCM-based thermal management. Due to BCS-915 cycler's instrument errors and the practical limitation on charging at no more than 1.5C especially for more demanding current operation, even for single-module tests, NRTC cycling was carried out only on the PCM module. This allowed us not to repeat these tests on the non-PCM module and limited the possibility to compare the thermal and degradation performance under equal stress conditions of both modules. The NRTC cycles were thus restricted to 20 and the charging/discharging protocols were restricted to 1.5C and 2C respectively.

In the third experimental cycle, the 2S2P PCM module was subjected to one complete NRTC discharge followed immediately by a CC-CV recharge and a short rest, giving a total third cycle duration from 3 h 26 min. As shown in Fig 37, during the NRTC phase, the current followed a highly transient profile between approximately 0 A and a peak of −54.88 A, corresponding to a 2C discharge, while the module voltage decreased towards a minimum of 6.54 V.

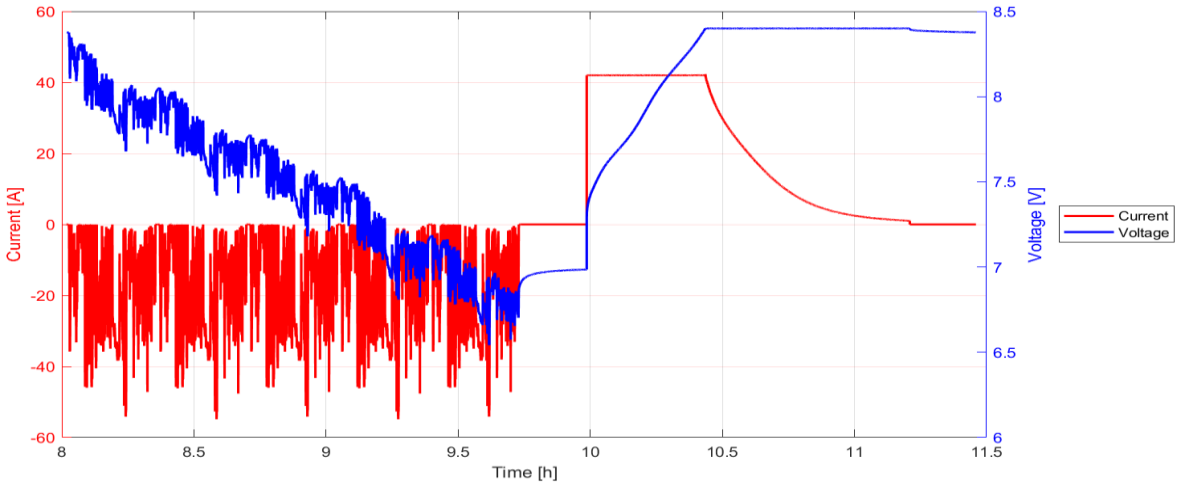

Figure 37: Current and Voltage Profiles of PCM module at 2C NRTC discharge and 1.5C CC-CV charge for 3rd cycle

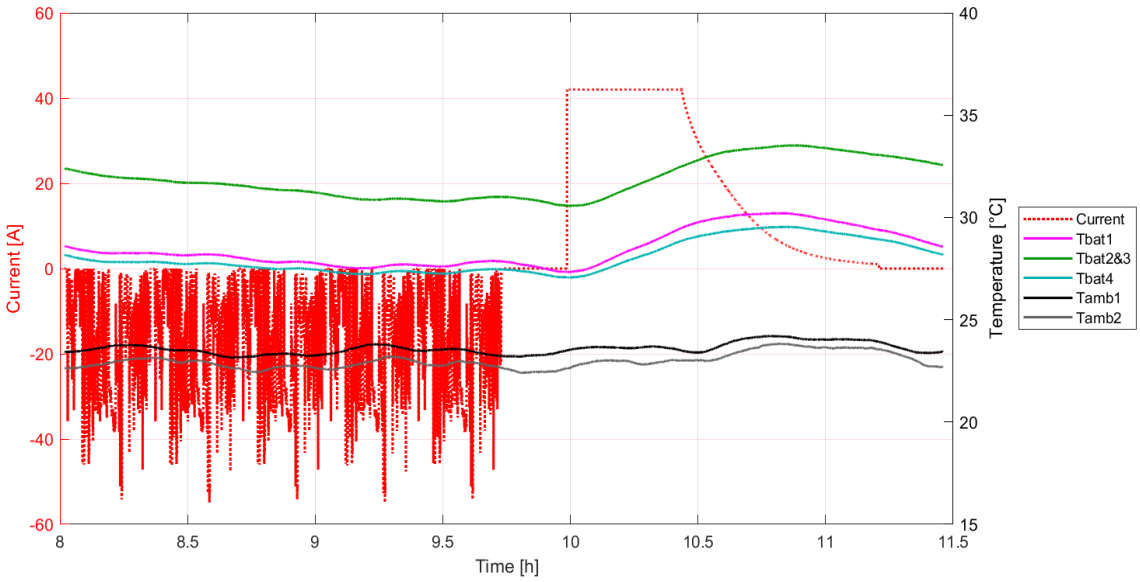

Figure 38: Current and Temperature Profiles of PCM module at 2C NRTC discharge and 1.5C CC-CV charge for 3rd cycle

The temperature response closely followed these electrical loads. As shown in Fig 38, at the start of the NRTC discharge, the cell temperatures were already above ambient because of prior cycling, with T_{bat1}, $T_{bat2\&3}$ and T_{bat4} measuring 28.60 °C, 32.38 °C and 28.16 °C, respectively, compared with 23.42 °C and 22.64 °C at the two ambient sensors. During the NRTC discharge, the temperature decreased because the average NRTC power (0.58C) was less than the charging power (1.5C), and the highest temperatures of the cycle occurred during the CV charging period, when continuous 1.5C charging produced sustained internal heat generation. At this stage, the middle thermocouple $T_{bat2\&3}$, between the inner cells

reached a maximum temperature of 33.53 °C, whereas the edge sensors T_{bat1} and T_{bat4} reached 30.15 °C and 29.51 °C. The relative ambient temperature was 23.92 °C and therefore, the maximum temperature rise above ambient in this cycle was 9.61 °C at the middle and 6.23 °C and 5.59 °C at the two edges.

The temperature differences at the peak stages were small i.e., the middle sensor was only 3.38 °C hotter than T_{bat1} and 4.02 °C hotter than T_{bat4}, even though it was located between the two inner cells where heat accumulation is expected. Ambient temperatures were constant, with an average of 23.82 °C and varied roughly 1 °C over the cycle.

4.3.1 NRTC cycling (20 cycles) of PCM module

Over the full sequence of 20 NRTC cycles, the PCM module exhibited stable electro thermal behavior, with no significant drift in peak temperature, temperature gradients or electrical performance. The five representative cycles 1, 5, 10, 15 and 20 summarize this behavior well. In these cycles, the NRTC discharge capacity remained essentially constant at about 27.27-27.28 Ah, while the subsequent CC-CV charge returned approximately 45.15-45.86 Ah. The minimum voltage during NRTC stayed in the narrow range 6.53-6.55 V and the maximum voltage during CC-CV was 8.40 V as shown in Fig 39, indicating highly repeatable electrical loading and recharging conditions across the test.

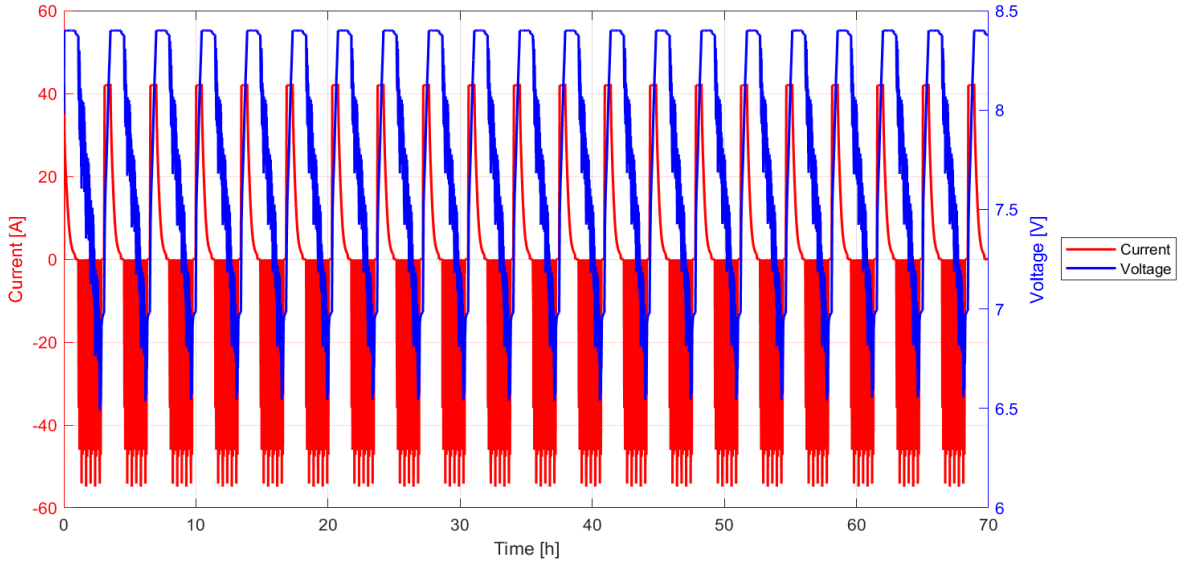

Figure 39: Current and Voltage Profiles of PCM module at 2C NRTC discharge and 1.5C CC-CV charge for 20 cycles

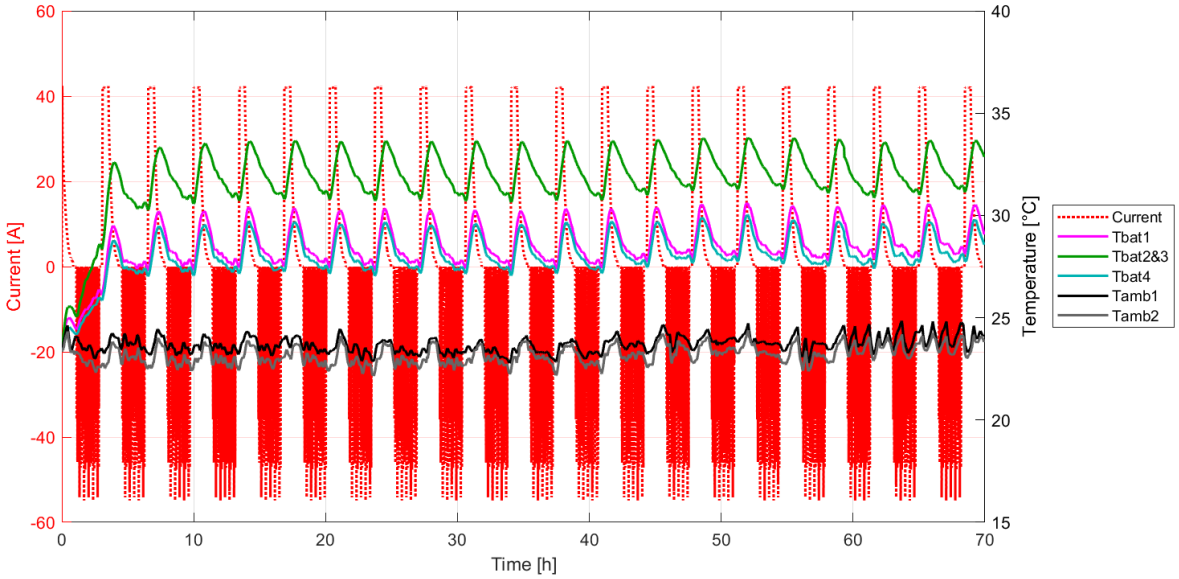

Figure 40: Current and Temperature Profiles of PCM module at 2C NRTC discharge and 1.5C CC-CV charge for 20 cycles

The corresponding thermal data shows that the module temperatures stayed within a tight band over all examined cycles. As shown in Figs 40 and 41, the maximum temperatures recorded by the three cell thermocouples were 29.50-30.70 °C at T_{bat1}, 32.60-33.80 °C at $T_{bat2\&3}$ and 28.80-29.90 °C at T_{bat4}, while the mean ambient temperature per cycle remained near 23.20-24.10 °C. This peak temperature rises above ambient of approximately 6.20-7.00 °C at T_{bat1}, 9.30-10.40 °C at $T_{bat2\&3}$ and 5.50-6.30 °C at T_{bat4}, with no systematic increase from cycle 1 to cycle 20. The temperature gradients between the middle and edge sensors were consistently small: $T_{bat2\&3}$ was only about 3.10-3.30 °C hotter than T_{bat1} in the early and late cycles and at most 4 °C hotter than T_{bat4}, again without any upward trend over cycling. Average temperatures over each cycle show stable passive thermal control. The cycle average values for T_{bat1}, $T_{bat2\&3}$ and T_{bat4} stayed close to 26.80-28.90 °C, 28.00-32.90 °C and 26.40-28.90 °C, respectively, while the ambient averages from the two sensors remained around 23-24 °C throughout.

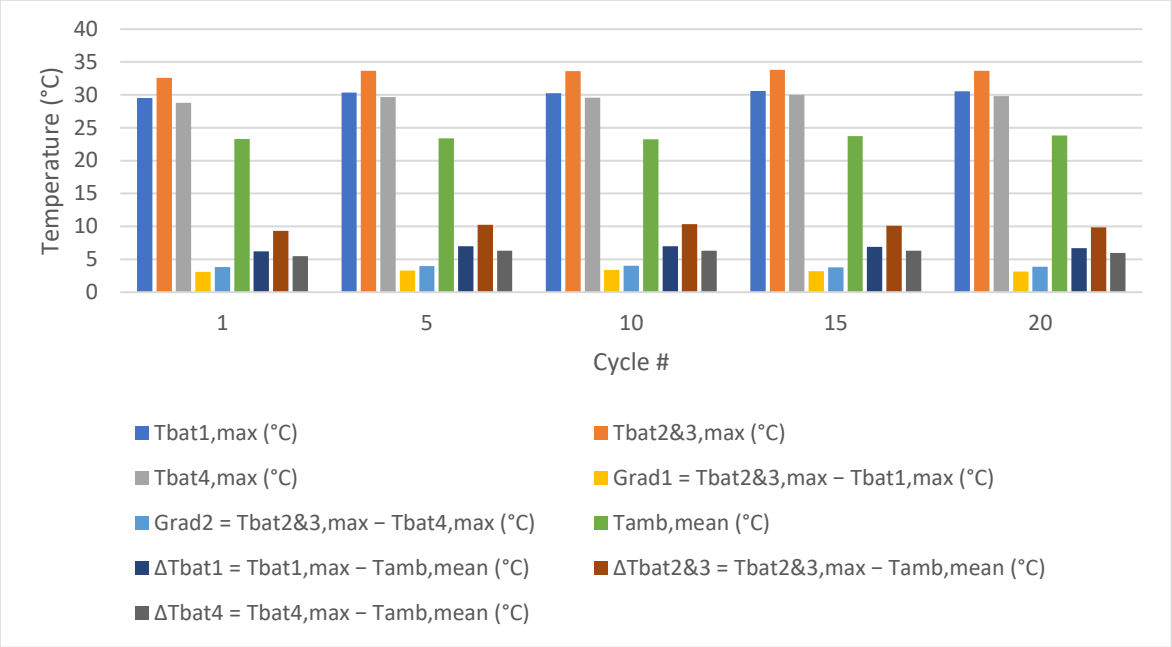

Figure 41: Peak cell temperatures, temperature rise above ambient and in-plane gradients for the selected NRTC cycles of the PCM module during CC-CV charging (cycles 1, 5, 10, 15 and 20)

Across all these cycles the middle thermocouple remains a few degrees warmer than the edge sensors because it is located between the two inner prismatic cells, where heat generated in adjacent cells accumulates before being conducted through the PCM layer and outer surfaces, whereas the edge sensors are attached to cells with one side more directly exposed to the environment.

Taken together, these results show that the PCM-equipped module limits the peak cell temperature to below roughly 34 °C and maintains middle-edge differences of only about 3-4 °C, even under repeated 2C NRTC discharge followed by 1.5C fast charging. The absence of temperature accumulation or increasing gradients across 20 consecutive cycles indicates that the PCM layer provides durable heat spreading and buffering capacity, enabling purely passive thermal management to keep the module within a narrow and repeatable temperature envelope over the full test. For context, the 1.5C constant-current / constant-voltage cycling tests performed on the non-PCM module (Section 4.2) showed maximum cell temperatures of about 37.30 °C and peak temperature rises of approximately 13.80 °C above ambient under comparable C-rates, whereas in the NRTC test with PCM the hottest cell remained below about 34 °C with a maximum rise of roughly 10.40 °C above ambient, despite the additional transient 2C discharge loading. This indirect comparison indicates that the PCM

layer not only limits temperature gradients within the module but also suppresses peak temperatures by roughly 3 °C relative to a similar module without PCM when operated at similar or less demanding C-rates.

4.4 Capacity and EIS metrics for the PCM module post-NRTC

4.4.1 Capacity test results post-NRTC

After completing 20 NRTC cycles, the discharge capacities of the four cells in the PCM module are shown in Fig 42. Compared with their initial capacities reported in Fig 28 (14.85 Ah, 14.76 Ah, 15.00 Ah and 14.96 Ah, respectively), capacity losses are 0.9% to 2.5% per cell, i.e. less than 3% over the 20 NRTC cycles. This minor capacity degradation in the PCM module might be due to the cycler errors, but the cycling should be continued for several hundreds of cycles to assess degradation more precisely.

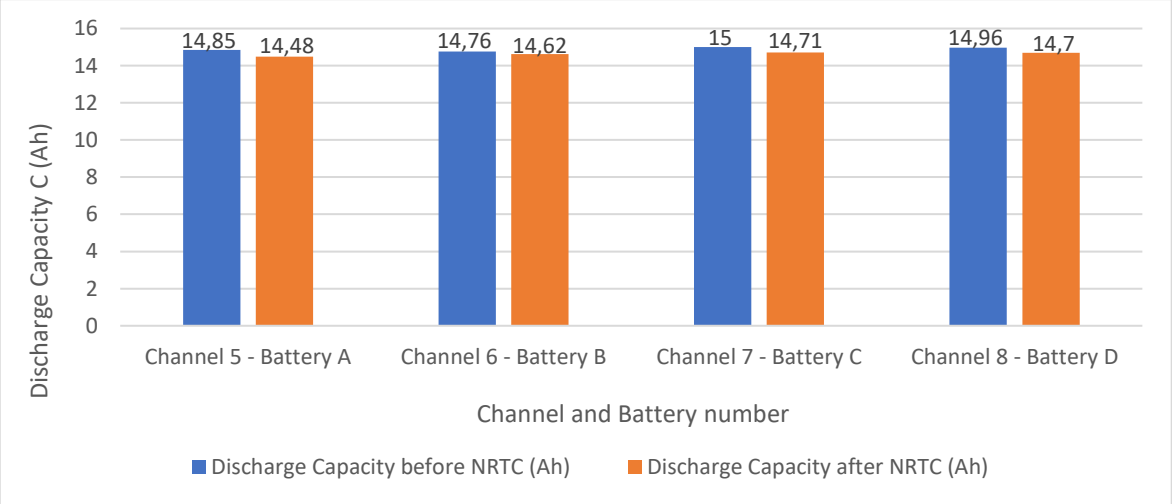

Figure 42: Discharge capacities of experimental batteries after NRTC

4.4.2 GEIS test results post-NRTC

The GEIS measurements performed after the NRTC cycling do not show a consistent, systematic shift of the Nyquist curves of the PCM module toward lower real impedance compared with the initial measurements in Figs 30 and 31. At both 100% and 50% SOC in Fig. 43 and Fig. 44, the HFR of individual cells changes only by a few milliohms, with cells

A and C exhibiting slightly higher values after NRTC, while cells B and D show slightly lower values. These small, non-uniform variations in both the high-frequency intercept and the semicircle height are within the expected experimental scatter for impedance measurements and therefore cannot be reliably interpreted as a change in ohmic or charge-transfer resistance, consequently, no clear conclusion regarding activation or degradation of the batteries can be drawn from these GEIS results alone.

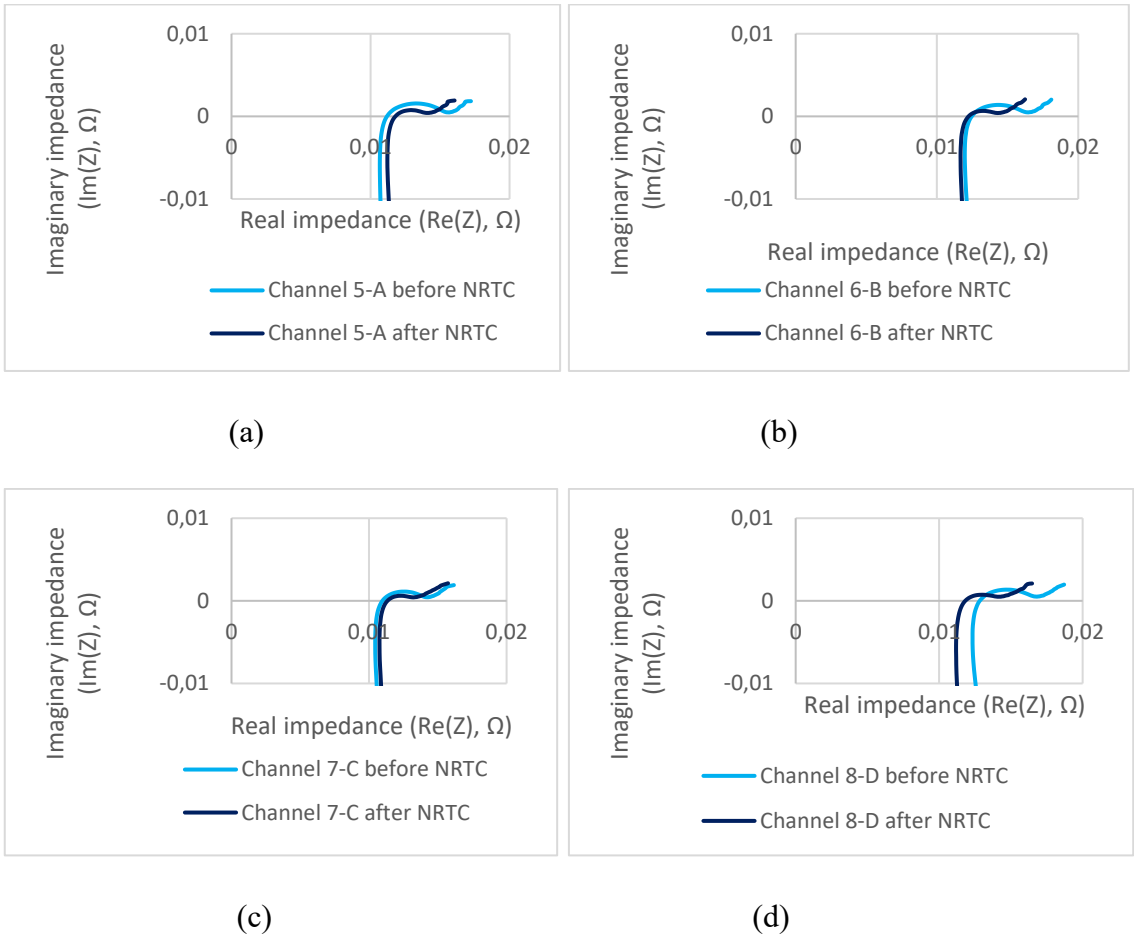

Figure 43: Nyquist plot of EIS before and after NRTC at 100% SOC (a) Channel 5 - battery A (b) Channel 6 - battery B (c) Channel 7- battery C (d) Channel 8 - battery D

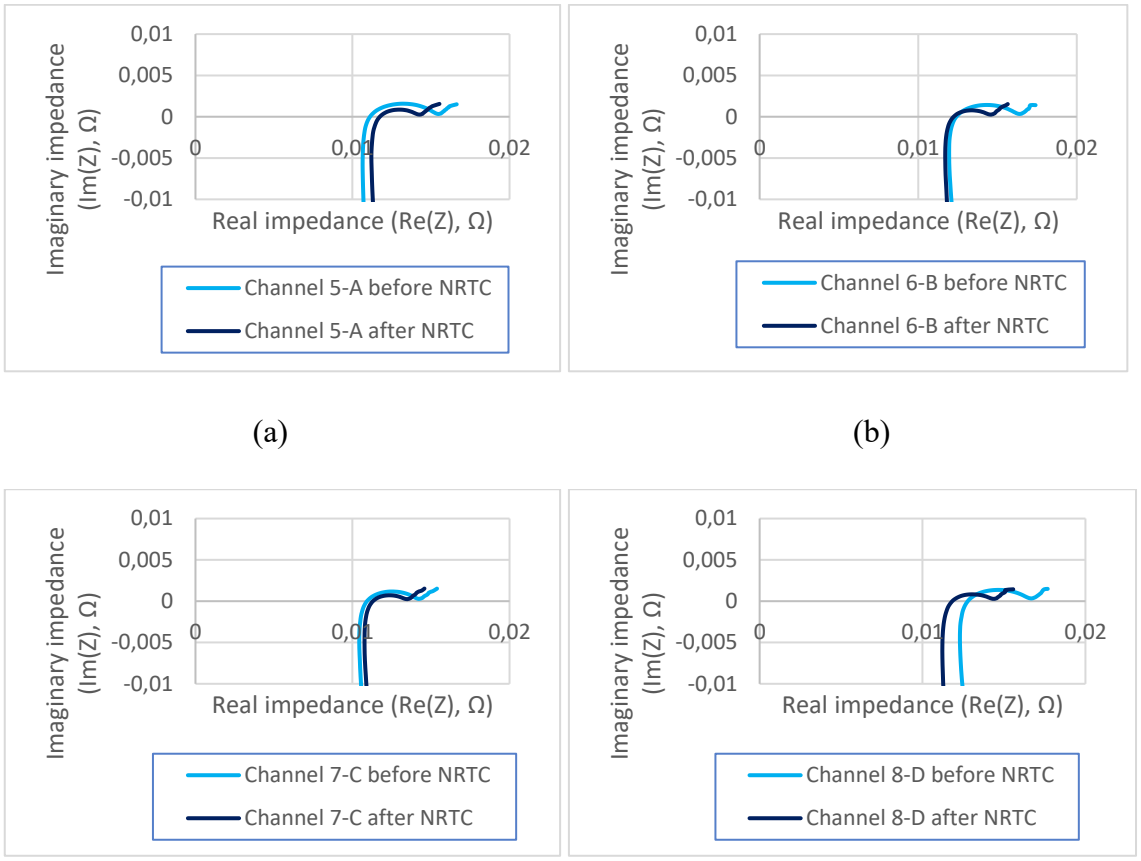

Figure 44: Nyquist plot of EIS before and after NRTC at 50% SOC (a) Channel 5 - battery A (b) Channel 6 - battery B (c) Channel 7- battery C (d) Channel 8 - battery D

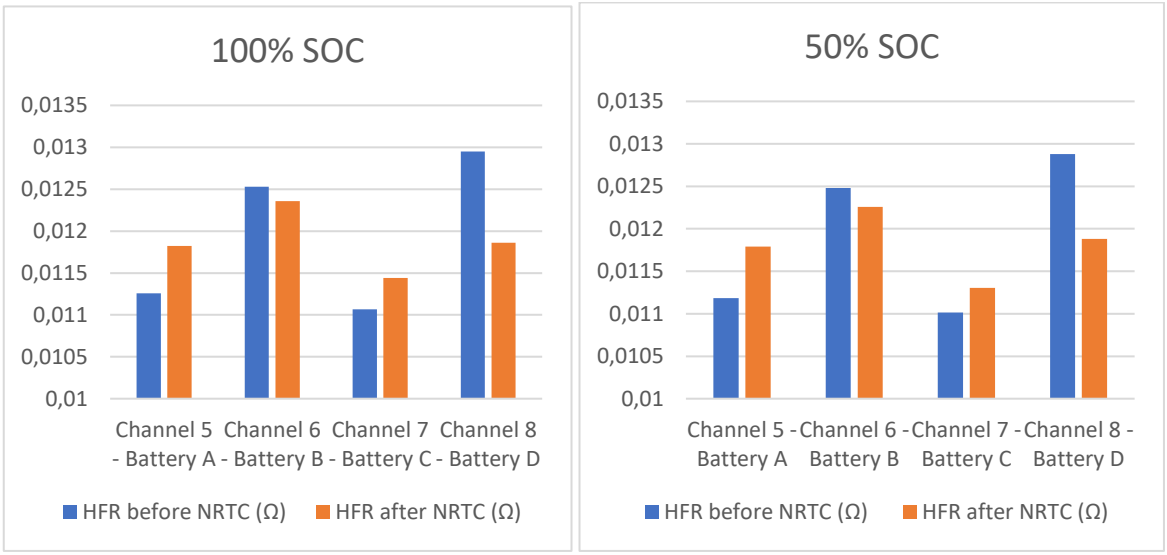

Figure 45: High-Frequency resistance (HFR) (a) at 100% SOC (b) at 50% SOC

The bar charts in Fig. 45 summarize the HFR values obtained for all four cells at 100% and 50% SOC. For batteries A and C, the interpolated HFR increases slightly after NRTC, whereas for batteries B and D it decreases by a similarly small amount, so that all changes remain within a few percent of the initial values. This bidirectional variation, together with the nearly unchanged Nyquist shapes (no extra semicircles or extended low-frequency tails) and the preserved capacity reported in the previous subsections, suggests that the observed differences reflect normal measurement scatter rather than systematic activation or degradation of the PCM-equipped module's internal impedance under the applied NRTC profile.

5 Discussion

The results show that the benefit of PCM-based passive thermal management depends strongly on the imposed C-rate and duty cycle. Under 1C CC-CV cycling, both PCM and non-PCM 2S2P modules operated in a similar temperature range, with peak cell temperatures around 33-34 °C and sensor-to-sensor gradients roughly below 3.5 °C. In this C-rate, heat generation is modest and conventional conduction through cell casings and busbars, together with natural convection to the surroundings, is sufficient to keep temperatures and gradients within acceptable limits. Consequently, the PCM layer does not significantly lower the absolute peak temperature at 1C, although it already contributes to keeping gradients small.

At 1.5C CC-CV charging, the situation changes: the non-PCM module reaches peak temperatures of about 37 °C with intra-module differences close to 5 °C, while the PCM module remains below 35 °C with gradients around 3 °C. This indicates that, once heat generation is high enough, the PCM's latent heat and enhanced lateral conduction become important in suppressing local hot spots. The NRTC tests reinforce this conclusion under a more realistic non-road duty cycle. Despite the combination of 2C discharge and 1.5C charge, the PCM module maintains peak temperatures below roughly 34 °C and stable middle–edge differences of only 3-4 °C across 20 consecutive NRTC cycles, with no trend of temperature accumulation or increasing gradients. The peak temperatures were recorded during1,5C charging and the module was cooling during the 2C NRTC discharge with an average discharge rate of 27.27 Ah which is below 1.5C.

As the battery temperature remain below the PCM melting point, it still contributes through its sensible heat capacity. From Table 9, 0.45 kg of PCM adds about 5.04 Wh of sensible thermal storage for a 20 K temperature rise, which increases the module's total sensible capacity by roughly 85 % compared with the cells alone and helps to damp short-term temperature oscillations. There is need for more aggressive NRTC cycling to demonstrate the effect of PCM more clearly.

The spatial distribution of temperatures can be understood from the module geometry. In the PCM module, the middle thermocouple is placed between two inner prismatic cells, so it naturally records the highest values as heat from adjacent cells accumulates before being

redistributed through the PCM and outer surfaces. In the non-PCM module, higher temperatures at sensors close to busbars and screw connections, and on more shielded faces, reflect local ohmic/contact heating and weaker convection. PCM reduces the sensitivity of cell temperatures to these local boundary conditions, which is particularly valuable in practical pack designs where perfectly symmetric cooling is rarely achievable. The comparison between the NRTC test with PCM and the 1.5C CC-CV test without PCM suggests that PCM lowers peak temperatures by roughly 3 °C and reduces the maximum rise above ambient by about 2.50-3.00 °C under comparable or more demanding C-rates, even though a fully symmetric NRTC test for the non-PCM module could not be carried out due to cycler limitations.

6 Conclusion

This work has explained that the PCM battery module can provide effective passive thermal management for non-road mobile machine applications. At moderate 1C cycling, the PCM and non-PCM modules show similar peak temperatures and small temperature gradients, indicating that PCM offers limited added value when heat generation is low and conventional heat rejection paths are sufficient. However, at higher 1.5C charging and under a transient NRTC duty cycle, the PCM module clearly limits hot-spot formation and reduces temperature non-uniformity compared with the non-PCM reference, while keeping absolute cell temperatures within a narrow and stable range. Further testing at higher C-rates would be needed to evaluate the PCM's performance under stressful operating conditions of NRMMs.

The NRTC experiments, although performed only on the PCM module, show that peak cell temperatures remain below 34 °C and the middle-edge differences are consistently limited to 3-4 °C over 20 consecutive cycles. There is no proof of thermal accumulation or growth of gradients is observed, suggesting that the PCM layer provides durable heat-spreading and buffering capacity during repeated high-rate operation. These observations support the suitability of PCM-based passive thermal management as a low-complexity solution for non-road battery systems that frequently experience short, high-power events followed by recharge periods.

A key limitation of the study is the incomplete symmetry of the PCM and non-PCM test matrix. Hardware constraints in the cycler prevented NRTC testing of the non-PCM module and restricted the number of NRTC loops, so the comparison between PCM-assisted NRTC operation and non-PCM CC-CV operation is indirect. In addition, only one PCM formulation, geometry and ambient condition were investigated, and the experiments focused on short-term thermal behaviour rather than long-term ageing.

Future work should extend the NRTC investigations to longer time scales and both module types. Performing NRTC cycling over 30 days or more for both PCM and non-PCM modules would allow the joint study of degradation patterns and thermal behaviour under identical transient loading. Such initiative could measure how the observed reduction in peak temperature and temperature gradients translates into slower capacity fade and impedance

growth. Further studies could also explore alternative PCM materials and configurations, hybrid passive-active cooling concepts, and high-fidelity electro-thermal modelling to support the design of full-scale battery packs for non-road mobile machines.

References

Alehosseini, E., & Jafari, S. M. (2020). *Nanoencapsulation of phase change materials (PCMs) and their applications in various fields for energy storage and management. Advances in Colloid and Interface Science, 283, 102226*. https://doi.org/10.1016/j.cis.2020.102226

Antila, M., Galimova, T., Breyer, C., Norouzi, S., Repo, S., Pihlatie, M., Pettinen, R., & Shah, S. (2025). *Future Energy Technology for Nonroad Mobile Machines. Advanced Energy and Sustainability Research, 6(3), Article 2400257.* https://doi.org/10.1002/aesr.202400257

Bao, Z., Wu, Z., Chen, H., Ma, Y., Ji, Z., Sun, F., & Luo, D. (2025). *Advanced battery thermal management systems: Technologies, integration challenges, and future trends. Journal of Energy Storage, 140(Part B), 119094.* https://doi.org/10.1016/j.est.2025.119094

Batteries Europe. (2022). *Roadmap on mobile applications of batteries (Prepared by Working Group 5). Batteries Europe*.https://batterieseurope.eu/wp-content/uploads/2022/09/Roadmap-on-mobile-applications-of-batteries_WG5.pdf

BCG research, (n. d). *Batteries for electric cars - challenges, opportunities, and the outlook to 2020. Retrieved July 6, 2021, from* https://gerpisa.org/en/system/files/file36615.pdf

Birkl, C. R., Roberts, M. R., McTurk, E., Bruce, P. G., & Howey, D. A. (2017). *Degradation diagnostics for lithium-ion cells. Journal of Power Sources, 341, 373–386*. https://doi.org/10.1016/j.jpowsour.2016.12.011

Boparai, K. S., & Singh, R. (2020). *Electrochemical energy storage using batteries, superconductors and hybrid technologies. In S. Hashmi & I. A. Choudhury (Eds.), Encyclopedia of Renewable and Sustainable Materials (pp. 248–254). Elsevier.* https://www.sciencedirect.com/topics/materials-science/lithium-ion-battery

Cai, S., Zhang, X., & Ji, J. (2023). *Recent advances in phase change materials-based battery thermal management systems for electric vehicles. Journal of Energy Storage, 72(Part E), 108750*. https://doi.org/10.1016/j.est.2023.108750

Caterpillar Inc. (n.d.). *Track loaders — 114480*. Caterpillar. https://www.cat.com/en_US/products/new/equipment/track-loaders/track-loaders/114480.html

Celltech Solutions. (2023, September 25). *Electrifying Non-Road Mobile Machinery. Retrieved from* https://celltechsolutions.fi/press/electrifying-non-road-mobile-machinery/ Celltech Solutions

Chen, J., Kang, S., E, J., Huang, Z., Wei, K., Zhang, B., Zhu, H., Deng, Y., Zhang, F., & Liao, G. (2019). *Effects of different phase change material thermal management strategies on the cooling performance of the power lithium-ion batteries: A review. Journal of Power Sources, 442, 227228.* https://doi.org/10.1016/j.jpowsour.2019.227228

Chen, W., Liang, J., Yang, Z., Li, G., et al. (2019). *A Review of Lithium-Ion Battery for Electric Vehicle Applications and Beyond. Energy Procedia, 158, 4363–4368*. https://doi.org/10.1016/j.egypro.2019.01.783

Di Luca, G., Muccillo, M., Giardiello, G., Gimelli, A., & Di Blasio, G. (2020). *Numerical assessment of different engine model levels in the view of complex hybrid application.* Journal of Environmental Science and Engineering Technology, 8, 52–62. https://doi.org/10.12974/2311-8741.2020.08.6

DieselNet. (n.d*.). Emission Test Cycles: NRTC. Retrieved from* https://dieselnet.com/standards/cycles/nrtc.php

DieselNet. (n.d.). *ISO 8178-4: Reciprocating internal combustion engines — test cycles. Retrieved from* https://dieselnet.com/standards/cycles/iso8178.php

DieselNet. (n.d.). *Nonroad Transient Cycle (NRTC). Retrieved from* https://dieselnet.com/standards/cycles/nrtc.php

Donaldson. (2024). *How electrification transforms mining efficiency: BEVs, batteries & trolley systems. E-Mobility Engineering. Retrieved from* https://www.emobility-engineering.com/electrification-mining-bevs-batteries-trolley-systems/

Environmental Protection Agency. (2005*). Engine-testing procedures: 40 CFR Part 1065 (Source: 70 FR 40516, July 13, 2005). Code of Federal Regulations*. U.S. Government. https://www.ecfr.gov/current/title-40/part-1065

Esmaeili, J.; Jannesari, H. *Developing Heat Source Term Including Heat Generation at Rest Condition for Lithium-Ion Battery Pack by Up Scaling Information from Cell Scale. Energy Convers. Manag. 2017, 139, 194–205*. https://doi.org/10.1016/j.enconman.2017.02.052

F. Mocera, A. Somà and D. Clerici., *"Study of aging mechanisms in lithium-ion batteries for working vehicle applications," 2020 Fifteenth International Conference on Ecological Vehicles and Renewable Energies (EVER), Monte-Carlo, Monaco, 2020, pp. 1-8,* doi: 10.1109/EVER48776.2020.9243079.

Flash Battery. (2022, June 30). *Lithium batteries type: which chemistry should be used? Retrieved from* https://www.flashbattery.tech/en/blog/types-of-lithium-batteries-which-chemistry-use/

Guan, J., & Chen, M. (2024). *An overview of phase change materials on battery application: Modification methods and thermal management systems. Journal of Energy Storage, 103 (Part A), 114268*. https://doi.org/10.1016/j.est.2024.114268

Guchen. (n.d.). *Battery thermal management system (BTMS). Retrieved from* https://www.guchen.com/products/battery-thermal-management-system/

Gungor, S., & Lorente, S. (2024). *PCM-based passive cooling solution for Li-ion battery pack: A theoretical and numerical study. Applied Thermal Engineering, 257(Part A), 124262*. https://doi.org/10.1016/j.applthermaleng.2024.124262

Guo, J.; Guo, Q.; Liu, J.; Wang, H. *The Polarization and Heat Generation Characteristics of Lithium-Ion Battery with Electric–Thermal Coupled Modelling. Batteries 2023, 9 (11), 529*. https://doi.org/10.3390/batteries9110529

Huber, C. (2017). *Phase Change Material in Battery Thermal Management Applications: An assessment of efficiency and safety (Doctoral dissertation, Technische Universität München). Retrieved from* https://mediatum.ub.tum.de/1356376

Jaswani, P. (2024). *Battery markets in construction, agriculture & mining machines 2024-2034. IDTechEx. Retrieved from* https://www.idtechex.com/en/research-report/march-s-des-batteries-dans-les-machines-de-construction-dagriculture-et-dexploitation-mini-re-2024-2034/1008

John Deere. (n.d.). *GX Crew electric utility vehicle*. John Deere. https://www.deere.com/en/gator-utility-vehicles/electric-gators/gx-crew-electric-utility-vehicle/

John Deere. (n.d.). *X-series combines*. John Deere. https://www.deere.com/en/harvesting/x-series-combines/

Kharabati, S., & Saedodin, S. (2024). *A systematic review of thermal management techniques for electric vehicle batteries. Journal of Energy Storage, 75, 109586*. https://doi.org/10.1016/j.est.2023.109586

Lagerstedt, F., Kärnell, S., Rösth, M., & Ericson, L. (2025). *Analysis of Opportunities for Integrated Thermal Management on Battery Powered Mobile Machines. In L. Ericson & P. Krus (Eds.), Advancements in Fluid Power Technology: Sustainability, Electrification, and Digitalization. Lecture Notes in Mechanical Engineering. Springer*. https://doi.org/10.1007/978-3-031-84505-5_21

Lajunen, A., Sainio, P., Laurila, L., Pippuri-Mäkeläinen, J., & Tammi, K. (2018). *Overview of powertrain electrification and future scenarios for non-road mobile machinery. Energies, 11(5), 1184*. https://doi.org/10.3390/en11051184

Li, W., Zhou, Y., Zhang, H., & Tang, X. (2023). *A Review on Battery Thermal Management for New Energy Vehicles. Energies, 16(13), 4845.* https://doi.org/10.3390/en16134845

Lindgren, M. (2005). A *Transient Fuel Consumption Model for Non-road Mobile Machinery. Biosystems Engineering, 91(2), 139–147.* https://doi.org/10.1016/j.biosystemseng.2005.03.011

Lumikko. (2025, March 24). *Thermal management in off-highway EVs – better efficiency and lifespan. Retrieved from* https://lumikko.fi/en/thermal-management-in-off-highway-evs-better-efficiency-and-lifespan/

Lumikko. (n.d.). *Electrification of Mobile Work Machines. Retrieved from* https://lumikko.fi/en/industries/electrification/mobile-work-machines/

Ma, S.; Jiang, M.; Tao, P.; Song, C.; Wu, J.; Wang, J.; Deng, T.; Shang, W. *Temperature Effect and Thermal Impact in Lithium-Ion Batteries: A Review. Prog. Nat. Sci. Mater. Int. 2018, 28(6), 653–666.* https://doi.org/10.1016/j.pnsc.2018.11.002

Ma, S.; Jiang, M.; Tao, P.; Song, C.; Wu, J.; Wang, J.; Deng, T.; Shang, W. *Temperature Effect and Thermal Impact in Lithium-Ion Batteries: A Review. Prog. Nat. Sci. Mater. Int. 2018, 28(6), 653–666*. https://doi.org/10.1016/j.pnsc.2018.11.002

Madani, S. S., Hajihosseini, M., & Ziebert, C. (2024). *A brief survey on heat generation in lithium-ion battery technology. Renewable Energy and Environmental Sustainability, 9, 9*. https://doi.org/10.1051/rees/2024006

Maher, K.; Boumaiza, A.; Amin, R. *Understanding the Heat Generation Mechanisms and the Interplay between Joule Heat and Entropy Effects as a Function of State of Charge in Lithium-Ion Batteries. J. Power Sources 2024, 623, 235504.* https://doi.org/10.1016/j.jpowsour.2024.235504

Mahlia, T. M. I., Saktisahdan, T. J., Jannifar, A., Hasan, M. H., & Matseelar, H. S. C. (2014). *A review of available methods and development on energy storage; technology update. Renewable and Sustainable Energy Reviews, 33, 532 545.* https://doi.org/10.1016/j.rser.2014.01.068

Mem Magazine (2025, June 27). *Optimising thermal management for electrified off-road, construction, and mining equipment: The push for electrification in heavy-duty machines. EV & Fuel Cells, Mining. Retrieved from* https://memuknews.com/infrastructure/mining/thermal-management/

Mesha. (2025, September 25). *How temperature affects lithium-ion battery performance? Tips to prevent damage. Tycorun Energy*. https://www.tycorunenergy.com/how-temperature-affects-lithium-ion-battery-performance/

Mika, Ł., Radomska, E., Sztekler, K., Gołdasz, A., & Zima, W. (2025). *Review of Selected PCMs and Their Applications in the Industry and Energy Sector. Energies, 18(5), 1233*. https://doi.org/10.3390/en18051233

Murashko, K. A., Pyrhönen, J., & Jokiniemi, J. (2020). *Determination of the through-plane thermal conductivity and specific heat capacity of a Li-ion cylindrical cell*. International Journal of Heat and Mass Transfer*, 162*, Article 120330. https://doi.org/10.1016/j.ijheatmasstransfer.2020.120330

Nasiri, M., & Hadim, H. (2025). *Thermal management of Li-ion batteries using phase change materials: Recent advances and future challenges. Journal of Energy Storage, 111, 115440*. https://doi.org/10.1016/j.est.2025.115440

NetZero-Events. (n.d.). *Challenges and opportunities in charging infrastructure for non-road mobile machinery. Retrieved from* https://netzero-events.com/challenges-and-opportunities-in-charging-infrastructure-for-non-road-mobile-machinery/

Optimising Thermal Management for Electrified Off-Road, Construction, and Mining Equipment. (2025, June 27). EV & Fuel Cells, Mining. Retrieved from https://memuknews.com/infrastructure/mining/thermal-management

Patil, S. R., Lokavarapu, B. R., & Thaliyanveedu, H. K. (2023). *Optimization of battery cooling system used in electric vehicles. Journal of Energy Storage, 58, 106299.* https://doi.org/10.1016/j.est.2022.106299

Pilali, E., Soltani, M., Hatefi, M., Shafiei, S., Salimi, M., & Amidpour, M. (2025). *Passive thermal management systems with phase change material-based methods for lithium-ion batteries: A state-of-the-art review. Journal of Power Sources, 632,* 236345. https://doi.org/10.1016/j.jpowsour.2025.236345

Podara, C. V., Kartsonakis, I. A., & Charitidis, C. A. (2021). *Towards Phase Change Materials for Thermal Energy Storage: Classification, Improvements and Applications in the Building Sector. Applied Sciences, 11(4), 1490.* https://doi.org/10.3390/app11041490

Rahmani, A., Dibaj, M., & Akrami, M. (2024). *Recent advancements in battery thermal management systems for enhanced performance of Li-ion batteries: A comprehensive review. Batteries, 10(8), 265.* https://doi.org/10.3390/batteries10080265

Rao, Z., Wang, S., & Zhang, G. (2011). *Simulation and experiment of thermal energy management with phase change material for ageing $LiFePO_4$ power battery*. Energy Conversion and Management, 52, 3408–3414. https://doi.org/10.1016/j.enconman.2011.07.009

Rasool, G., Xinhua, W., Sun, T., Hayat, T., Sheremet, M., Uddin, A., Shahzad, H., Abbas, K., Razzaq, I., & Yuexin, W. (2024). *Recent advancements in battery thermal management system (BTMS): A review of performance enhancement techniques with an emphasis on nano-enhanced phase change materials. Heliyon, 10(17), e36950*. https://doi.org/10.1016/j.heliyon.2024.e36950

Sandvik Mining and Rock Technology. (n.d.). *TH550B*. Sandvik. https://www.mining.sandvik/en/products/equipment/trucks/th550b/

Shen, W.; Wang, N.; Zhang, J.; Wang, F.; Zhang, G. *Heat Generation and Degradation Mechanism of Lithium-Ion Batteries during High-Temperature Aging. ACS Omega 2022, 7(47), 43256–43264.* https://doi.org/10.1021/acsomega.2c04093

Sundar, A., Vannarath, A., Prucka, R., & Zhu, Q. (2023). *The Influence of Cooling Air-Path Restrictions on Fuel Consumption of a Series Hybrid Electric Off-Road Tracked Vehicle. SAE Technical Paper 2023-01-1611.* https://doi.org/10.4271/2023-01-1611

Thomas, K. E.; Newman, J. *Heats of Mixing and of Entropy in Porous Insertion Electrodes. J. Power Sources 2003, 119–121, 844–849*.

Thomas, K. E.; Newman, J. *Thermal Modeling of Porous Insertion Electrodes. J. Electrochem. Soc. 2003, 150, A176–A192*.

Transport & Environment. (2024, December). *Reducing emissions from non-road mobile machinery (BRIEFING – December 2024). Retrieved from* https://www.transportenvironment.org/uploads/files/202412_NRMM_briefing_final.pdf

Transport Policy. (n.d.*). EU: Nonroad: Emissions. Retrieved from* https://www.transportpolicy.net/standard/eu-nonroad-emissions/

Transport Policy. (n.d.). *International: Nonroad: NRTC Test. Retrieved from* https://www.transportpolicy.net/standard/international-nonroad-nrtc-test/

UNECE. (2011). ECE-TRANS-WP29-GRPE: *Technical regulation for nonroad mobile machinery – NRTC test cycle (Document No. WP29-GRPE-2011-11e). United Nations Economic Commission for Europe. Retrieved from* https://unece.org/fileadmin/DAM/trans/doc/2011/wp29grpe/ECE-TRANS-WP29-GRPE-2011-11e.pdf

Weng, J., Yang, X., Zhang, G., Ouyang, D., Chen, M., & Wang, J. (2019). *Optimization of the detailed factors in a phase-change-material module for battery thermal management*. International Journal of Heat and Mass Transfer, 138, 126–134. https://doi.org/10.1016/j.ijheatmasstransfer.2019.04.050

YANMAR Technical Review. (2023, December 8). *Motor Thermal Analysis for Electrification of Machinery. Retrieved from* https://www.yanmar.com/

Zhang, X., Kong, X., Li, G., & Li, J. (2014). *Thermodynamic assessment of active cooling/heating methods for lithium-ion batteries of electric vehicles in extreme conditions. Energy, 64, 1092–1101*. https://doi.org/10.1016/j.energy.2013.10.088

Zhi, M., Fan, R., Yang, X., Zheng, L., Yue, S., Liu, Q., & He, Y. (2022). *Recent research progress on phase change materials for thermal management of lithium-ion batteries. Journal of Energy Storage, 45, 103694.* https://doi.org/10.1016/j.est.2021.103694

Zhu, Z., Zhang, Y., Chen, A., Chen, J., Wu, Y., Wang, X., & Fei, T. (2025). *Review of integrated thermal management system research for battery electric vehicles. Journal of Energy Storage, 106, 114662*. https://doi.org/10.1016/j.est.2024.114662

Appendix 1. Datasheet of the LIB from Phylion

DESCRIPTION ATTACHMENTS

Lithium cells for long-lasting performance

Powerful lithium cells that deliver long-lasting performance for your projects. These lightweight and compact batteries offer excellent energy density and fast charging with long life. With our lithium cells, you'll be able to power your equipment with ease, and with confidence in their long-term reliability. Take on projects with the confidence that power will always be on hand!

Technical specifications:

- Rated capacity: 14 Ah (1C / +25 °C)
- Rated voltage: 3.65 V
- Energy: 51 Wh
- Operating voltage range: 2.75 V – 4.2 V
- Maximum charging voltage: 4.20 V
- Standard charging current: 14 A / 1C
- Maximum continuous discharge current: 42 A / 3C
- Maximum discharge current: 70 A / 5C (5 seconds)
- Self-discharge rate: ≤ 3% / month
- Internal resistance: ≤ 3 mΩ
- Number of cycles / lifetime: > 1000
- Operating temperature / charging: 0 °C ~ 45 °C
- Operating temperature / discharging: -20 °C ~ 50 °C
- Storage temperature: -30 °C ~ 45 °C

PHYLION

Brand PHYLION

Features

Chemical composition	Li-Ion
Rated capacity (Ah)	14
Energy (kWh)	51 Wh
Rated voltage (V)	3,65
Clamp and tightening torque	No bolts
Dimensions (W × H × D)	66 × 133 × 18 mm
Case made of	aluminium
Model	Prismatic
Package weight	0.32 kg

Appendix 2. Datasheet of Rubitherm RT35HC

Data sheet

RUBITHERM Phase Change Material

RT35HC

RUBITHERM® RT is a pure PCM, this heat storage material utilising the processes of phase change between solid and liquid (melting and congealing) to store and release large quantities of thermal energy at nearly constant temperature.
The RUBITHERM® phase change materials (PCM's) provide a very effective means for storing heat and cold, even when limited volumes and low differences in operating temperature are applicable.

Properties for RT-line:
- high thermal energy storage capacity
- heat storage and release take place at relatively constant temperatures
- no supercooling effect, chemically inert
- long life product, with stable performance through the phase change cycles
- melting temperature range between -9 °C and 100 °C available

The most important data:	Typical Values	
Melting area	34-36 main peak: 35	[°C]
Congealing area	36-34 main peak: 35	[°C]
Heat storage capacity ± 7,5% Combination of latent and sensible heat in a temperatur range of 27°C to 42°C.	240	[kJ/kg]*
	67	[Wh/kg]*
Specific heat capacity	2	[kJ/kg·K]
Density solid at 20°C	0,83	[kg/l]
Density liquid at 40°C	0,77	[kg/l]
Heat conductivity (both phases)	0,2	[W/(m·K)]
Volume expansion	12	[%]
Flash point	177	[°C]
Max. operation temperature	70	[°C]

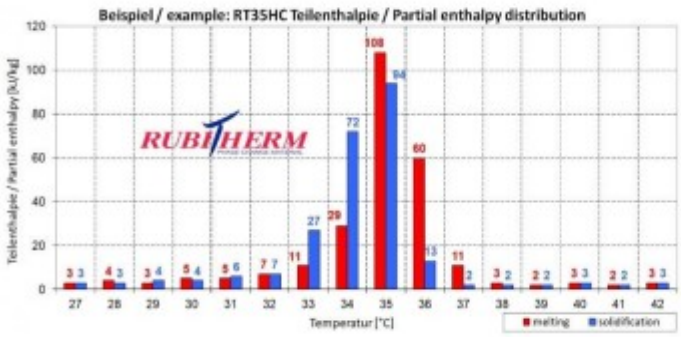

Rubitherm Technologies GmbH
Imhoffweg 6
D-12307 Berlin
phone: +49 (30) 7109622-0
E-Mail: info@rubitherm.com
Web: www.rubitherm.com

The product information given is a non-binding planning aid, subject to technical changes without notice.
Version: 08.02.2024

*Measured with 3-layer-calorimeter.

Appendix 3. Calculations of thermal sizing

From the below diagram of the honeycomb spacer, the dimensions of the spacer are given as133mm x 66mm x 20mm.

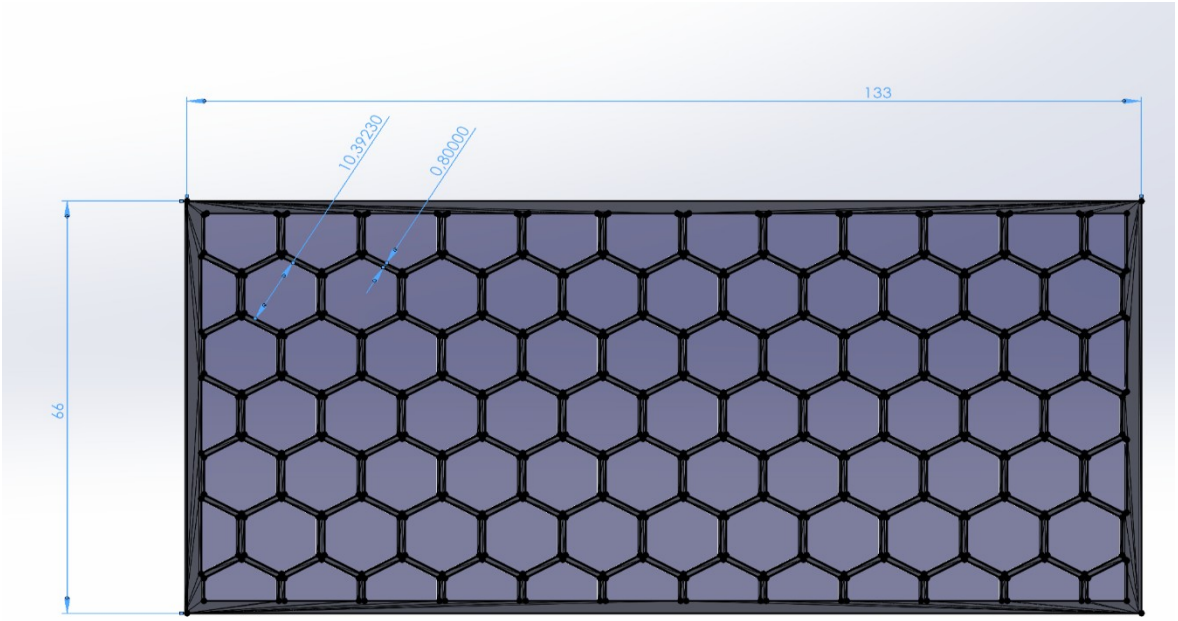

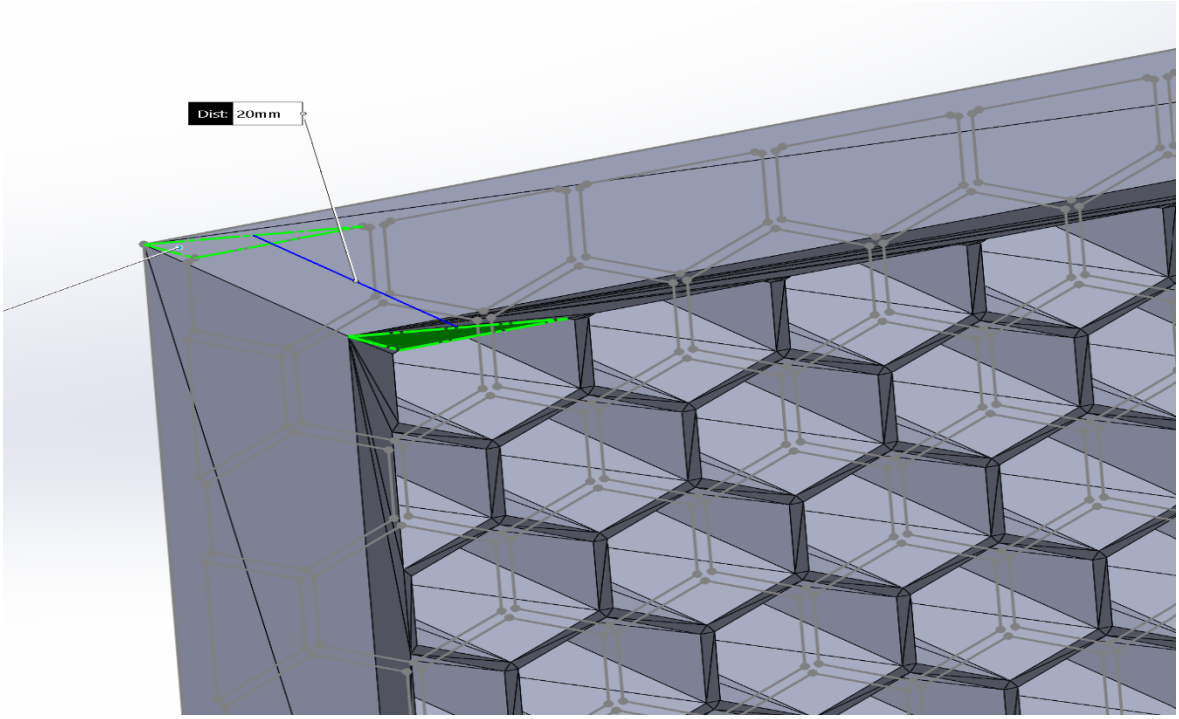

As the PCM is filled inside these hexagonal shapes and we have used five such spacers. To determine the mass of the PCM, the total volume of the all the spacer cavities is calculated first. From the diagram, we have Flat-to-flat length of hexagon as, f =10.39mm which is given by the equation: $f = 2s$

where, s is side length and is derived from the above equation as, $s = f/2$

$$s = 10.39/2$$

$$s = 5.195 \text{ mm}$$

Area of one hexagon is given by $A_{hex} = 3\frac{\sqrt{(3)}}{2}s^2$

$$A_{hex} = 3\frac{\sqrt{(3)}}{2}(5.195)^2$$

$$A_{hex} = 70.2 \text{ mm}^2$$

From above diagram, depth of each cell, d = 20 mm

Therefore, Volume per hexagon cell, $V_{cell(hex)}$ is given by: $V_{cell(hex)} = A_{hex} \times d$

$$= 70.2 \times 20$$

$$V_{cell(hex)} = 1404 \text{ mm}^3$$

Number of hexagon structures per each spacer is approximately 84, therefore:

$$V_{spacer} = 84 \times 1404 = 1.18 \times 10^5 \text{ mm}^3$$

We have used 5 spacers in the PCM module, $V_t = V_{spacer} \times 5$

$$= 5 \times 1.18 \times 10^5 \text{ mm}^3$$

$$V_t = 5.9 \times 10^5 \text{ mm}^3$$

Converting it into litres, we have 1 $\text{mm}^3 = 10^{-6}$ L, therefore, $V_t = 0.59$ L

From Eq. (5) $m_{PCM} = V_t \times \rho_{PCM}$

$\rho_{PCM} = 0.77$ kg/L (Appendix 2) and $V_t = 5.9 \times 10^5 \text{ mm}^3$

Therefore, $m_{PCM} = 0.59 \times 0.77$

$m_{PCM} = 0.45$ kg i.e., PCM module was filled with 0.45 kg of PCM.

From Eq. (6), we have $P_i = nR_{int}I^2$

Substituting n = 4, R_{int} = 3m Ω = 3 × 10^{-3} Ω (Appendix 1) and I = 28 A

we have: $P_i = 4 \times 3 \times 10^{-3}\ \Omega \times (28)^2$

P_i = 9.408 W

From Eq. (8), we have $Q_i = P_i \times \Delta t$

Substituting P_i = 9.408 W and Δt ~ 1618 s:

$$Qi = 9.408 \times 1618$$

$$Q_i = 15222.144 \text{ J}$$

$$Q_i = 4.22 \text{ Wh (since, 1Wh = 3600 J)}$$

From Eq. (9), we have $Q_{sens,bat} = nm_{bat}c_{bat}\Delta T$

Substituting m_{bat} = 320 g = 0.32 kg (Appendix 1), ΔT = 20K (Assumption), c_{bat} = 0.83 × 10^3 $Jkg^{-1}K^{-1}$ [Murashko et al., 2020], we have:

$$Q_{sens,bat} = 4 \times 0.32 \text{ x } 0.83 \times 10^3 \times 20$$

$$Q_{sens,bat} = 2.12 \times 10^4 \text{ J}$$

$$Q_{sens,bat} = 5.9 \text{ Wh (since 1Wh = 3600 J)}$$

From Eq. (11) and (12), we have $Q_{t,PCM} = m_{PCM}(c_{PCM}\Delta T + f_m \Delta H_{PCM})$

Substituting c_{PCM} = 2 kJ $kg^{-1}K^{-1}$= 2000 J $kg^{-1}K^{-1}$ (Appendix 2)

ΔH_{PCM} = 240 kJ kg^{-1} = 240 × 10^3 J kg^{-1} (Appendix 2)

f_m = 1 (fully melted PCM)

$$Q_{t,PCM} = 0.45\ ((2000 \times 20) + 1\ (240 \times 10^3))$$

$$Q_{t,PCM} = (18172 \text{ J}) + (108 \times 10^3 \text{ J})$$

$Q_{sens,PCM}$ = 18172 J = 5.04 Wh

$Q_{lat,PCM}$ = 108 × 10^3 J = 30 Wh

$Q_{t,PCM}$ = 35.04 Wh (1Wh = 3600 J)